UNIVERSITY OF CALIFORNIA
RIVERSIDE

Synthesis and Characterization of Oxide/Metal Exchange-Coupled Nano-Composite Materials for Permanent Magnetic Applications

A Dissertation submitted in partial satisfaction
of the requirements for the degree of

Doctor of Philosophy

in

Mechanical Engineering

by

Aleksey Volodchenkov

June 2016

Dissertation Committee:
Dr. Javier Garay, Chairperson
Dr. Yasuhiro Kodera
Dr. Jing Shi
Dr. Lorenzo Mangolini

The Dissertation of Aleksey Volodchenkov is approved:

_____

_____

_____

_____

Committee Chairperson

University of California, Riverside

Acknowledgements

I dedicate this dissertation and the completion of my doctorate degree to my wife Grissel, my parents Dmitriy and Marina, and my brother Daniel. Without their support, this endeavor would not have been possible.

Journal of Materials Chemistry C has published my work: Synthesis of strontium ferrite/iron oxide exchange coupled nano-powders with improved energy product for rare earth free permanent magnet applications. The manuscript was written with co-authorship of Yasuhiro Kodera and Javier Garay and accepted May 09, 2016. Data and parts of discussion rewritten from the mentioned published work was used in Section 3.1 of the dissertation.

ABSTRACT OF THE DISSERTATION

Synthesis and Characterization of Oxide/Metal Exchange-Coupled Nano-Composite Materials for Permanent Magnetic Applications

by

Aleksey Volodchenkov

Doctor of Philosophy, Graduate Program in Mechanical Engineering
University of California, Riverside, June 2016
Dr. Javier Garay, Chairperson

Permanent magnets (PMs) are essential to an amazing variety of current and future devices, causing widespread interest in improving PM performance. A promising approach to improving PM performance is exchange-coupling between hard and soft magnetic phases. Exchange-coupling has been shown to improve the energy product of nano-composite magnets, compared to their single phase counterparts. This dissertation presents a simple and scalable material engineering route that produces exchange-coupling in nano-composite PMs. Notably, no rare-earth (RE) or precious metals are used. The composites are ferrite based. In one system, $SrFe_{12}O_{19}$ is used as the hard phase and Fe_3O_4 as the soft phase. In the second system $SrFe_{12}O_{19}$ is the hard phase while Co is the soft phase, leading to oxide/metal nano-composites. In order to maximize the beneficial effect of exchange-coupling, a fine degree of mixing between the hard and soft phases is required. In order to achieve well intermixed phases at the nano-scale, soft phase precursor is precipitated on

$SrFe_{12}O_{19}$ flakes through heterogeneous precipitation by decomposition of urea. The soft phase precursor is reduced and core-shell hard/soft magnetic composite is synthesized. A clear processing window is established to control composition. This requires temperatures high enough to reduce the soft phase precursor, yet low enough to keep the hard/soft interphase reaction free, producing a hard/soft ratio that maximizes the energy product. The resulting nano-composite powder outperforms the energy product of pure hard phase, $SrFe_{12}O_{19}$ by 37%.

The energy product of hard/soft magnetic nano-composite powder is further improved by applying a similar synthesis route to a $SrFe_{12}O_{19}$/Co composite (Co replacing Fe_3O_4 as the soft phase). In order to optimize microstructure and composition ratio, the amount of Co precipitated on $SrFe_{12}O_{19}$ is varied by controlling precipitation time and precipitation $SrFe_{12}O_{19}$:Co ratio. Synthesizing optimized $SrFe_{12}O_{19}$/Co composite powder leads to an energy product improvement of 162% compared to pure $SrFe_{12}O_{19}$ powder.

Bulk dense nano-composite materials have been difficult to synthesize due to grain growth attributed from slow heating rates of traditional sintering techniques. High processing temperatures leads to high density, minimizing property diluting porosity. However, a thermodynamically favored reaction at elevated temperatures deprives the composite of improved magnetic properties. Core-shell $SrFe_{12}O_{19}$/Co nano-composite powders are processed into bulk samples through Current Activated Pressure Assisted Densification (CAPAD). Relatively high processing pressure and heating rates are taken advantage of during CAPAD and a processing window that leads to high density, as well as reaction free samples is established. The result is oxide/metal nano-composites, which

would not have been possible though traditional sintering. The processing route developed produces bulk $SrFe_{12}O_{19}$/Co composite material with a 70% improvement in energy product compared to the bulk $SrFe_{12}O_{19}$. First order reversal curve (FORC), δM and recoil loop analysis is used to provide evidence of exchange-coupling.

Table of Contents

List of Figures

1 Introduction

1.1 Motivation

Permanent magnets (PMs) find themselves at the heart of a host of modern technologies. Anything from speakers, medical devices, motors and generators to Hall Effect sensors use magnets. The PM industry is expected to grow to $15 billion by 2018 [1]. The use of PMs has allowed for higher efficiencies in renewable energy applications such as wind turbines. The strongest magnets are based on rare-earth (RE) materials such as Neodymium. Since their discovery in 1984 by General Motors [2] and Sumitomo Special Metals Company [3], Neodymium Iron Boron (neo) magnets have been at the helm of most high performance magnetic applications thanks to their high energy product (40 MGOe), a figure of merit for the performance of PMs.

However, there have been a number of problems with RE based magnets. REs are environmentally damaging and costly to mine and process [4]. They also have poor corrosion resistance. RE based magnets cost significantly more, per weight, than ferrite based magnets. In addition, the supply of Neodymium has been very volatile in the past, mostly due to monopolized RE mining [1]. In addition, as the world demand grew from 40,000 tons in 2000 to 120,000 tons in 2010, the supply of RE was reduced [5]. Lack of stability in supply has caused the price of Nd_2O_3 to spike from $17/kg to $85/kg in 2010 [6]. Even with growing supply in the recent past [7], the supply volatility of REs is still considered a risk in the future, as identified by the US Department of Energy [8]. Green technologies such as wind turbines use as much as 1.5 tons of magnetic material per

turbine[6], triggering United States and other governments engaged in energy efficient technology to have colossal interest in finding a replacement for RE based magnets[9].

1.2 The Promise of Exchange-Coupled Permanent Magnets

With progress in the ability to control microstructure at the nano level, magnetic properties have been improved. Two magnetic phases interacting with each other at the phase boundary have been shown to have a higher energy product that either of the two constituents [10]. This interaction is called magnetic exchange-coupling. Its effect is maximized when the area of interaction between the phases is large, requiring for intermixing between the phases at the nano-scale [11]. Very fine control of microstructure is required for improved magnetic properties in exchange-coupled magnets.

Research and development of exchange-coupled magnets has been based conducted since with early Since early 1990s [10]. Despite the promise of improved magnetic properties, exchange-coupling in bulk nano-composite PMs has been an elusive task, and thus many works have not been able to improve the energy products of the composite over the constituent phases [12]. Since microstructure is more difficult to control in bulk materials, the research as focused primarily on 1D [13] (powders) and 2D [14] (thin film) materials. Previous work on the development of exchange-coupling bulk materials was mostly centered on either RE based magnets or magnets containing precious metals [15], inapplicable to large scale commercial applications.

2 Background

2.1 Magnetism

2.1.1 Briefs History of Permanent Magnets

The earliest use of magnetism has been in navigation. Chinese chronicles form thousands of years ago as well as European reports from 1200AD [16] wrote of the use of lodestone, containing Fe_3O_4 as compass [17]. PM materials have come a long way since the time of the early compass. The energy product, a figure of merit for the performance of PMs has increased significantly about every decade though the 20th century as shown in **Figure 2.1.1.1** [18]. The improvements in the performance of PMs have mostly been due to the development and discovery of new materials.

Developed in Japan, Cobalt steel magnets dominated the beginning of the 20th century [17]. Alnico magnets consisting of Al, Ni, Co and Fe were developed in 1931 [16], and are still used in the highest temperature applications. 1950s brought along the discovery of Barium and Strontium Ferrites. These ceramic magnets, developed by Philips laboratories have higher than before reported coercivities, at the expense of overall magnetization[19]. The next major breakthrough came from Rare Earth (RE)-Co based magnets[20]. These included materials such as $SmCo_5$, with the highest yet magneto-crystalline anisotropy[17]. Arguably the most popular RE-based magnet $Nd_2Fe_{14}B$ was discovered in 1984 by General Motors[2] and Sumitomo Special Metals Company [3], dominating PM applications since.

Unfortunately, the improvements in performance of PMs has stagnated over the last 30 years. Researchers believe that the next step in improving the energy product will come not from the discovery of new phases, but from nanostructural engineering. Magnets made from several known magnetic phases, synthesized with optimized microstructure, are the key to the next step forward in improving the energy product of PMs.

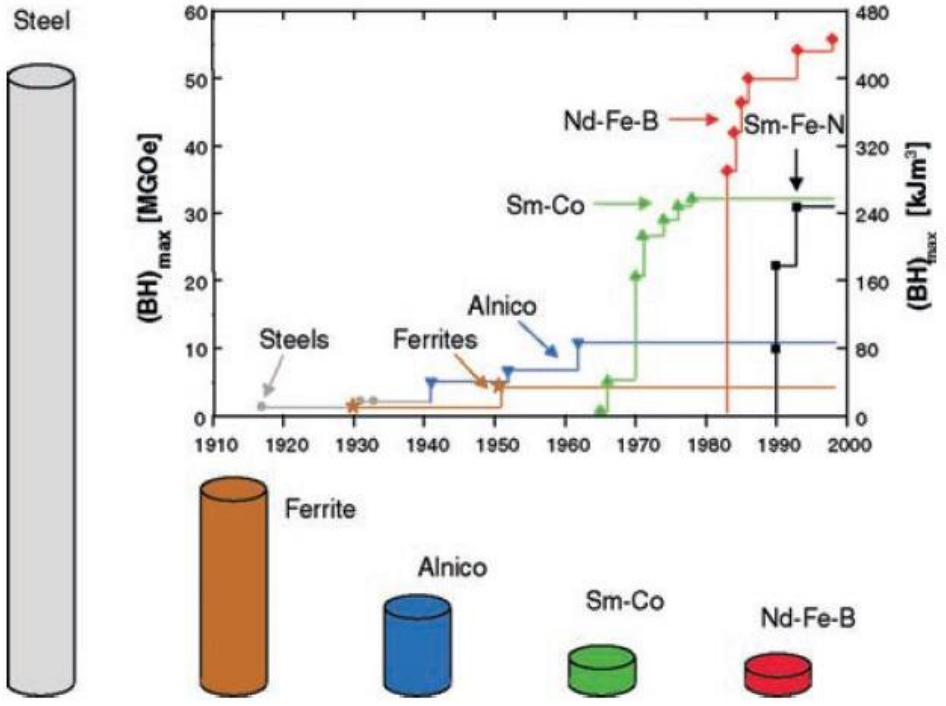

Figure 2.1.1-1 Improvement in energy product of various permanent magnet materials through the 20th century. From REF [18].

2.1.2 Classes of Magnetic Materials

The phenomena of magnetism has its roots at the electron level. The angular momentum due to an electron's orbital and/or spin give rise to the atomic magnetic moment. The Bohr magneton, μ_b, is a unit for the magnetic moment of one electron. The

effective magnetic moment, μ_{eff}, takes into consideration the number of unpaired electrons and their angular momentums[21] and how they interact with each other. Although traditionally measured experimentally[22], and approximate μ_{eff}, for a specific material could be calculated.

There are several classes of magnetic materials. These classes are diamagnetism, paramagnetism, ferromagnetism, antiferromagnetic and ferrimagnetism. The magnetization, *m* [emu], of different classes of materials responds differently to externally applied magnetic field, *H* [Oe]. Magnetic susceptibility *X* [emu/Oe], is the initial response of a material to *H*, and is described in **Equation 2.1.2-1**.

$$M = XH \qquad \textit{(Equation 2.1.2-1)}$$

Diamagnetic materials generally have a weak response to an externally applied field and are sometimes even referred to as not magnetic. The susceptibility of a diamagnetic material is negative. The net magnetic moment, μ_{eff}, for of a diamagnetic material is zero since it has no unpaired electrons. As seen in **Figure 2.1.2-1 (a)**, the diamagnetic material has a negative response to an external field and generally impedes *H* across it. The susceptibility of a diamagnetic material is not effected by temperature.

Paramagnetic materials have unfilled *d* of *f* electron shells and a non-zero μ_{eff}. Without the influence of *H*, the magnetic moments of atoms of a paramagnetic material point in random directions, usually due to thermal randomizing effects. These materials have a positive susceptibility, hence a positive response to an external field, as seen in

Figure 2.1.2-1 (b). The susceptibility of a paramagnet becomes lower with increasing temperature.

Ferromagnetic materials are the most familiar to the general public. This class of material is used often for PMs. Ferromagnetic material has long term periodic order with moments aligning parallel to each other, as seen in **Figure 2.1.2-2 (a)**. The large positive response of a ferromagnetic material to an external field is seen in **Figure 2.1.2-1 (c)**. Ferromagnetic material's susceptibility decreases with increasing temperature. There exists a temperature called the Currie Temperature, T_c, at which the material loosed long range ferromagnetic order and begins to act as a paramagnet.

Antiferromagnetic materials, like ferromagnetic materials exhibit long range ordering. However instead of parallel moment alignment, in the ferromagnetic case, antiferromagnetic material's moments align anti-parallel, as soon in **Figure 2.1.2-2 (b)**. Generally, the moments of an antiferromagnet cancel and this class of materials does not make a good candidate for PMs. The susceptibility of an antiferromagnet increases with temperature until Niel Temperature, T_n, after which the material acts paramagnetic.

The last class of magnetic material is ferrimagnetic. Ferrimagnetic materials exhibit long range order with moments aligning anti-prallel, similar to antiferromagnetic ordering. However, the magnitude of the moment is stronger in one direction, than in the other, leading to a net magnetization. Ferrimagnetic materials behave similarly to ferromagnetic materials with a decrease in susceptibility with increasing temperature. Above *Tc*, ferrimagnetic materials behave like paramagnets.

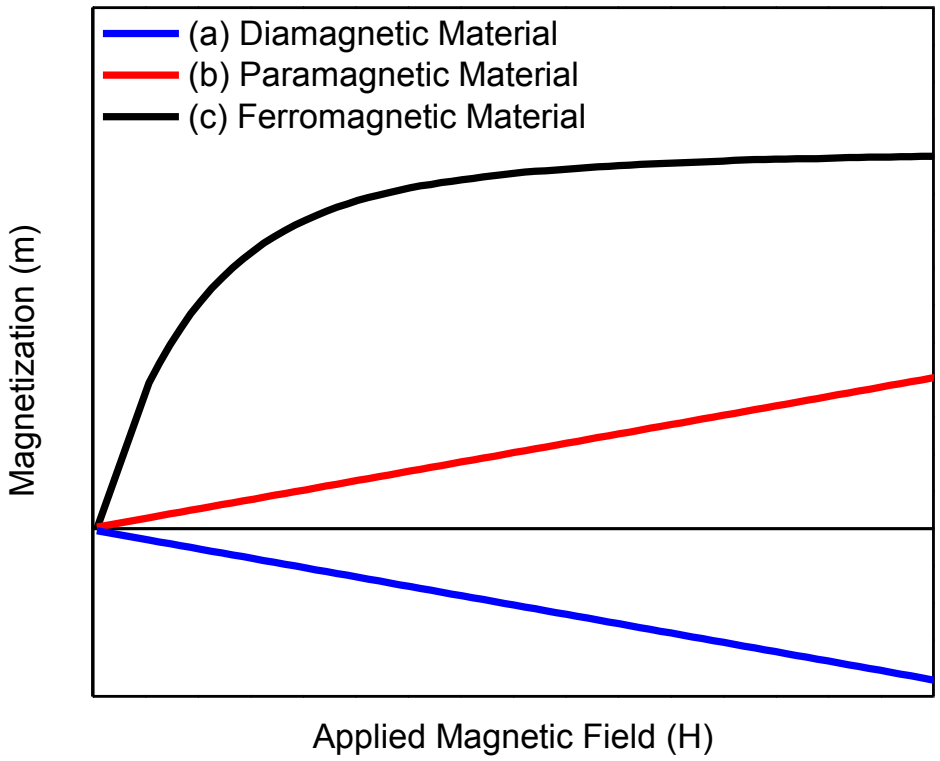

Figure 2.1.2-1 Schematic response of (a) diamagnetic, (b) paramagnetic and (c) ferromagnetic materials to an externally applied magnetic field

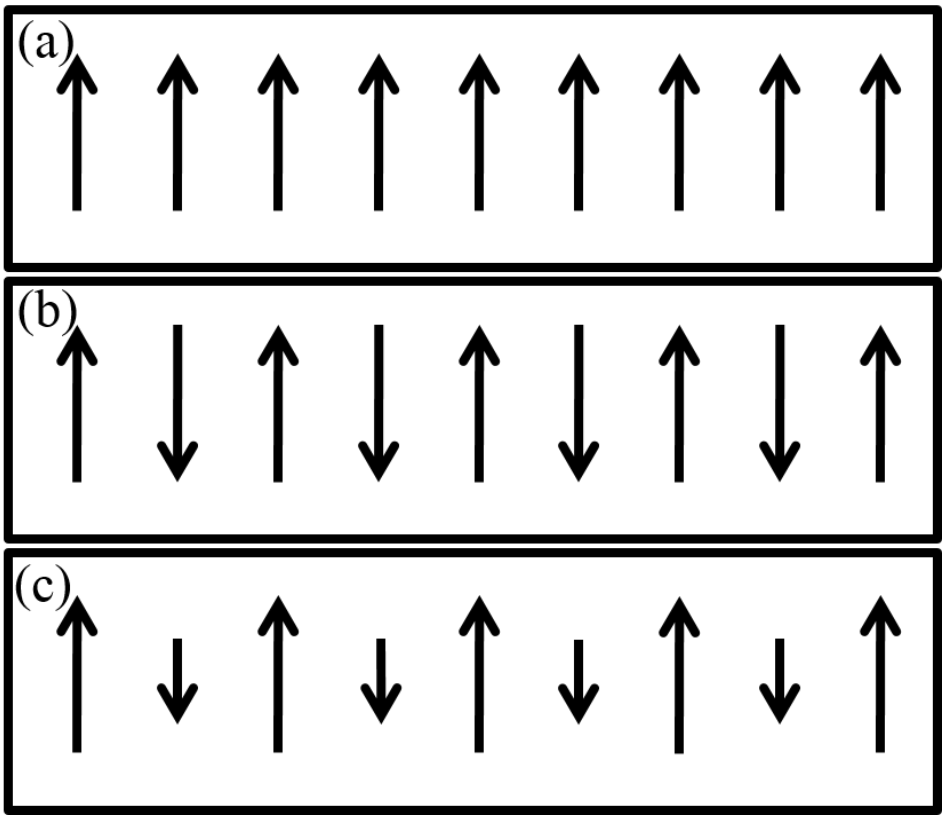

Figure 2.1.2-2 Periodic order in (a) ferromagent, (b) antiferromagnet and (c) ferrimagnet

2.1.3 Energies and Domains in Magnetic Materials

There are several energies in balance when magnetic moments interact with *H*, and amongst each other. A magnetic moment, μ, in *H* has the potential energy, *U(θ)*, equal to the dot product between μ and *H* as shown in **Equation 2.1.3-1**.

$$U(\theta) = -\mu \cdot H \qquad \text{(Equation 2.1.3-1)}$$

It is clear that *U(θ)* is minimized when the magnetic moments in the material align parallel to *H*. Another energy involved in dictating the magnetic state of material is the energy assosicate with magneto-crystalline anisotropy of the material[23]. There are certain

crystallographic directions in which magnetic moments prefer to point to minimize this anisotropy energy, called the easy directions of magnetization. The directions which maximize a material's anisotropy energy, are called the hard directions of magnetization.

Another energy associated with the magnetic state is exchange energy[23]. Exchange energy is minimized when the alignment of moments is in a similar direction, such as in the ferromagnetic long range order. Lastly, the magneto-static energy is very large when all the moments of a material point the same direction. This is due to the energetically high state associated with the material creating a large magnetic field around itself. The minimization of the total magnetic energy, given by **Equation 2.1.3-1** dictates the overall magnetic state of the material.

$$E = E_{Zeeman} + E_{exchange} + E_{anisotroy} + E_{magnetostatic} \qquad \textit{(Equation 2.1.3-2)}$$

Magnetic domains are regions in a material in which the magnetic moments all point in the same direction. They exist due to a fine balance of energies within a magnetic material. While exchange energy would dictate for all the moments to point in a single easy direction (to minimize anisotropy energy) magneto-static energy would be very large. In order to minimize the expanse of the magnetic field created from multiple moments pointing in the same direction, the material subdivides into numerous domains to lower the magneto-static energy. Randomly oriented domains are shown in a hypothetical material in **Figure 2.1.3-1**.

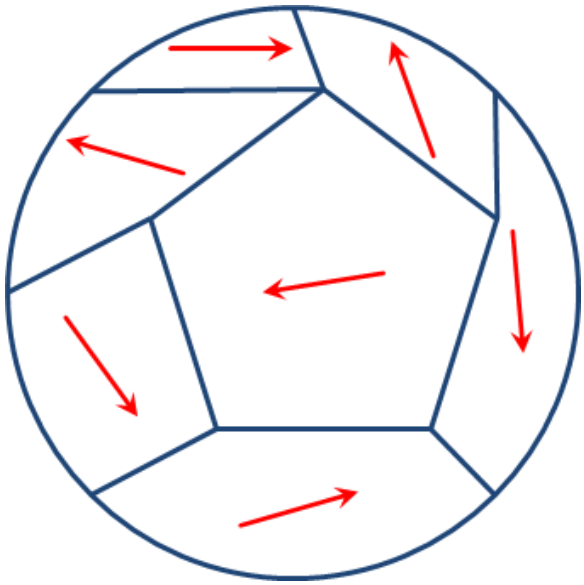

Figure 2.1.3-1 Material subdividing into domains to minimize magneto-static energy

The region between two domains is called a domain wall. Within the domain wall, moments rotate from the direction of alignment of one domain to the direction of alignment of the neighboring domain as seen in **Figure 2.1.3-2**. The length of the domain wall, δ, is dictated by the competition for minimization of anisotropy and exchange energy. Anisotropy energy is minimized when moments don't point in hard directions. In a long domain wall, under gradual moment rotation, many moments will point in unfavorable directions. Minimization of anisotropy energy calls for a narrow domain wall. If the wall is narrow, ratio of the rotation of the moments to distance from the domain will be large, causing the moments to rotate abruptly. This will cause a high angle between adjacent moments, maximizing exchange energy. δ is a ratio between a materials anisotropy energy constant, K, and exchange energy constant, A. For a Bloch style domain wall, **Equation 2.1.3-3** dictates δ.

$$\delta = \pi\sqrt{\frac{A}{K}} \qquad \textit{(Equation 2.1.3-3)}$$

Figure 2.1.3-2 Magnetic moment structure within a domain wall

2.1.4 Important Properties of Permanent Magnetic Materials

There are several properties important for PM materials. Most magnetic properties discussed in this dissertation come from a magnetic hysteresis loop measurement, shown in **Figure 2.1.4-1**. The materials magnetization, m [emu], is measured as a function of H. m is generally normalized by mass and reported as σ [emu/g] for powders, and by volume reported as M [emu/cm^3]for bulk samples.

The hysteresis loop measurement generally starts with a demagnetized PM. As the H increases, m will grow up to a certain point. When m no longer increases with increasing H the material has reached saturation. At this condition, all magnetic moments point in the direction of the applied field (minimizing Zeeman energy). Satiation values are commonly reported as σ_s [emu/g] or M_s [emu/cm^3].

Once the material is saturated, H is decreased back to 0. The magnetization at this point is called the material's remanence and is reported as σ_r [emu/g] or M_r [emu/cm^3]. Importantly for PM applications, the microstructure of PMs is could be textured. Texturing enables the material to have improved magnetic properties, and a more square hysteresis

loop. Textured PMs have a M_r/M_s ratio higher than 0.5 (maximum for non-textured materials).

Once at M_r, H increases in the opposite direction to the original saturation direction, decreasing m. At a large enough negative H, m=0 and the sample is completely demagnetized. The magnitude of H that fully demagnetize a saturated sample is the sample's coercivity, H_c. H_c depends on material property K. However, it could also be tuned by microstructure. Grain size has a large effect on H_c. A sample with a very small grain size, containing few atoms has poor H_c due to thermal randomizing effects. A small grain cannot hold a domain since magnetic moments associated with individual atoms point in random directions (anisotropy energy doesn't play enough of a role). Samples made of large grains have poor H_c as well. Several domains, separated by a domain wall, could occupy a large grain. Demagnetization within such a grain occurs by domain wall motion. Atomic magnetic moments flip one plane at a time as the domain wall sweeps across the grain. The largest coercivity is founds in samples with grain size matching that of single domain size. At a relatively small grain size it is energetically unfavorable for a domain wall to exist, only one domain exists per grain. Since there is no domain wall to propagate as the grain is magnetized in a different direction, all the moments have to rotate at once. This simultaneous rotation of moments requires higher H, yielding a higher H_c for the sample, than when demagnetization is done by domain wall motion. Besides grain size, there are other microstructural features that affect Hc. Generally, lattice defects such as secondary phases and grain boundaries block domain walls from propagating. Different grains have different crystallographic orientations, hence different easy and hard

directions. It is generally not energetically favorable for a domain wall propagating through one grain to propagate through the adjacent grain in the same direction under constant *H*. *H* needs to increase sufficiently to overcome the energy hump associated with domain wall jumping a grain boundary to propagate through the adjacent grain.

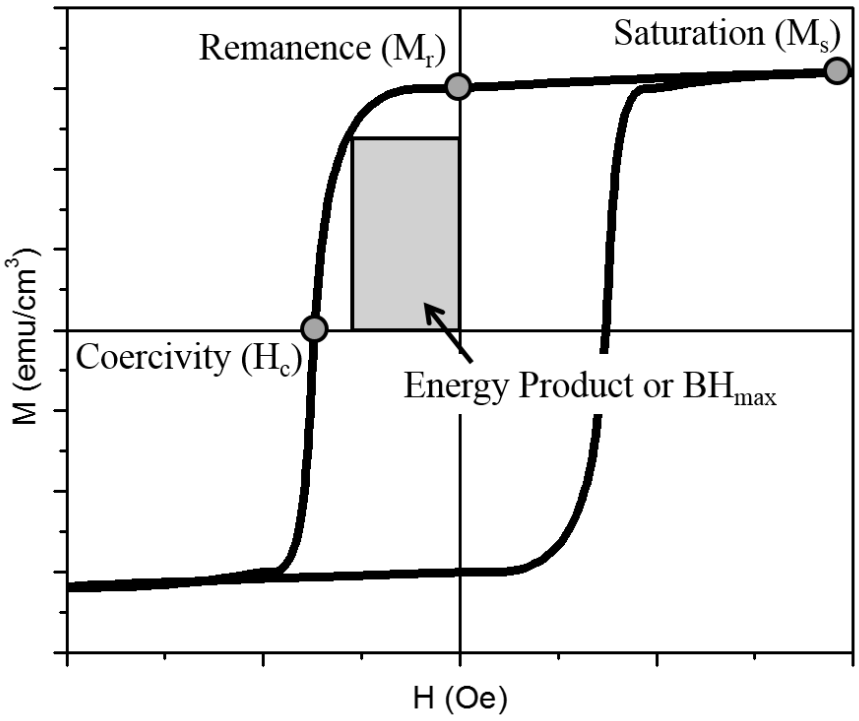

Figure 2.1.4-1 Hysteresis curve measurement of a permanent magnet

2.2 Exchange-Coupled Permanent Magnets

Nano-structured materials contain a significant amount of atoms at the grain boundary [24]. Such materials typically exhibit different properties than their non-nano-structured counterparts. Magnetic properties, having interaction lengths at the nano-scale [21], could be improved and tailored through nano-structuring of materials. One of such mechanisms is called exchange-coupling (also exchange-spring). Exchange-coupling improves the properties of PMs by combining the high H_c of the hard phase and the high M_s of the soft phase in a composite acting as a single phase. Under demagnetization, the hard phase keeps the moments of the soft phase aligned in the original direction of magnetization under oppositely applied H. The exchange energy between the hard and soft phases has a higher effect on the magnetic structure of the material than the Zeeman energy due to H. Exchange-coupling is maximized when the hard and soft phase interphase area is large. Since the interphase area is much higher with nano-scale microstructure, exchange-coupled PMs benefit greatly from the intermixture of hard and soft phases at the nano-scale.

2.2.1 Brief History of Exchange-Coupled Permanent Magnets

Despite the high reward, exchange-coupled PMs have been an elusive goal. In 1989, Coehorn *et. al.* observed improved M_r in multiphase Nd-Fe-B magnets and attributed the enhancement to interaction between phases [25]. Kneller and Hawig proposed the idea of an exchange-spring magnet in July of 1991 [10]. In order to reach a maximum energy

product, a material must exhibit both a high magneto-crystalline anisotropy as well as a high magnetization. Kneller and Hawig realized that most hard magnets are RE based, highly corrosive and pricy compare to most soft magnets. They proposed the idea of combining hard and soft magnetic materials as a composite magnet. Kneller and Hawig also suggested the benefit of a soft phase enveloping the hard phase, in order to in improve exchange-coupling, as well as protect the easily corroded hard phase. Kneller and Hawig showed theoretical calculations which concluded that in order to have high degree of exchange-coupling, "the microstructure of such materials are a fine and regular dispersion of phases in a scale of the order of 10 nm". They also performed a study on the nucleation of Fe rich areas within a Neo magnet. Higher than expected M_r/M_s ratio was theorized. Kneller and Hawig's exchange spring idea opened the door and started a race for a new type of PM materials.

Several other groups performed calculations in the 1990s to predict the magnetic properties of exchange-coupled composites. Skimski and Coey predicted energy products over 100MGOe in RE based nano-structured two-phase magnets [11]. Sabiryanov and Jaswal from the University of Nebraska showed that the energy product limit for a $SmCo_5$ - $Co_{1-x}Fe_x$ composite is a whooping 65MGOe. Curie temperature of such a composite would also increase and is predicted to reach as high as 1115^{o}C [26].

There have been numerous successful techniques in creating nano-composite exchange-coupled magnetic materials using top-down techniques. Mechanical milling and alloying [27]–[29], melt spinning[25],[30] and arc melting[27],[29] techniques have been at the forefront of exchange-coupled nano-composite synthesis for powders and ribbons.

There had been plenty of work done in 2D (film) materials[31]–[34]. Unfortunately, these techniques don't have a lot of potential to be used as scalable synthesis route that could one day be used for bulk commercial applications.

Bottom-up approach is a potential method for scalable exchange-coupled PM synthesis. Creating well intermixed nanoparticles of hard and soft magnetic materials is very difficult. There have been successes in creating composite nanoparticles of hard and soft magnetic materials. Hou *et al.* and Chaubey *et. al.* reported successful synthesis of magnetic composites of $SmCo_5$ / Fe with improved magnetic properties by high temperature reduction of nanoparticles [35], [36]. The composites showed in increase in M_r from 45 emu/g for single phase $SmCo_5$ to 56 emu/g for the composite; magnetic saturation also increased, at the expense of H_c. Although a lot of work has focused on RE based composite magnets, there has been work done in RE free magnets as well.

In 2002, Zeng et al. in a collaboration between IBM, Louisiana Tech University and Georgia Institute of Technology showed clear evidence of exchange-coupling [37]. The research focused on hard FePt magnetic material with soft Fe_3Pt magnetic material in a PM composite. Hexane dispersions of FePt and Fe_3O_4 nano-particles with different mass ratios as well as particle sizes were investigated. The dispersions were dried and the nano-particles assembled. Best mixing was achieved with 4nm particles of FePt and Fe_3O_4 while 12 nm particles of Fe_3O_4 and 4 nm particles of FePt created the most inhomogeneous assemblies. The samples were then annealed in 5% H_2 balance Ar gas at 650^{o}C for 1 hr. The annealing got rid of organic particles as well as converted Fe_3O_4 into αFe. Pt from FePt then diffused into the newly created Fe rich zone, creating Fe_3Pt, a soft magnetic material.

Sintered nano-particles from the starting size of 4nm created well intermixed zones of hard and soft magnetic material, while the sample what started off with 12nm Fe_3O_4 nano-particles had soft magnetic zones in excess of 20 nm. As expected, the coercivity decreased with higher mass fraction of soft phase while saturation magnetization increased. M_r however, had a maximum value with a Fe_3O_4: FePt mass ratio of 0.10. The sample with the maximum M_r was studied further and showed an energy product 50% higher than the theoretical limit of the hard FePt phase. Samples with large zones of soft phase were also studied further and show two phase behavior, having a kink in the hysteresis loop and low energy product. It was theorized that the large soft phases were not well intermixed and lacked enough surface boundaries between the soft and hard phases, inhibiting effective exchange-coupling. This group showed great prospects for the future of PMs. They demonstrated great control of microstructure, as well as great properties. However, Pt is very rare and expensive, and it is impractical to consider it as a replacement material for Neo magnets. Very recently, the engineering feat of an exchange-coupled, RE free nano-composite PM with improved magnetic properties made of abundant materials has been realized [38].

Very little work has been done in bulk 3D exchange-coupled PMs. There are difficulties in synthesizing bulk materials with microstructure in the nano-scale due to grain growth attributed to slow heating rates of traditional sintering techniques [17]. Emerging technologies such as spark plasma sintering and shock compaction have allowed for the synthesis of bulk materials with nano-scale grains. Bulk exchange-coupled magnets based on the Fe-Pt system have been synthesized with densities as high as 70% theoretical

density[39]. RE based exchange-coupled bulk PMs were produced by shock compaction[40]. Ribbons of $Nd_2Fe_{14}B$/Fe composite were rapidly quenched, pulverized and annealed. Fully dense bulk nano-composites were produced without grain growth. Despite the pioneering work described above, bulk exchange-coupled magnets with improved properties compared to constituent phases, free of RE and precious metals have not yet been developed.

2.2.2 Characterization of Exchange-Coupling in Permanent Magnets

2.2.2.1 Hysteresis Loop Kink Analysis

The hysteresis loop could provide insight to the lack of coupling between hard and soft magnetic phases. **Figure 2.2.2-1** shows a schematic hysteresis loops of soft, hard, exchange-coupled and no- exchange-coupled materials. Soft magnetic materials have high M_s but low H_c. Hard magnetic materials have low M_s but high H_c. If there is sufficient exchange between the phases of the soft and hard magnetic materials, the hysteresis loop of the exchange-coupled composite will act like a single phase, taking advantage of the high M_s of the soft phase and the high H_c of the hard phase. However, if there is poor mixing between the magnetic phases, the decoupled material will have a kink in the second and fourth quadrants of the hysteresis loop[13], [37], [41], [42].

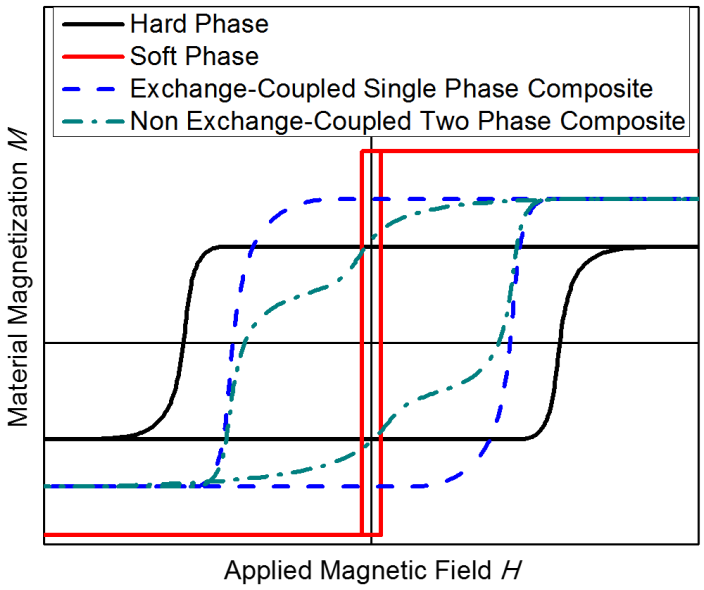

Figure 2.2.2-1 Schematic hysteresis loops of soft, hard, exchange-coupled and non exchange-coupled materials

2.2.2.2 δM Analysis

The δM analysis is a popular method of evaluating exchange-coupling in magnets [13], [36], [41], [43]. The δM analysis is based on the comparison between M_r of a demagnetized magnetic sample as a function of H in the positive direction and the M_r of a saturated sample as a function of H in the negative direction. The demagnetizing remanence curve, *DRC*, is obtained by saturating a sample and measuring M_r as a function of H values in the opposite direction. The isothermal remanence curve, *IRC*, is obtained by measuring M_r as a function of H, while $H<H_{saturation}$[44]. Function values $M_rd(H)$ and $M_ri(H)$ are obtained from *DRC* and *IRC* respectively. The relationship between *IRC* and

DRC is known from E. P. Wohlfarth and given in **Equation 2.2.2-1**, for non-interacting particles[45].

$$M_r d(H) = M_r - 2M_r i(H) \qquad \textit{(Equation 2.2.2-1)}$$

Kelly *et. al.* modified Wohlfarth' relationship to account for interacting particles and is given in **Equation 2.2.2-1**. Kelly's relationship gives insight on the nature of interaction of the particles.

$$\delta M = \frac{M_r d(H)}{M_r} - \left[1 - \frac{2M_r i(H)}{M_r}\right] \qquad \textit{(Equation 2.2.2-2)}$$

Positive δM values suggest interactions that support the magnetized state, such as exchange-coupling. Negative δM values imply interactions that support the demagnetized state, such as dipole/dipole interaction. A measured δM curve of an exchange-coupled magnet is shown in **Figure 2.2.2-2**.

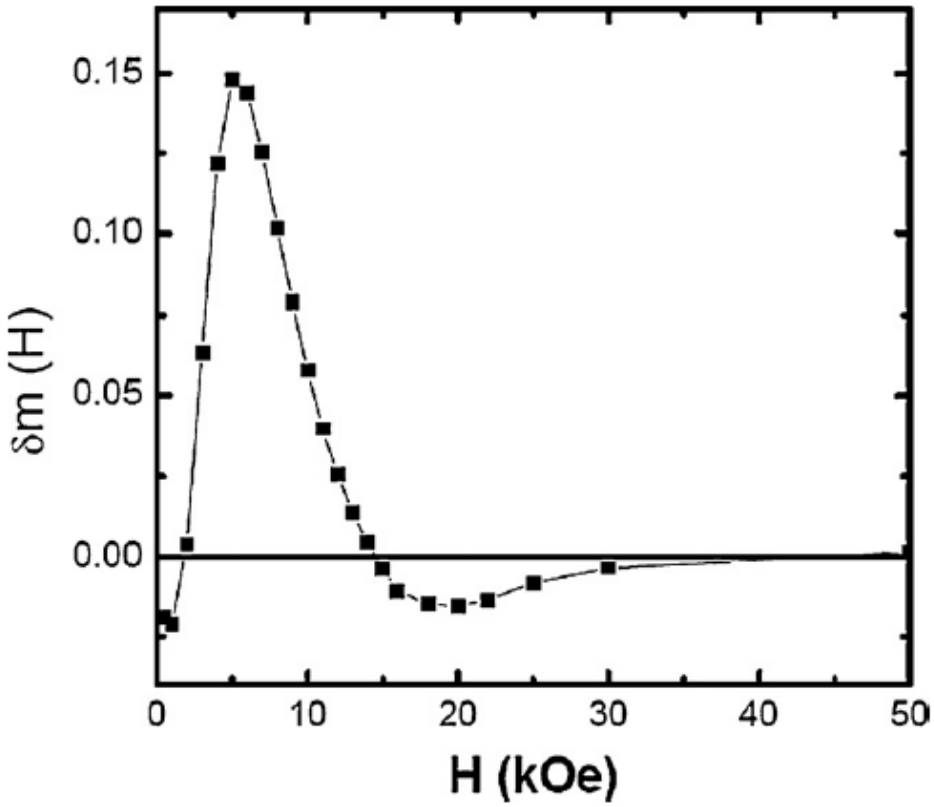

Figure 2.2.2-2 δM curve for exchange-coupled magnetic material. From REF [36]

2.2.2.3 Recoil Loop Analysis

Recoil loop analysis is another method of evaluating exchange-coupling in nano-composite PMs[38], [43], [46]–[49]. Recoil loops are done by first saturating a sample in one direction. A reversal field H_a in the opposite direction is then applied, removed (field taken back to 0Oe) and reapplied. The application of H_a followed by removal and reapplication is repeated for a variety of H_a values. As H is swept from H_a to 0Oe, the magnetization recoil curve is formed. As H is swept from 0Oe to H_a, the demagnetization recoil curve is formed. The area between the recoil magnetization and recoil demagnetization curves, normalized by ½ the hysteresis loop area, is called the recoil area.

Well coupled composite magnets and single phase magnets exhibit recoil loops with little to no openness. Decoupled composite materials typically show larger openness in recoil loops. **Figure 2.2.2-3** shows measured recoil loops for various thicknesses of soft phase, **(a)** being thicker and **(c)** being the thinner. Smaller recoil loop openness is attributed to better coupling with the thinner soft phase dimension. Recoil loop analysis is also useful for looking at the recoil remanence ratio, M_{recoil}/M_r. M_{recoil}, the value of magnetization with 0 Oe field applied following recoil magnetization from H_a to 0 Oe is divided by the magnetic remanence M_r. High recoil remanence ratio suggests resistance to demagnetization and could be used as evidence of exchange-coupling[38].

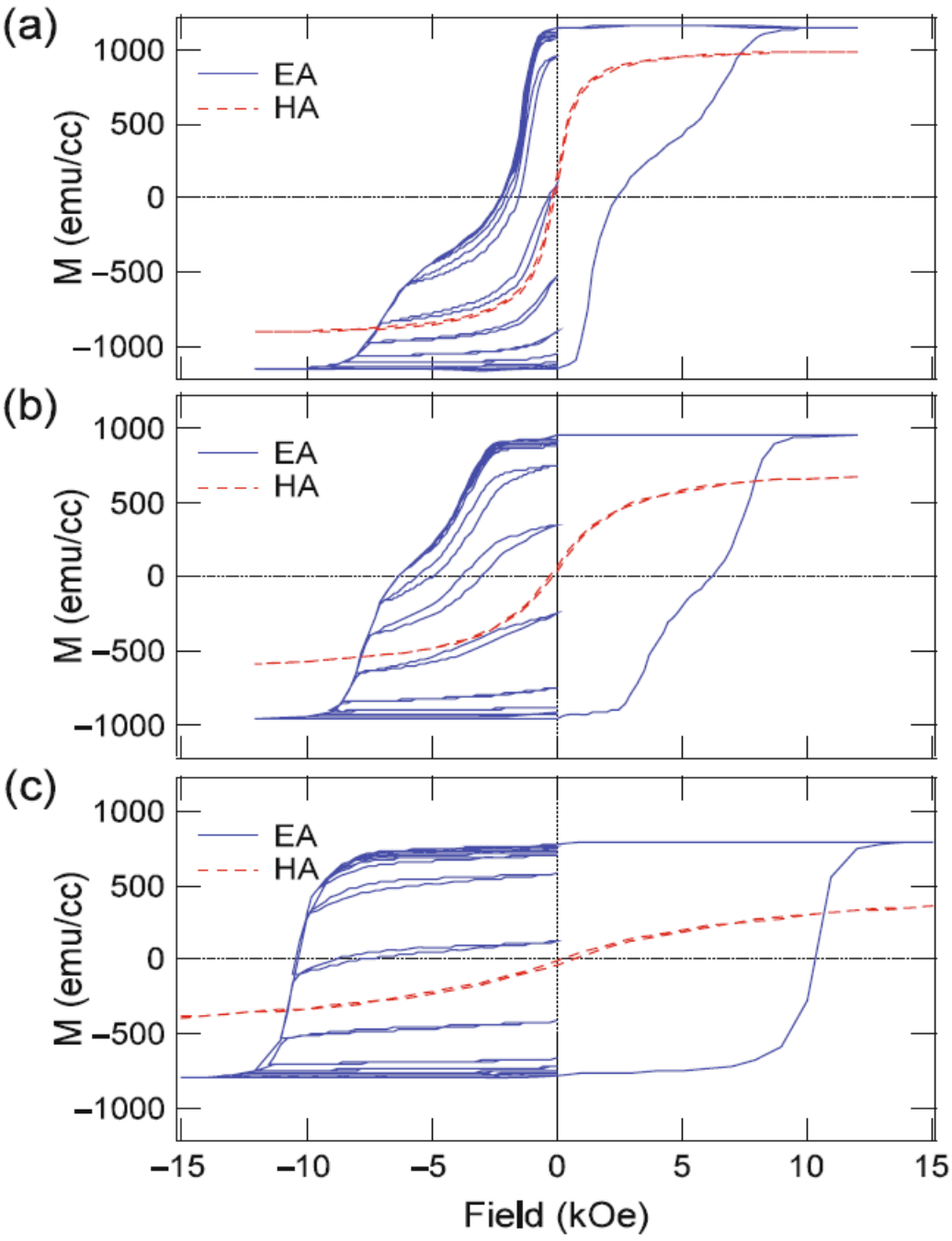

Figure 2.2.2-3 Recoil loop measurements of SmCo/Fe bilayers with varying thickness of soft Phase: (a)20nm, (b)10nm, (c)5nm. From REF [49]

2.2.2.4 First Order Reversal Curve Analysis

First Order Reversal Curve (FORC) analysis has been previously used to evaluate the interaction between magnetic particles[38],[43],[50]. FORC is measured by saturating the material (out of time considerations, maximum H applied is often lower than H required for saturation), then decreasing H to H_a, and ramping H back to saturation through field values H_b with a constant step size shown schematically in **Figure 2.2.2-4**. A set of FORCs is used to calculate FORC distribution, ρ, according to **Equation 2.2.2-3** [51].

$$\rho(H_a, H_b) = -\frac{\partial^2 M(H_a, H_b)}{\partial H_a \partial H_b} \qquad \textit{(Equation 2.2.2-3)}$$

Numerical methods such as FORCinel [52] are used to plot the FORC distribution traditionally as H_c *vs* H_u given by **Equation 2.2.2-4** and **Equation 2.2.2-5**.

$$Hc = \frac{(Hb - Ha)}{2} \qquad \textit{(Equation 2.2.2-4)}$$

$$Hu = \frac{(Ha + Hb)}{2} \qquad \textit{(Equation 2.2.2-5)}$$

Pike *at. al.* first developed FORC analysis in 1999[50]. They used experimental results along with theoretical models to examine how FORC distributions varied for interacting and non-interacting particles, as well as the types of interactions involved. Generally higher values in ρ suggest more ferromagnetic interaction [43], [53]. A large spread in H_u data is indicative of a large mean interaction field, while a small spread is indicative of non-interacting particles, shown in **Figure 2.2.2-5** and **Figure 2.2.2-6** respectively. The location of the distribution hotspot and the slope of the line of contour elongation gives suggestions to the style of inter-particle interaction. Exchange style interaction favors a hotspot displacement bellow the H_u=0 axis and a positive slope of the

line of contour elongation, while dipole-dipole style interaction favors a hotspot displacement above the H_u=0 axis and a negative slope of the line of contour elongation, as shown in **Figure 2.2.2-7** and **Figure 2.2.2-8** respectively. This emerging method of charactering exchange-coupled PMs is more effective than the δM method, as the exchange interaction is often clouded by dipole-dipole interaction when using δM method.

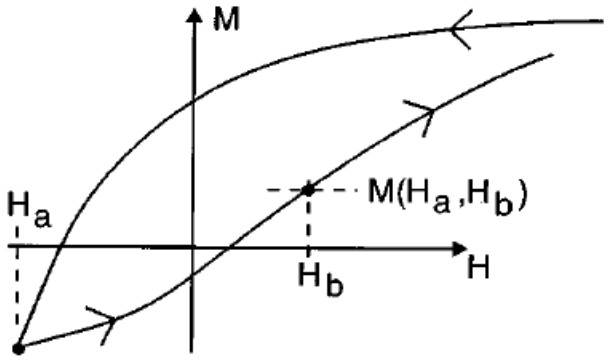

Figure 2.2.2-4 Schematic of a FORC measurement. From REF [50]

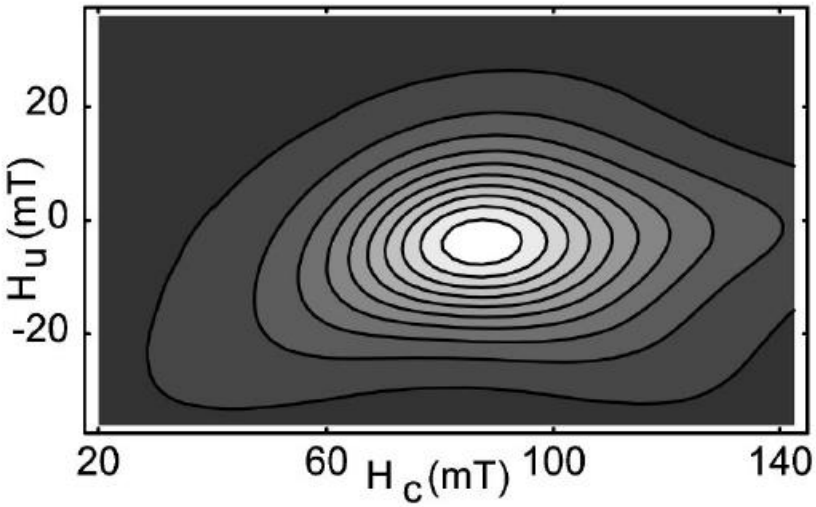

Figure 2.2.2-5 Typical FORC distribution of interacting particles[50]

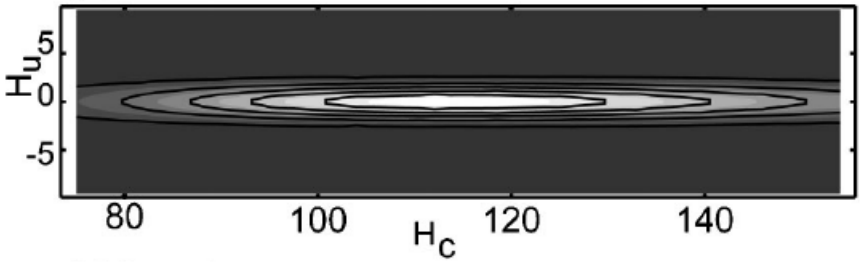

Figure 2.2.2-6 Typical FORC distribution of non-interacting particles. From REF [50]

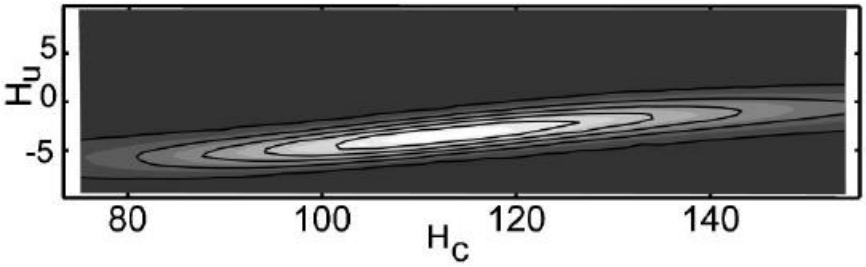

Figure 2.2.2-7 Typical FORC for particles with exchange style interaction. From REF [50]

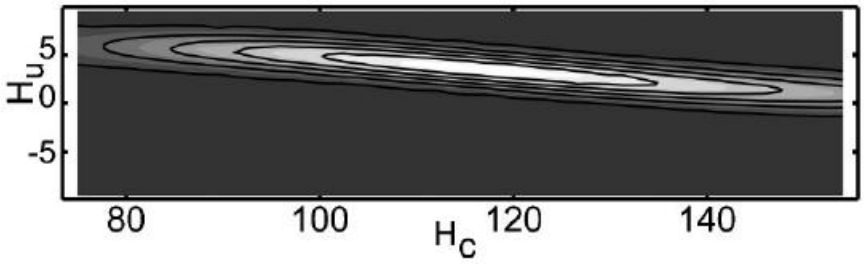

Figure 2.2.2-8 Typical FORC for particles with dipole-dipole style interaction. From REF [50]

2.3 Materials systems studied in this dissertation: selection and microstructural considerations

Haxaferrite PMs make up a bulk amount of magnetic material produced. Discovered in 1951 by Philips Laboratories[17],[19], hexaferrites improved upon the performance of PMs though high coercivity, but relatively low magnetization. $XFe_{12}O_{19}$ (X is Sr, Ba or Pb) materials make up the class of hexaferrites. At 300,000 tons/year, $BaFe_{12}O_{19}$ account for

roughly 50% of PM material synthesized [54]. Importantly, RE and precious metal free, containing mostly Fe and O, $SrFe_{12}O_{19}$ was chosen as the hard phase material for this study.

Fe is one of the most abundant element on earth, as seen in **Figure 2.3-1**. It has an incredibly high M_s of 1672 emu/cm^3 [55]. Fe is an excellent soft phase candidate for a RE and precious metal free exchange coupled PM.

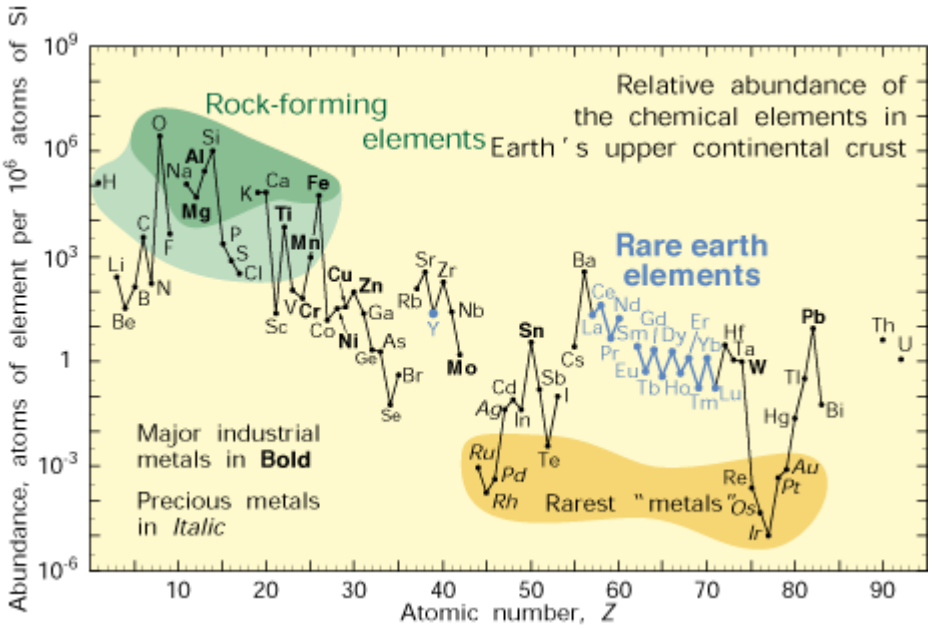

Figure 2.2.2-1 Abundance of elements on earth. From REF [56]

2.3.1 Length Scale Considerations

H_c of the hard magnetic phase in an exchange-coupled PM could be tailored by microstructure. According to literature, SFO has a single domain size of about 500nm [57]. The exchange length, L_{ex}, is about equal to the length of the domain wall, δ, which is calculated by **Equation 2.3.1-1**. The exchange constant for SFO is ~3.7x10^{-7} erg/cm [54]

while the anisotropy constant (using Barium Ferrite for this approximation) is ~$3.5x10^6$ erg/cm^3 [58]. The exchange length of SFO is calculated to be ~10.5nm. This means for ideal exchange-coupling, 500nm SFO grains should interact with 10.5nm Fe grains. In order to maximize the inter-phase surface area, a core/shell microstructure, with SFO as the core and Fe as the shell, is applied for this project.

2.4 Bottom-up Approach to Exchange-coupling

Much research on exchange-coupled PMs focused on thin films, ribbons and powders synthesized through top-down methods such as mechanical milling and melt-spinning. These approaches, although successful, are not very scalable. A simple and scalable bottom up approach, using homogeneous precipitation as a way to synthesize the soft phase precursor, and subsequent reduction of the precursor into soft phase was implemented in this study.

2.4.1 Colloid Synthesis

Homogeneous precipitation is one of the most common methods of synthesizing "monodispersed" colloids in chemistry [59]. It has been used in the past to synthesize a variety of different materials[60]–[63]. In particular, previous work based on precipitation from homogeneous solution had shown successful precipitation of Fe-O and Fe-O-H [59], [62], [64]. Although several metal salts are available as sources of metal cations, $Fe(NO_3)_3$ was used in this study, due to the ease of removal of NH_4NO_3, which is formed as bi-

product. Urea is used for controlled release of OH^- ions, aiding the hydrolysis of metal cations. In water, urea decomposes into NH_4OH and CO_2 according to **Equation 2.4.1-1**.

$$(NH_2)_2CO_{(aq)} + 3H_2O_{(l)} \rightarrow 2NH_4OH_{(aq)} + CO_{2(g)} \quad \textit{(Equation 2.4.1-1)}$$

Metal salt, $Fe(NO_3)_3$ was used as a source of metal ions in solution. The metal ions will precipitate as metal hydroxide, donating their anion to the NH_4 group, according to **Equation 2.4.1-1**.

$$Fe(NO_3)_{3(aq)} + 3NH_4OH_{(aq)} \rightarrow Fe(OH)_{3(s)} + 3NH_4NO_{3(aq)} \quad \textit{(Equation 2.4.1-2)}$$

2.5 Sintering

Sintering developed its roots with ancient brick making. Today the sintering industry includes powder metallurgy, ceramics, cemented carbides, etc [65]. In general, sintering involved the consolidation of fine particles into bulk samples. The driving force behind sintering is the reduction of surface area and along with it the surface free energy. Capillary pressure due to surface curvature at the contact points of particles drives sintering[66]. Typically there is competition between densification, the movement of the centers of two particles closer together, and coarsening, the growth of the neck region between particles[66]. Volume diffusion is not very active at low temperatures, and most mass transport is done by surface diffusion, causing grain growth and coarsening. Due to slow heating rates of traditional sintering techniques, synthesis of materials with nano-scale grains has been a challenge.

2.5.1 Current Activated Pressure Assisted Densification (CAPAD)

Current Activated Pressure Assisted Densification (CAPAD) delivers very fast heating rates via joule heating. This is done by running current directly through and/or around the powder being processed. Pressure is simultaneously applied in order to create high density samples quickly, typically in a matter of minutes. High heating rates, typically ~ 200°C/min are used. Current is ran through a water cooled electrode to a graphite diffuser, then to a plunger and die assembly and back out though another graphite diffuser and electrode, as shown in **Figure 2.5.1-1**. Powder is loaded into a graphite die and plunger set. Graphite is used due to its excellent electrical and thermal conductivities. In this study, the powder is densified under relatively high pressure, 500 MPa, temperature, 300°C to 500°C. The custom built CAPAD device in this study, has a load frame capable of delivering 160 kN and a power supply capable of current up to 6000A.

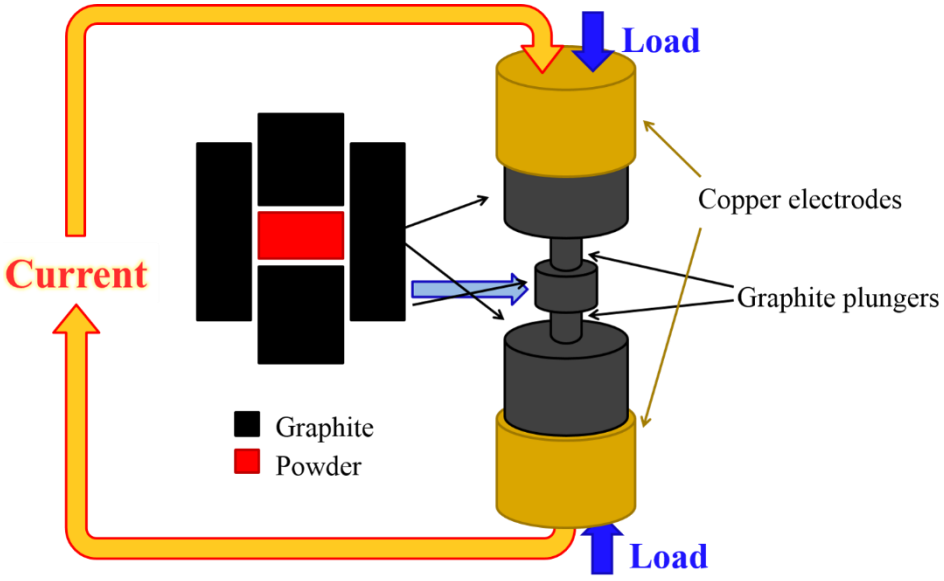

Figure 2.5.1-1 CAPAD schematic

3 Exchange-Coupled Nano-Composite Magnetic Powders

3.1 SFO/Fe(Fe-O) Material System

Research conducted started with the use of common ceramic magnetic material, SFO as the hard phase. SFO does not have very high energy product, compared to RE, precious metal or even magnets made of earth abundant materials (Alnico, etc). SFO does however have one of the higher H_c values among materials made of abundant materials. Fe, one of the most abundant elements on earth, with its very high magnetization could improve the properties of SFO vastly, if exchange-coupled with it. The goal of this part of the project was to achieve improved energy product, compared to as-received SFO, by taking advantage of exchange-coupling.

3.1.1 Procedure

3.1.1.1 Synthesis

Precipitation by decomposition of urea, explained in detail in Section 2.4.1, was chosen as the method of depositing Fe-O/Fe-O-H soft phase precursor onto SFO powder ($SrFe_{12}O_{19}$, Nanostructured & Amorphous Materials Inc). The as-synthesized SFO powder consists of high aspect ratio flake like particles with average dimensions of 1.12 μm and 0.16 μm. 28.7 mmol of $Fe(NO_3)_3$ (Sigma Aldrich >98%) was mixed with 167 mmol of $CO(NH_2)_2$, Urea (Sigma Aldrich >99.5%). The mixture was then titrated into a slurry of 1.58 mmol of SFO and 50mL of H_2O at 90 ^oC over periods of 2 hours. The resulting mixture was cooled quickly to prevent further particle growth.

In order to understand the soft phase precipitation process, experiments without SFO were studied, (soft phase only) in which no titration is used. 28.7 mmol of $Fe(NO_3)_3$ was mixed with 167 mmol of Urea and held at 90 ^oC for 2 hours. The resulting homogeneous precipitation creates nano-scale particles of the soft magnetic phase precursor.

In both the composite and soft phase cases, the resulting particles were centrifuged, washed with ultra-high pure water and centrifuged again. The powder and liquid was separated by decantation. The powder was dried at 80 ^oC in a vacuum furnace for 24 hours to ensure no moisture remains. The dried agglomerates were then are broken by mortar and pestle. The powders were then treated in a tube furnace under forming gas (5% H_2, 95 % N_2) at temperatures ranging from 300 ^oC to 500 ^oC with 1 hour ramp and no hold time. The resulting powder was handled in Argon atmosphere to avoid oxidation.

The yield of Fe-O precipitation was obtained by the gravimetric analysis based method. The collected liquid, left over from precipitation, was dried and calcined at 800 ^oC for 6 hr in air atmosphere. The residue remaining after calcination was αFe_2O_3 single phase which was confirmed by X-ray diffraction analysis. The amount of αFe_2O_3 was used to calculate yield of the precipitation process.

3.1.1.2 Composition and Microstructural Characterization

The phase composition was characterized with X-ray diffraction (XRD) (PANalytical Empyrean Diffractometer with Cu Kα X-ray source λKα1=1.54056 Å λKα2=1.54440 Å using 0.01313o step size). In order to provide an estimate of phase

composition ratio, XRD peak intensities ratio was calculated by taking the highest intensity peak of one phase and dividing it by the sum of the highest intensity peaks of all detectable phases and multiplying by 100. The particle morphology was characterized by Scanning Electron Microscopy (SEM) (Philips XL30).

3.1.1.3 Magnetic Characterization

Magnetic properties were measured using a Vibrating Sample Magnetometer (VSM) (Lakeshore 7400 Series) at room temperature. Powders were packed into polycarbonate capsules, and the powder was locked into place by melting *eicosane* (organic substance with a melting point ~40 ^{o}C) around it. Hysteresis loop measurements using field values of up to 1.7 T were obtained in order to plot mass normalized magnetization, σ [emu/g] *vs.* applied field, H [Oe]. We refer to these measurements as hysteresis loops. Coercivity, H_c [Oe], remanence magnetization M_r [emu/g] and saturation magnetization M_s [emu/g] was extracted from the σ *vs. H* hysteresis curves. In calculating M_s, the non-saturating slope (due to SFO and Fe_3O_4 being ferrimagnetic) was subtracted. Energy product, $(BH)_{max}$ [MGOe] was calculated assuming full density of SFO*.

First order reversal curve (FORC) measurements were done by ramping the field to 0.6 T then decreasing the magnetic field to a reversal field with value of H_a and ramping back up to 0.6 T through field values, H_b with a step size of 200 Oe. Magnetization as a function of H_a and H_b, $M(H_a,H_b)$, is recorded. This procedure was repeated in order to measure a collection of first order reversal curves for reversal fields in 200 Oe intervals from 5800 Oe to -6000 Oe. FORC distribution, ρ is calculated using **Equation 3.1.1-1**.

FORCinel was used to calculate the FORC distribution and plot it as a function of (H_c, H_u), *Hc* and *Hu* are given in **Equation 3.1.1-4** and **Equation 3.1.1-5**.

Recoil loop measurements were done by first ramping magnetic field to 1.7 T in order to bring the sample to saturation (ignoring the non-saturating component due to SFO and Fe_3O_4 being ferrimagnetic). A Reversal field, H_a, was applied, removed (field taken to 0 Oe) and reapplied (field taken back to H_a). H_a values were varied from 100 Oe to 1400 Oe in 100 Oe increments. Measurements of magnetization, σ, were taken from H_a to 0 Oe, forming the recoil magnetization curve, and likewise from 0 Oe back to H_a, forming the recoil demagnetization curve. The area between recoil magnetization and recoil demagnetization curves was calculated using numerical methods. Normalized recoil loop area was calculated by dividing the area between recoil magnetization and recoil demagnetization curves by ½ of the total area of the sample's customary hysteresis loop area (also calculated using numerical methods). M_{recoil} is the value of magnetization with 0 Oe field applied following recoil magnetization from H_a to 0 Oe. Recoil remanence ratio M_{recoil}/M_r was calculated by taking the M_{recoil}, values and dividing it by the magnetic remanence M_r (from the customary loop obtained as described above).

3.1.2 Results

3.1.2.1 Fe Based Soft Phase

Soft phase precursor powders (Fe-O/Fe-O-H) have been synthesized using homogeneous precipitation by decomposition of Urea. **Figure 3.1.2-1 (a), (b)** shows the microstructure of as-precipitated soft phase precursor. Particle size <100 nm is observed in

the as-precipitated soft phase precursor. **Figure 3.1.2-1 (c), (d)** shows the microstructure of soft phase after reduction at 400 ^{o}C. Particle size <200 nm is observed. Particle size increased and necking is seen after the reduction process.

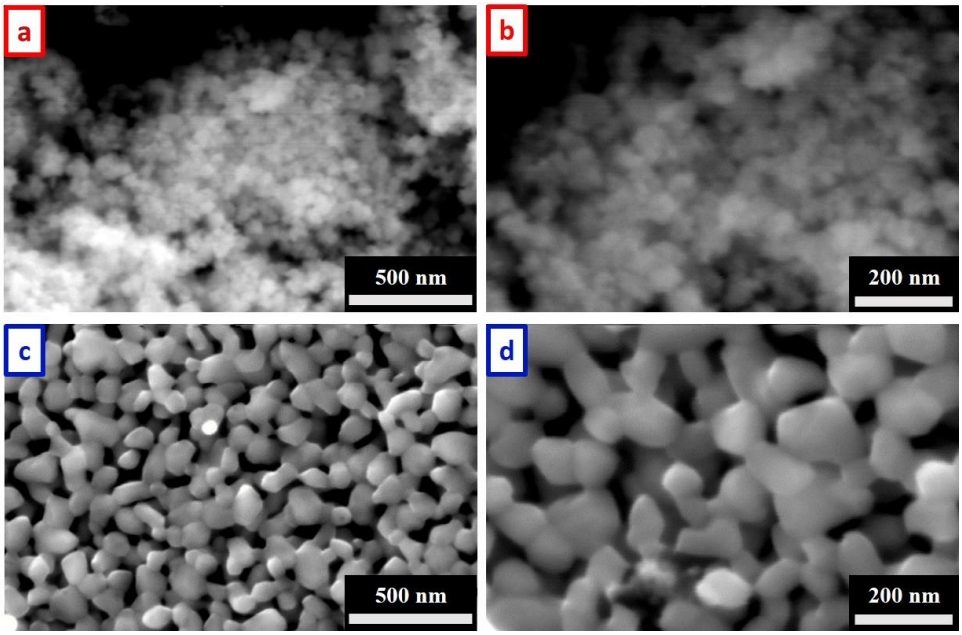

Figure 3.1.2-1 (a), (b) SEM micrographs of homogeneously precipitated Fe based soft phase precursor; (c), (d) SEM micrographs of soft phase reduced at 400 ^{o}C

XRD waterfall plots of as-precipitated as well as reduced (at various temperatures) Fe-O/Fe-O-H soft phase precursor and soft phase are shown in **Figure 3.1.2-2**. The as-precipitated precursor has high background intensity at low angles and displays peaks belonging to αFe_2O_3 and $\alpha FeO(OH)$. Increasing reduction temperature causes peaks of $\alpha FeO(OH)$ and αFe_2O_3 to disappear, while Fe_3O_4 peaks appear. Even higher reduction temperature causes the peaks of Fe_3O_4 to diminish while peaks belonging to metal αFe appear.

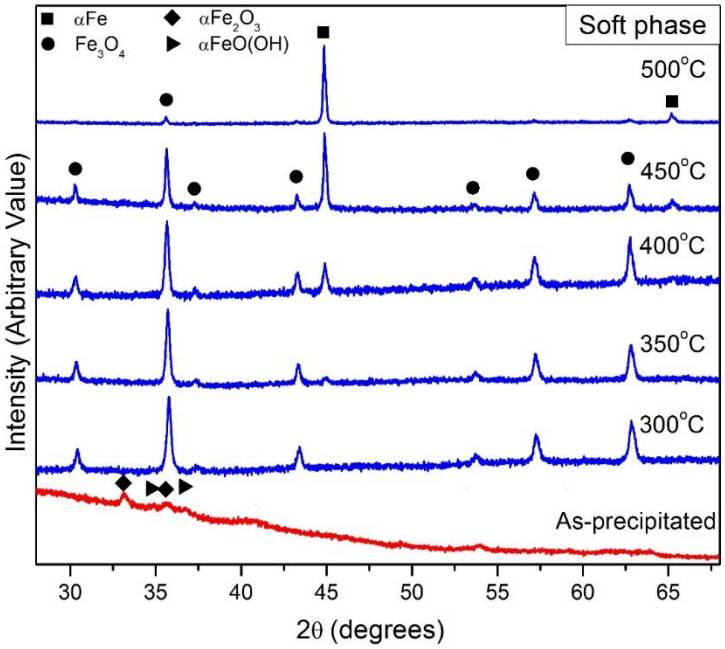

Figure 3.1.2-2 X-ray diffraction patterns for the soft Fe based phase after precipitation as well as at reduction temperatures 300-500 °C.

XRD peak intensity ratio vs. reduction temperature of the Fe based soft phase is shown in **Figure 3.1.2-3**. The XRD peak intensity ratios of αFe_2O_3 and αFeO(OH) account for 100 % of the peak intensities before reduction, but completely disappear by reduction temperature of 300 °C. The XRD peak intensity ratio of Fe_3O_4 makes up 100 % of the peak intensities at the reduction temperature of 300 °C and diminishes gradually as the reduction temperature is increased from 300 °C to 500 °C. Metal αFe peak intensity ratio appears at 350 °C and increases with reduction temperature. αFe peak intensity ratio becomes the largest peak intensity ratio once the reduction temperature reaches 450 °C.

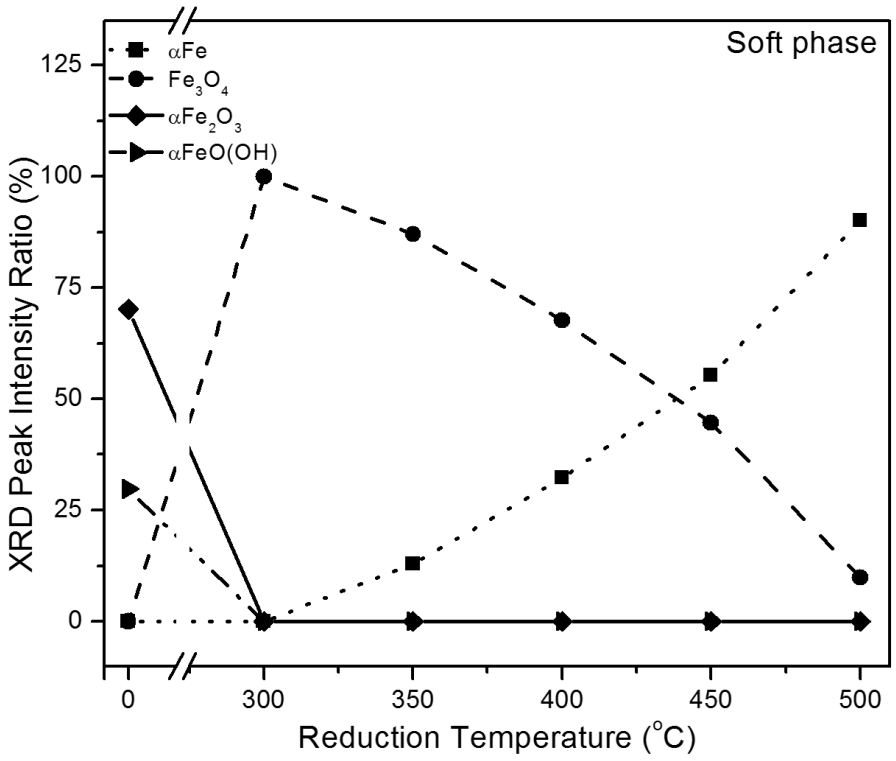

Figure 3.1.2-3 XRD peak intensities ratios of Fe based soft phase at various reduction temperatures. The peak intensity ratio is the ratio of the most intense peak of a particular phase to the sum of the intensities of the most intense peaks of all identifiable phases. The most intense peaks for αFe, Fe_3O_4, αFe_2O_3 and αFeO(OH) are from the (110), (311), (104) and (101) planes, respectively.

M_s of the soft phase particles at various reduction temperatures is displayed in **Figure 3.1.2-4**. Post precipitation, (0 ºC), M_s is very small. The magnetization increases from 0.4 to 93 emu/g as the powder is reduced at 300 ºC. M_s stays fairly constant at reduction temperatures 300 ºC to 400 ºC. *Ms* increases further as the reduction temperature is increased to 450 ºC and 500 ºC.

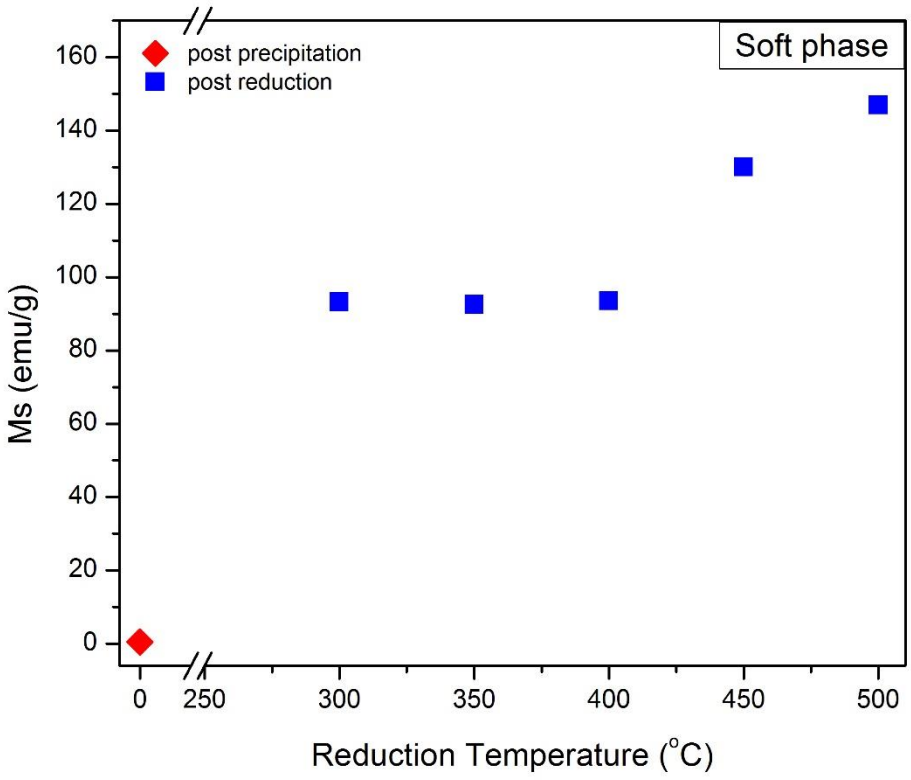

Figure 3.1.2-4 Saturation magnetization of the Fe based soft phase at various reduction temperatures.

3.1.2.2 SFO/Fe Based Composite

Fe-based soft phase was precipitated heterogeneously on the surface of SFO. The calculated yield of the precipitation process, based on the mass of Fe was 62 %. SEM micrograph is the as received SFO **(a-c)**, SFO/Fe based composite after precipitation **(d-f)** and SFO/Fe based composite after reduction **(g-i)** is shown in **Figure 3.1.2-5**. As received hexagonal SFO flakes, corresponding to SFO's crystal structure, have flat/smooth/featureless surfaces. After precipitation, features <100 nm appear on the surface of SFO. After reduction, features <200 nm are formed on the surface of SFO.

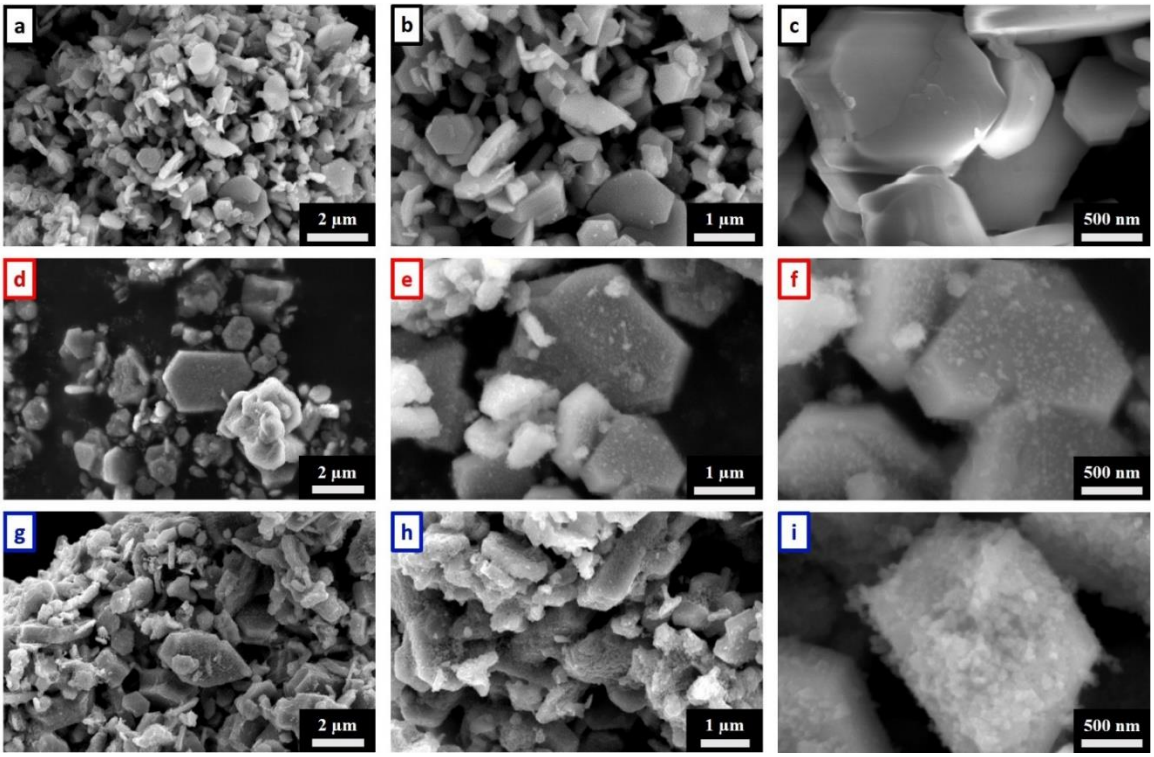

Figure 3.1.2-5: (a), (b), (c): SEM micrographs of single phase SFO powder. (d), (e), (f): SEM micrographs of SFO/Fe based composite powder after precipitation procedure. (g), (h), (i): SEM micrographs of SFO/Fe based composite powder after reduction at 400 ^{o}C.

XRD waterfall plots of as-precipitated as well as reduced (at various temperatures) SFO/Fe based composite are shown in **Figure 3.1.2-6**. The as-precipitated composite displays peaks belonging to αFe_2O_3 and SFO. At the reduction temperature of 300^{o}C the composite shows XRD peaks belonging to αFe_2O_3, SFO and Fe_3O_4. Increasing reduction temperature peaks of αFe_2O_3 to disappear, and peaks of Fe_3O_4 to increase. Even higher reduction temperature causes decrease in peaks belonging to SFO and an increase in peaks belonging to Fe_3O_4.

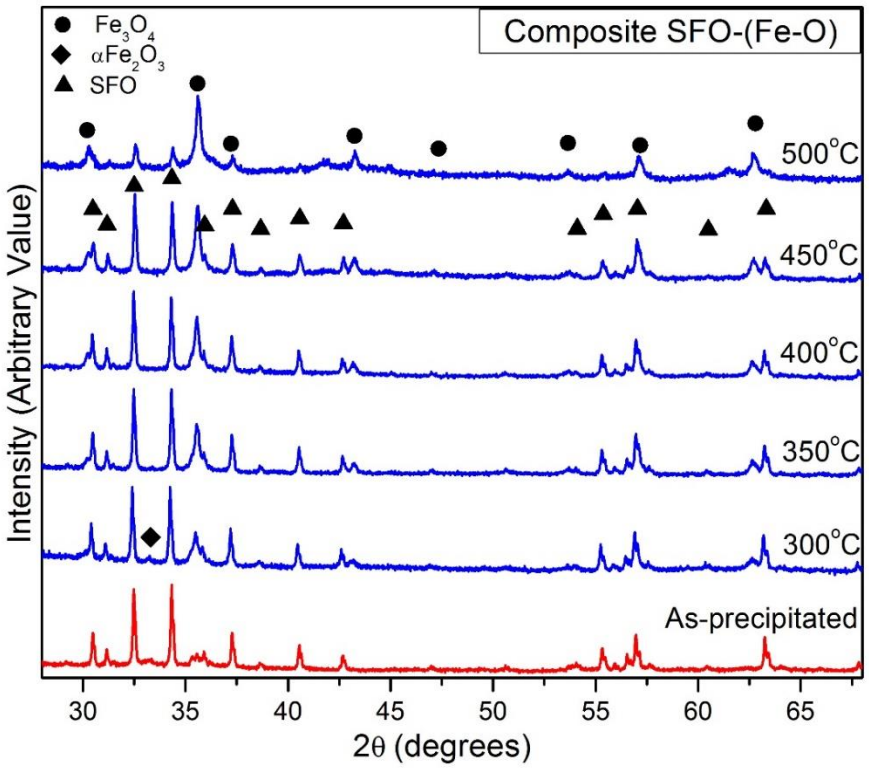

Figure 3.1.2-6 X-ray diffraction patterns for the SFO/Fe based composite after precipitation procedure as well as at reduction temperatures 300-500 °C.

XRD peak intensity ratio vs. reduction temperature of the SFO/Fe based composite is shown in **Figure 3.1.2-7**. The XRD peak intensity ratios of αFe_2O_3 and SFO account for 100% of the peak intensities before reduction. The XRD peak intensity ratio of αFe_2O_3 decreases and disappears at the reduction temperature of 350 °C. The XRD peak intensity ratio of Fe_3O_4 appears at 300 °C and increases until it becomes the major peak intensity at 500 °C. SFO peak intensity ratio decreases as the composite is reduced at 300 °C. SFO peak intensity ratio further decreases as the reduction temperature is increased from 350 °C to 500 °C.

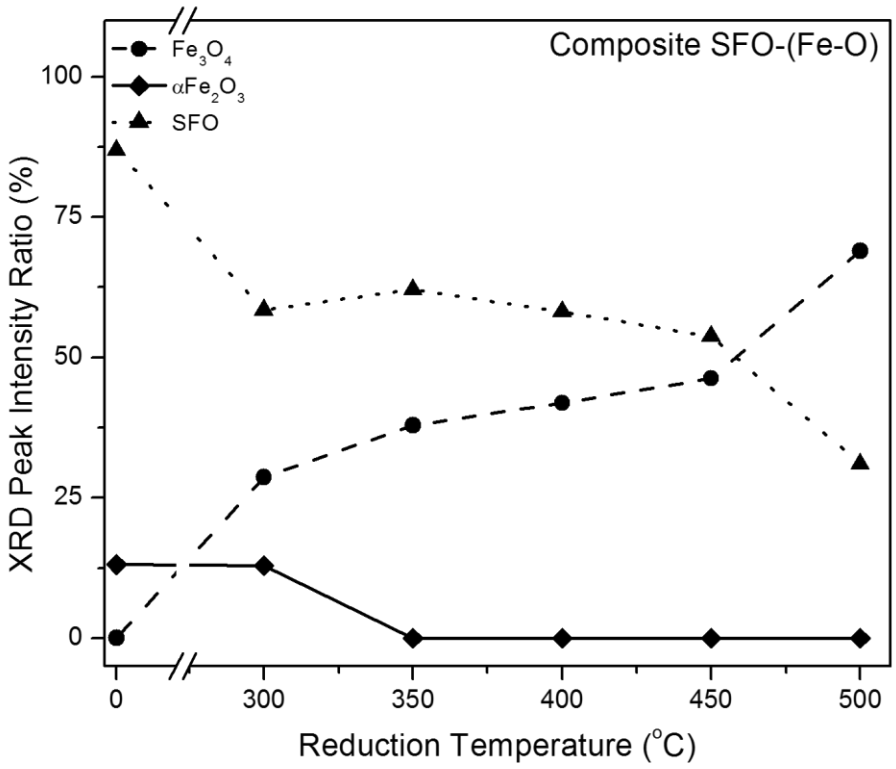

Figure 3.1.2-7 XRD peak intensities ratios of SFO/Fe based composite at varying reduction temperatures. The peak intensity ratio is the ratio of the most intense peak of a particular phase to the sum of the intensities of the most intense peaks of all identifiable phases. The most intense peaks for Fe_3O_4, αFe_2O_3 and SFO are from the (311), (104) and (107) planes, respectively.

Magnetic properties of the SFO/Fe based composite, including H_c, M_r, M_s *and* BH_{max}, as function of reduction temperature, are summarized in **Figure 3.1.2-8**. After the precipitation procedure, all magnetic properties of the SFO/Fe based composite drop. As the composite is reduced, magnetic properties increase and reach a peak at either 350 or 400 °C, depending on the property. Magnetic properties decrease as the reduction temperature is increased further than 400 °C.

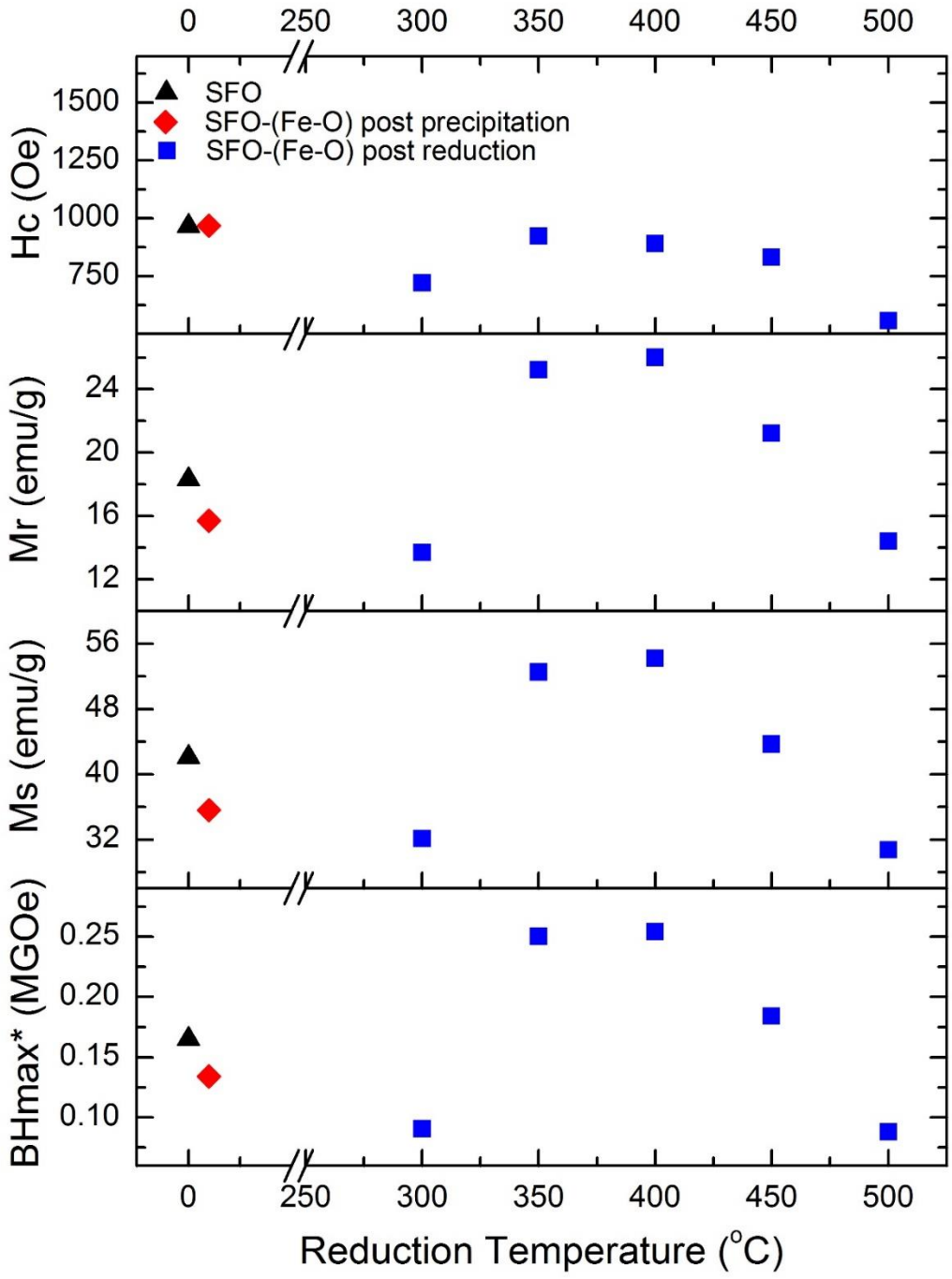

Figure 3.1.2-8 SFO/Fe based composite magnetic properties (coercivity, remnant magnetization, saturation magnetization, energy product).*

They hysteresis loop of the SFO/Fe based composite, reduced at 400 ºC (so really SFO/Fe_3O_4) and the hysteresis loop of the SFO powder is displayed in **Figure 3.1.2-9**. The loop of the composite material has a smooth transition from first to second quadrant, displaying no kink.

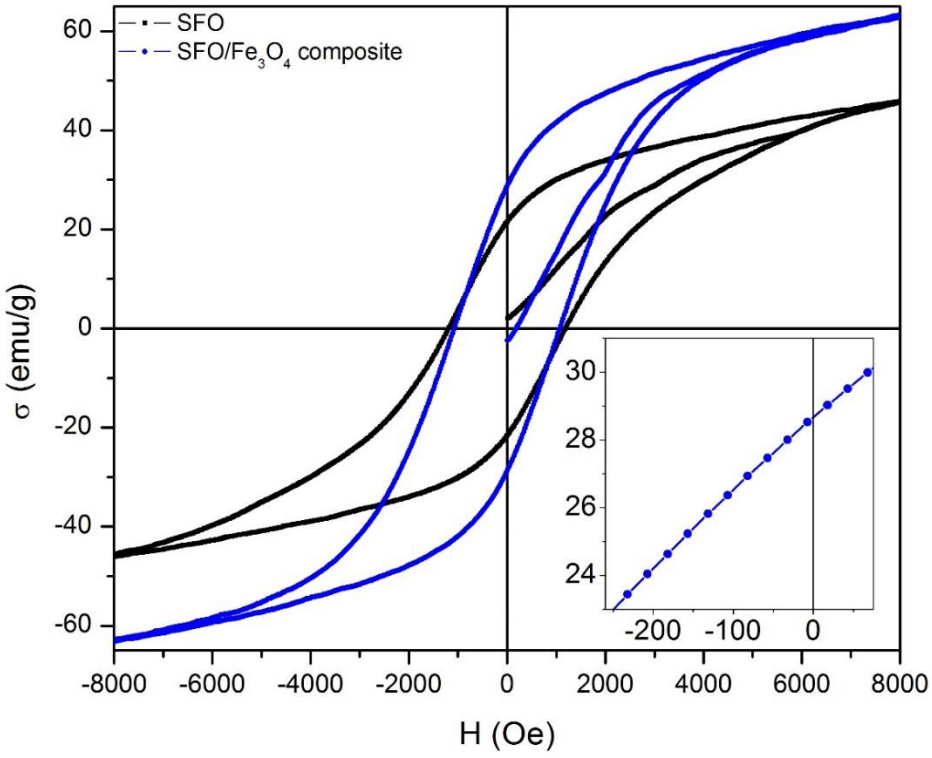

Figure 3.1.2-9 SFO/Fe_3O_4 composite (reduced at 400ºC) hysteresis loop compared to single phase SFO.

Figure 3.1.2-10 displays the FORC diagram for **(A)** SFO powder and **(B)** SFO/Fe based composite reduced at 400 ºC (so really SFO/Fe_3O_4). There are clear differences in the two diagrams. The H_u spread of data is much larger in the composite case. The

maximum distribution value is higher in the SFO/Fe_3O_4 powder compared to SFO powder. Both figures display a single "hot spot".

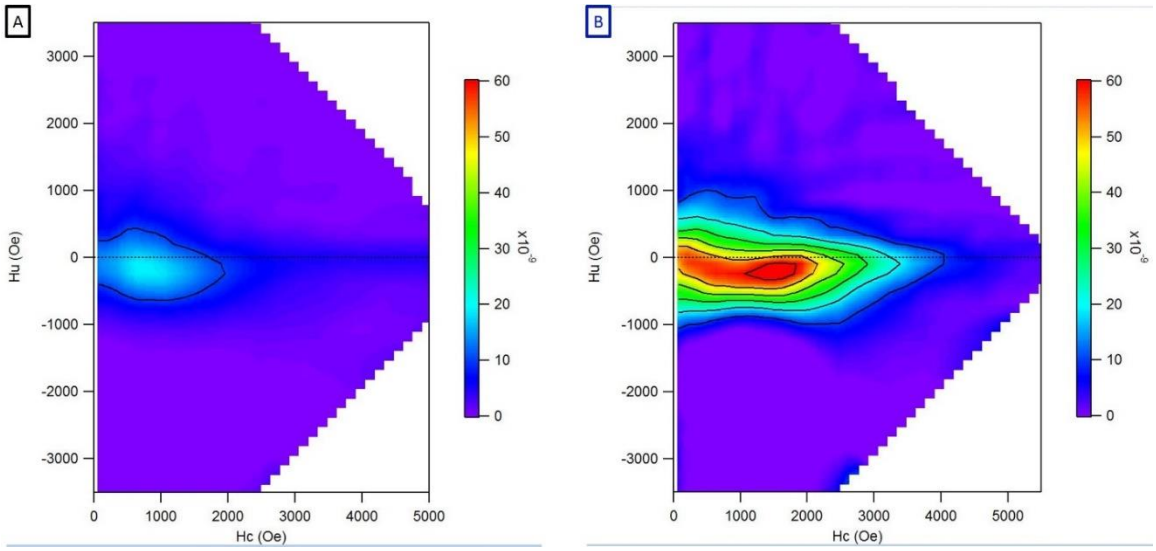

Figure 3.1.2-10 First order reversal curve (FORC) diagrams for (A) single phase SFO and (B) SFO/Fe_3O_4 composite (reduced at 400°C).

Figure 3.1.2-11 displays recoil loop measurements **(A)** for SFO powder and **(B)** for SFO/Fe based composite, reduced at 400 °C (so really SFO/Fe_3O_4). Normalized recoil loop area as a function of H_a for both SFO powder and SFO/Fe_3O_4 composite is shown in **Figure 3.1.2-11 (C)**. The normalized recoiled loop area is nearly zero in the case of both the SFO and SFO/Fe_3O_4 powder at low H_a. The loop area increases with increasing -H_a. The normalized recoil loop area is very similar for SFO powder and SFO/Fe_3O_4 powder at the same H_a value. **Figure 3.1.2-11 (D)** shows M_{recoil}/M_r as a function of H_a. M_{recoil}/M_r decreases with increasing -H_a. M_{recoil}/M_r is higher for the SFO/Fe_3O_4 composite than SFO powder at the same H_a value.

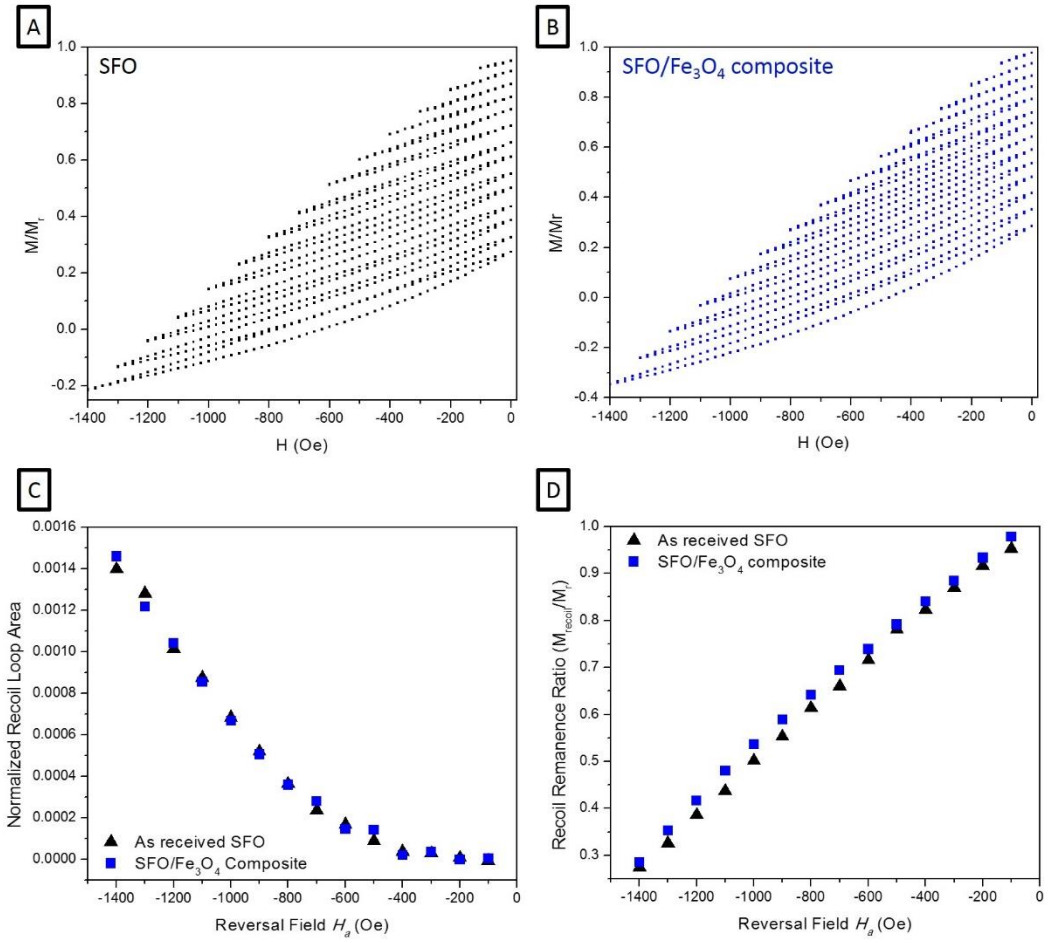

Figure 3.1.2-11 (A) Single phase SFO recoil loop measurement. (B) SFO/Fe_3O_4 composite (reduced at 400°C) recoil loop measurement. (C) Normalized recoil loop areas (normalized by ½ full hysteresis area) for pure SFO and SFO/Fe_3O_4 composite (reduced at 400°C). (D) Recoil remanence ratio for pure SFO and SFO/Fe_3O_4 composite (reduced at 400°C).

3.1.3 Discussion

3.1.3.1 Fe Based Soft Phase

In order to understand the composite material system, it is vital to understand the behavior of individual constituents. Characteristics of just the soft phase were therefore investigated, prior to investigating the composite system. Micrographs shown in **Figure**

3.1.2-1 provide evidence of the benefit of the precipitation procedure. Nano-scale mixing is necessary for effective use of exchange-coupling. The relatively loose (low degree of agglomeration) particles, **Figure 3.1.2-1 (a), (b)**, with gran sized <100 nm are excellent candidate soft phase precursors for exchange-coupled composite. Soft phase precursor particles reduced at 400 ^{o}C, **Figure 3.1.2-1 (c), (d)**, exhibit grain growth, but stay in the nano-range, important for taking full advantage of exchange-coupling.

The as precipitated Fe based soft phase precursor particles exhibit low degree of crystallinity, given evidence of by the high XRD background intensity at low angles, seen in **Figure 3.1.2-2 (As-precipitated)**. The as-precipitated powder is mixture of αFe_2O_3 and $\alpha FeO(OH)$ phases, observed previously in literature[67]. As the powder is reduced at temperatures 300 ^{o}C - 500 ^{o}C, the amorphous high background intensity, along with αFe_2O_3 and $\alpha FeO(OH)$ peaks disappear **Figure 3.1.2-2 (300 ^{o}C to 500 ^{o}C)**. Increasing reduction temperature causes the decomposition of $\alpha FeO(OH)$ and reduction of αFe_2O_3 to Fe_3O_4. At reduction temperatures of 350 ^{o}C and above, Fe_3O_4 undergoes further reduction to metal αFe. Similar findings have been reported previously in the literature[68], [69].

The ratio of peak intensities can give clues to the evolution of phases in the material as the reduction temperature increases. Increasing peak intensity ratio corresponds to an increasing fraction of the particular phase. **Figure 3.1.2-3** shows that by the reduction temperature of 300 ^{o}C all the initially precipitated phases (αFe_2O_3 and $\alpha FeO(OH)$) have disappeared. The volume fraction of Fe_3O_4 in the soft phase decreases with reduction temperature, as the volume fraction of metal αFe increases. These results are consistent with **Figure 3.1.2-4**, *Ms* at various reduction temperatures. Before reduction, **Figure 3.1.2-**

4 (0 ºC), since the powder is mostly antiferromagnetic αFe_2O_3 and αFeO(OH), *Ms* is very low. At the reduction temperature of 300 ºC, the material is mostly cubic Fe_3O_4, which has a modest saturation magnetization of 93 emu/g. As the metal, αFe, replaces Fe_3O_4 as the primary phase at reduction temperature of 450 ºC and above (**Figure 3.1.2-3)**, *Ms* improves further, to a very high 147 emu/g at reduction temperature of 500 ºC (**Figure 3.1.2-4)**.

3.1.3.2 SFO/Fe Based Composite

The synthesis technique investigated for soft phase is applied to precipitate soft phase directly on SFO particles. Single-phase SFO is consists of relatively smooth, hexagonally faceted flakes, corresponding to its crystal structure (**Figure 3.1.2-5 (a), (b) and (c)**). As result of the precipitation procedure, nano-scale features are visible at the surface of SFO (**Figure 3.1.2-5 (d), (e) and (f)**). After reduction at 400 ºC, there is not much change at low magnification, in the SFO/Fe based composite particles (**Figure 3.1.2-5 (g), (h)**). There does not appear to be much sintering between the composite particles at this temperature. However, higher magnification, (**Figure 3.1.2-5 (i)**), reveals that the surface of SFO is changed drastically. The precipitated material on the surface of SFO has sintered together. Necking and grain growth behavior is observed.

Yeild of the precipitation procedure was calculated to be 62 % based on the amount of Fe deposited, for this sample reduced at 400 ºC. Thickness of the soft phase layer was calculated to be 43 nm (see **Sample Soft Phase Thickness Calculation** in **Appendix**). This result is in agreement with visual observation of reduced SFO/Fe based composite micrographs.

The as-precipitated SFO/Fe based composite displays XRD patterns of SFO and a small peak of αFe_2O_3. This suggests that SFO was not significantly damaged during the precipitation process (**Figure 3.1.2-6 As-precipitated**). As the composite is reduced at 300 ^oC, peaks of Fe_3O_4 appear. The evolution of the peak intensities is more easily appreciated in **Figure 3.1.2-7**. As the reduction temperature increases, the XRD peak intensity ratio of SFO decreases, while the XRD peak intensity ratio of Fe_3O_4 increases, suggesting a reaction between SFO and precipitated material. Of note, in the absence of precipitated material, SFO is resilient to reduction, and at reduction conditions at 500 ^oC, SFO remain phase-pure. Information gathered from reduction of soft phase suggests that at the reduction temperature of 500 ^oC, the soft phase become mostly αFe (**Figure 3.1.2-3**). However in the composite case, at reduction temperature of 500 ^oC the composite is mostly Fe_3O_4. This suggests that as the soft phase shell of the composite is reduced by forming gas, oxygen moves from the hard phase core, shell-ward, causing the decomposition of SFO.

Due to the very narrow, or possibly overlapping (impossible to achieve) processing window during which reduction of Fe_3O_4 is favorable, while the solid state reaction between Fe_3O_4 and SFO is not favorable, it was not possible to create an oxide/metal composite. However, the severity of the solid state reaction between SFO and Fe_3O_4 suggests a very intimate interphase between the two oxides, creating a very well interphased oxide/oxide composite. Soft phase only samples containing mostly Fe_3O_4 show a relatively high *Ms* <90 emu/g (**Figure 3.1.2-4 300 ^{o}C-400 ^{o}C**), compared to SFO's *Ms*

of 42 emu/g. A well interphased SFO/Fe_3O_4 composite has high potential at improved magnetic properties compared to just the hard phase SFO material.

Magnetic properties of SFO used in this study, as well as composite powder are displayed in **Figure 3.1.2-8**. The single phase SFO powder has coercivity, H_c, remanence magnetization, M_r, saturation magnetization, M_s and energy product, $(BH)_{max}$ values of 967 Oe, 18.3 emu/g, 42 emu/g and 0.165 MGOe, respectively. Of note, since the energy product is based on volume normalized magnetization, the $(BH)_{max}$ values were calculated assuming full density of 5.1 g/cm^3 for SFO[70]. While better properties of SFO have been reported, this work focuses on the improvement of properties compared to starting powder, in contrast to aiming for the highest possibly $(BH)_{max}$. Composite energy product higher than SFO's 0.165 MGOe would mean success for this study.

SFO/Fe based composite pre-reduction shows decreased magnetic properties (**Figure 3.1.2-8)**. This is likely due to the dilution effect caused by the precipitation of antiferromagnetic αFe_2O_3 on the surface of SFO. Initially, increasing the reduction temperatures (300 ^oC to 400 ^oC) shows a general increase in magnetic properties, while further increasing the reduction temperatures (400 ^oC to 500 ^oC) decrease magnetic properties. Likely, at low temperatures, soft phase precursor is not fully converted to Fe_3O_4 soft phase, diluting magnetic properties. At high reduction temperatures, it is likely that too much SFO has decomposed, yielding a non-optimal hard/soft phase ratio for effective exchange-coupling. Improvements in M_r, M_s, and $(BH)_{max}$ of the SFO/Fe_3O_4 composite (reduced at 400 ^oC) compared to as-received SFO are 42 %, 29 % and 37 % respectively. A 37 % percent increase in energy product is a mark of success for this project.

Hysteresis loop of the SFO/Fe_3O_4 composite along with as receives SFO, shown in **Figure 3.1.2-9** displays single phase behavior, suggestive of an exchange-coupled composite[42]. Smooth transition from first to second quadrants in the hysteresis loop, as well as lack of kinks in the second quadrant is evidence of the hard and soft phases behaving as one.

Comparing FORC diagrams of SFO and SFO/Fe_3O_4 composite revels further evidence of exchange-coupling (**Figure 3.1.2-10**). The maximum value for the FORC distribution is 65×10^{-9} for the composite material and 19×10^{-9} for the SFO suggesting more ferromagnetic interactions[43], [53]. Larger spread of *Hu* data is further evidence of more particle interaction in the composite compared to as-received SFO[51]. A "hotspot" shift bellow the Hu=0 axis, as in the case of the composite, suggests an exchange-style particle interaction[43].

Recoil loop measurement in **Figure 3.1.2-11** show further evidence of exchange-coupling. Although closed recoil loops are typically expected for single-phase magnets, as-received SFO displays slightly open recoil loops. Typically, open recoil loops are attributed to decoupling in exchange-coupled nano-composite magnets[49]. However, in-homogeneities in magnetic anisotropy[71], thermal fluctuation[72] and intergranular exchange interactions[73] have been suggested to cause open recoil loops in single phase magnets, explaining SFO's open recoil loops. The relative openness of the recoil loops is investigated by normalized recoil loop area by ½ total hysteresis loop area and is shown in **Figure 3.1.2-11 (C)**. SFO/Fe_3O_4 composite and SFO show very similar normalized recoil

loop area behavior, suggesting no additional decoupling as a result of the added soft phase. This evidence is in agreement with the FORC analysis and the kink-less hysteresis loop.

Recoil remanence ratio, for the SFO/Fe_3O_4 composite and SFO is shown in **Figure 3.1.2-11 (D)**. M_{recoil}/M_r could give insight to the resistance of a PM to demagnetization. An exchange-coupled PM with optimized microstructure has a partially reversible demagnetization curve[10], suggesting M_{recoil}/M_r near 1 at low H_a. This is the case with the composite material. The SFO/Fe_3O_4 composite also demonstrates higher M_{recoil}/M_r than as-recieved SFO at the investigated H_a values, suggesting the composite has a higher degree of reversibility than the single phase hard phase. Combined, the evidence from the hysteresis loop, FORC diagrams and recoil loop measurements point to exchange-coupling, as the reason behind improvements in magnetic properties of the SFO/Fe_3O_4 composite compared so as received SFO

3.2 SFO/Co Material System

3.2.1 Procedure

A similar precipitation route as one described in **Section 3.1.1.1** was used to replace Fe based soft phase with Co based soft phase. Variations of 28.7, 57.4 and 114.8 mmol of $Co(NO_3)_2$ (Sigma Aldrich >98%) was mixed with variations of 167, 334 and 668 mmol of $CO(NH_2)_2$, Urea (Sigma Aldrich >99.5%) in 150mL of water. The mixture was then mixed into a slurry of 1.58 mmol of SFO and 50mL of H_2O at 90 ^oC over periods of 0.5, 1 and 2 hours. The resulting mixture was cooled quickly to prevent further particle growth. In order to understand the effect of the amount of Co on the surface of SFO, the amount of Co was

varied. The amount of precipitated Co was varied by changing the precipitation time as well as the initial SFO:Co mass precipitation ratio. Precipitation time was varied between 0.5 hr, 1 hr and 2hr for 1:1.98 SFO:Co ratio powder. The SFO:Co mass precipitation ratio was varied between 1:0.98, 1:1.96 and 1:3.92 for 1 hr precipitated powder.

In order to understand the soft phase precipitation process experiments without SFO, soft phase only, were investigated. 57.4 mmol of $Co(NO_3)2$ was mixed with 334 mmol of Urea and held at 90 ^oC for 2 hours. The resulting homogeneous precipitation creates nano-scale particles of the soft magnetic phase precursor.

In both the composite and soft phase cases, the resulting particles were centrifuged, washed with ultra-high pure water and centrifuged again. The powder and liquid was separated by decantation. The powder was dried at 80 ^oC in a vacuum furnace for 24 hours to ensure no moisture remains after which the dried agglomerates are broken by mortar and pestle. The powders were then treated in a tube furnace under forming gas (5% H_2, 95 % N_2) at temperatures ranging from 250 ^oC to 450 ^oC with 1 hour ramp and no hold time. The resulting powder was handled in Argon atmosphere to avoid oxidation.

The yield of Co-O precipitation was obtained by the gravimetric analysis based method. The collected liquid was dried and calcined at 800^oC for 6 h in air atmosphere. The residue remaining after calcination was Co_3O_4 single phase which was confirmed by X-ray diffraction analysis. The amount of Co_3O_4 was used to calculate yield of the precipitation process.

The same instruments and procedures as those described in Section 3.1.1 were used for phase, microstructure and magnetic characterization.

3.2.2 Results

3.2.2.1 Co Based Soft Phase

Like Fe-based soft phase, Co based soft phase was precipitated by homogeneous precipitation of urea. SEM Micrographs of the as precipitated Co based soft phase **(a)** and **(b)**, as well as Co based soft phase reduced at 400 ^{o}C **(c)** and **(d)** are displayed in **Figure 3.2.2-1**. As precipitated soft phase precursor was difficult to image due to charging, likely caused by low electrical conductivity of the powder. Collections of spike-like features >1 μm in length and <200 nm in width are observed. After the reduction the Co based soft phase's microstructure is an agglomeration of nano rods <500 nm in length and <100 nm in diameter.

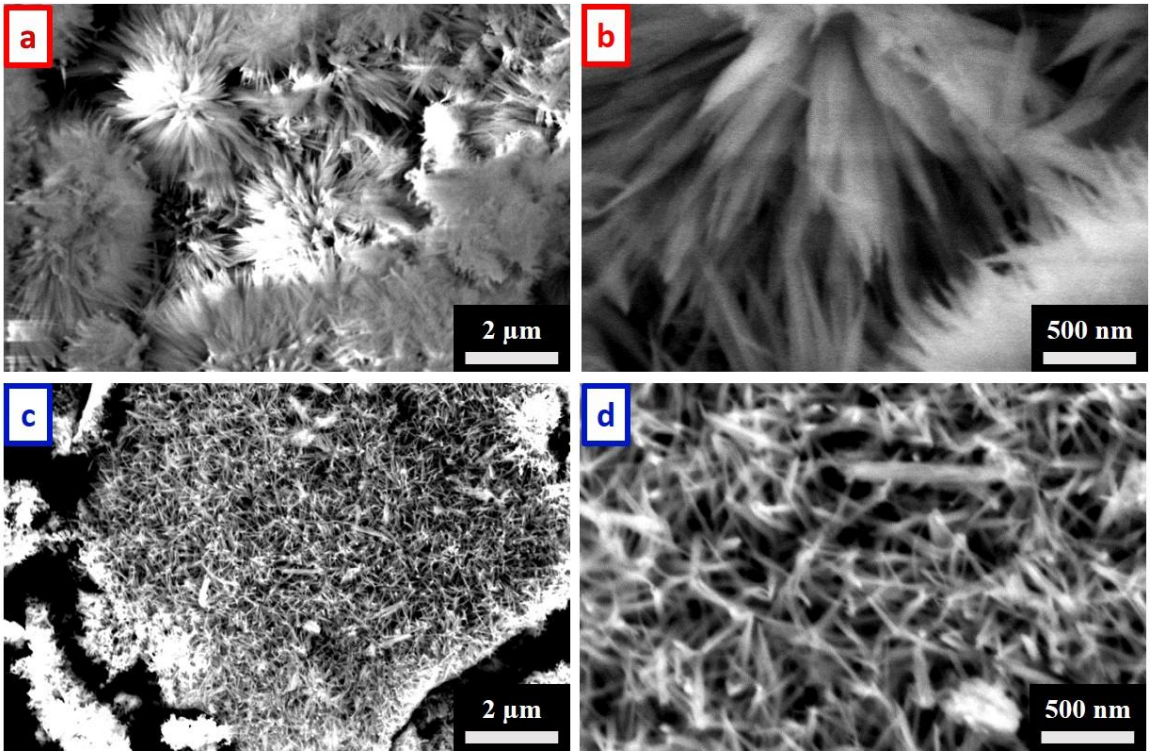

Figure 3.2.2-1(a), (b) SEM micrographs of homogeneously precipitated Co based soft phase precursor; (c), (d) SEM micrographs of soft phase reduced at 400 °C

XRD waterfall plots of as-precipitated as well as reduced (250-450 °C) Co based soft phase precursor and soft phase are shown in **Figure 3.2.2-2**. The as-precipitated precursor has high background intensity at low angles and displays peaks belonging to $Co(OH)_2$. Increasing reduction temperature causes loss of of $Co(OH)_2$ XRD peaks as well as gain of Co XRD peaks. Relatively broad Co XRD peaks are observed.

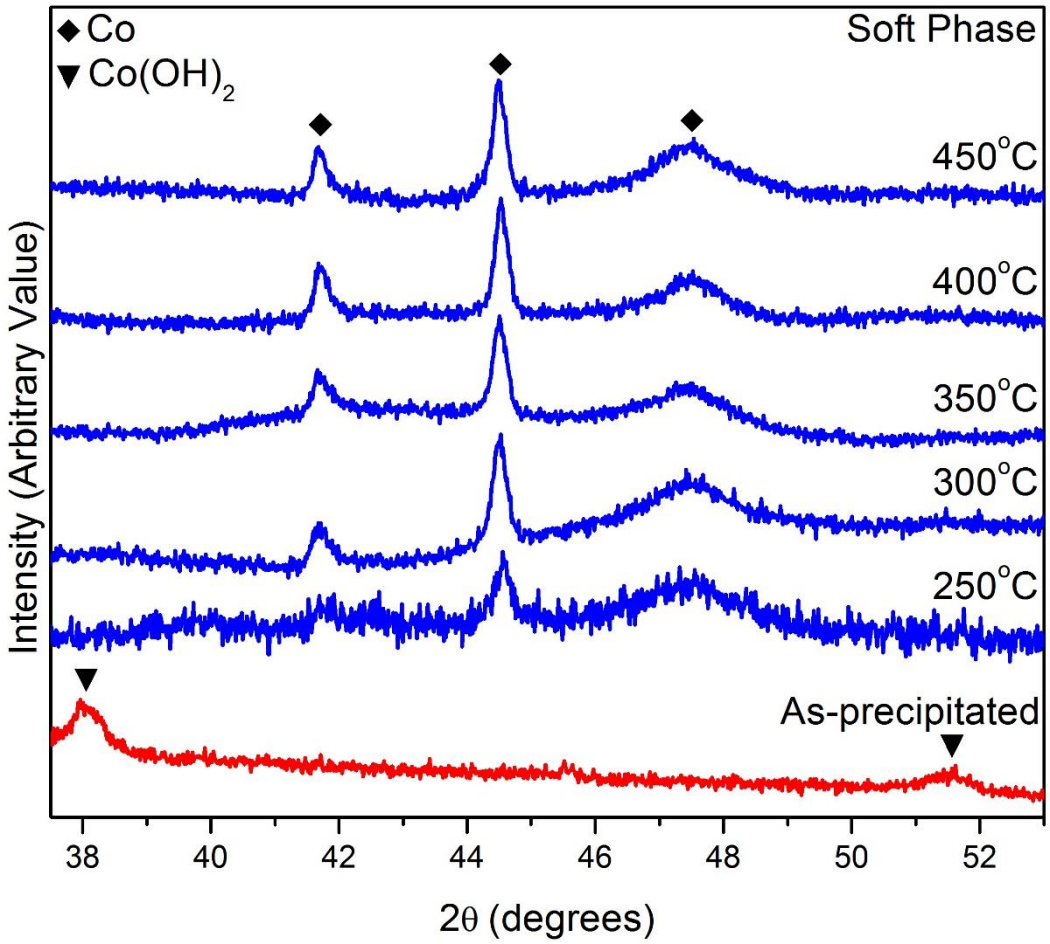

Figure 3.2.2-2 X-ray diffraction patterns for the Co based soft phase after precipitation as well as at reduction temperatures 300-450 °C.

XRD peak intensity ratio vs. reduction temperature of the Co based soft phase is shown in **Figure 3.2.2-3**. The XRD peak intensity ratios of $Co(OH)_2$ account for 100 % of the peak intensities before reduction, but completely disappear by reduction temperature of 250 °C. The XRD peak intensity ratio of Co makes up 100 % of the peak intensities at the reduction temperature of 250 °C and stays constant all the way through to reduction temperature of 450 °C.

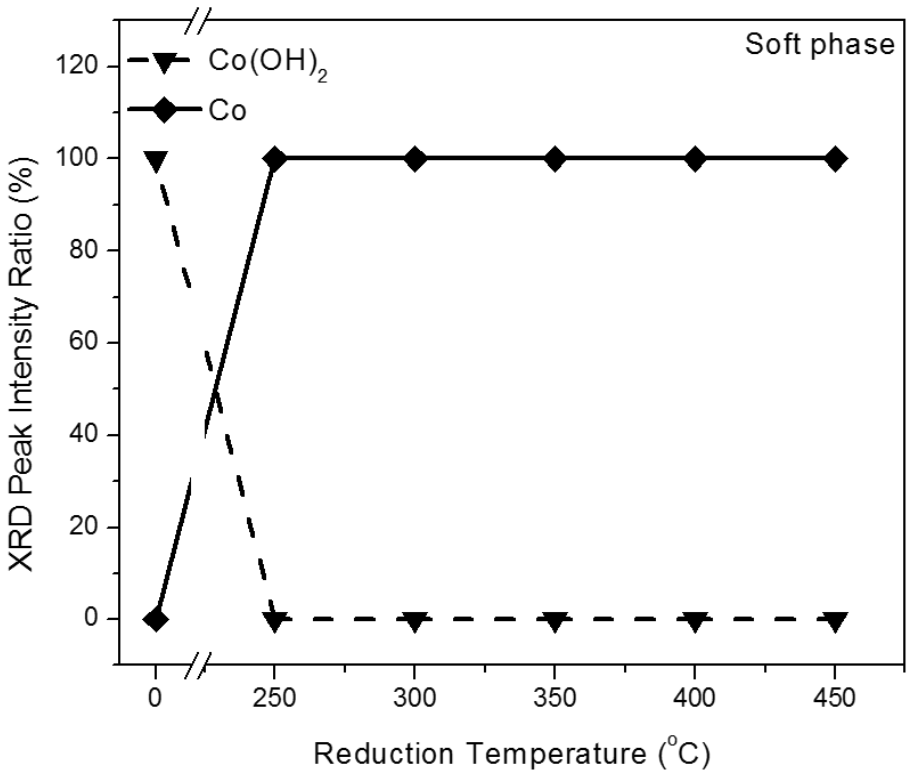

Figure 3.2.2-3 XRD peak intensities ratios of Co based soft phase at various reduction temperatures. The peak intensity ratio is the ratio of the most intense peak of a particular phase to the sum of the intensities of the most intense peaks of all identifiable phases. The most intense peaks for Co and $Co(OH)_2$ are from the (111) and (011) planes, respectively.

M_s of the soft phase particles post precipitation as well as at reduction temperatures of 300ºC and 400ºC is displayed in **Figure 3.2.2-4**. Post precipitation, (0 ºC), M_s is a mere 0.9 emu/g. M_s increases from 0.9 emu/g to 166 emu/g as the powder is reduced at 300 ºC. M_s stays constant at reduction temperatures 300 ºC and 450 ºC.

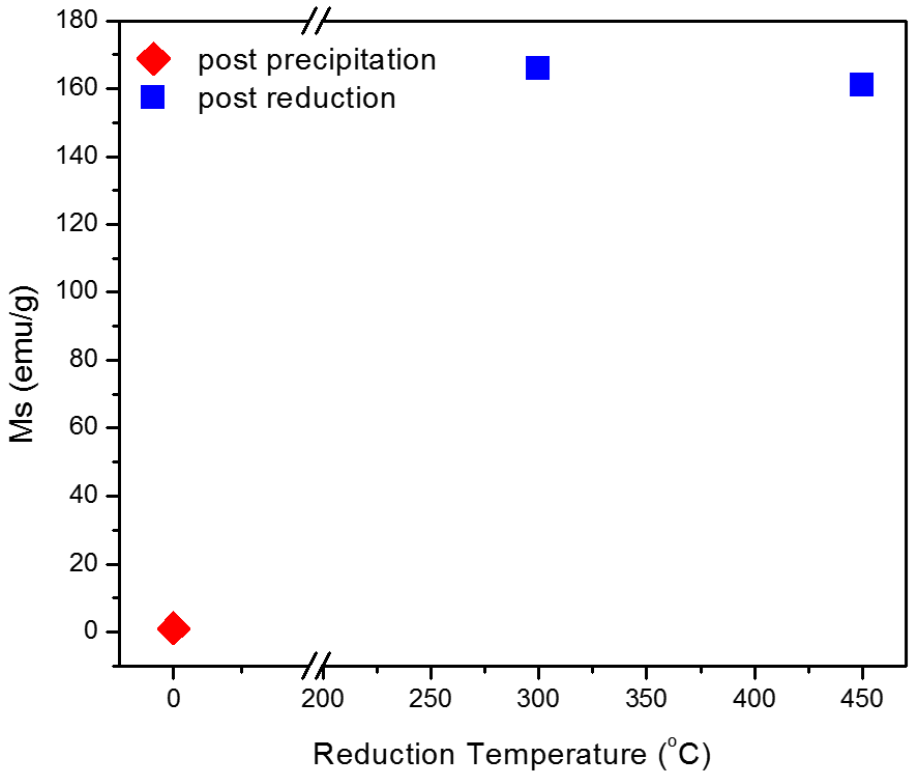

Figure 3.2.2-4 Saturation magnetization of the Co based soft phase post precipitation as well as at various reduction temperatures.

3.2.2.2 SFO/Co Based Composite

Co based soft phase was precipitated heterogeneously on the surface of SFO. The calculated yield of the precipitation process, based on the amount of Co was different depending on the initial ratio of Co:SFO:Urea used. SFO:Co:Urea mass ratios of 1 g SFO : 0.979 g Co : 10.028 g urea, 1 g SFO : 1.959 g Co : 20.056 g urea and 1 g SFO : 3.918 g Co : 40.111 g urea produced yields of 19.8 %, 21.8 % and 25.4 % respectively (under 1 hr precipitation conditions). SEM micrograph is the as received SFO **(a-c)**, SFO/Fe based

composite after precipitation **(d-f)** and SFO/Fe based composite after reduction **(g-i)** is shown in **Figure 3.2.2-5**. As received SFO powder is made up of hexagonal flakes with smooth, featureless surfaces. After precipitation, high aspect ratio features ~500 nm in length and <50 nm in width appear on the surface of SFO. After reduction, high aspect ratio features ~500 nm in length and ~100 nm in width are formed on the surface of SFO.

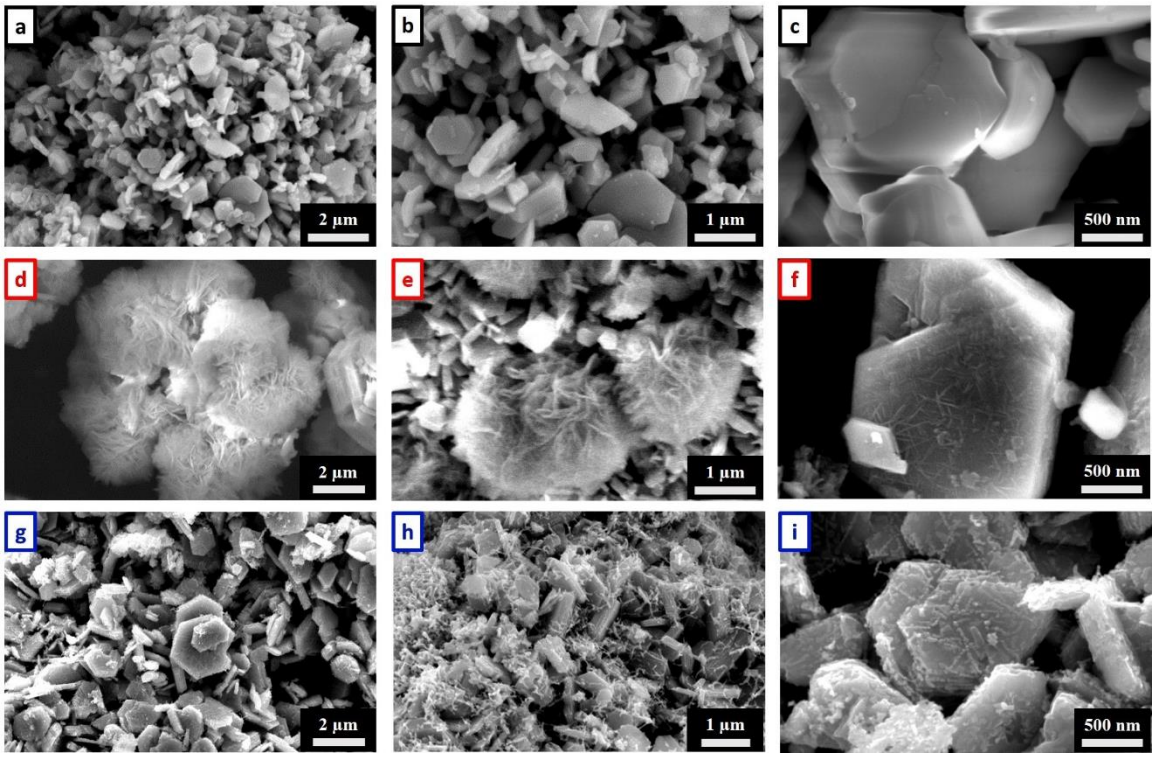

Figure 3.2.2-5(a), (b), (c): SEM micrographs of single phase SFO powder. (d), (e), (f): SEM micrographs of SFO/Co based composite powder after precipitation procedure. (g), (h), (i): SEM micrographs of SFO/Co based composite powder after reduction at 400 °C.

XRD waterfall plots of as-precipitated as well as reduced (at various temperatures) SFO/Co based composite are shown in **Figure 3.2.2-6**. The as-precipitated composite displays peaks belonging to CoO_2 and SFO. At the reduction temperature of 250 °C the composite shows XRD peaks belonging to CoO_2, Co and SFO. Increasing reduction

temperature causes the peaks of CoO_2 to disappear, however peaks of (Fe,Co) appear. Even higher reduction temperature causes the intensity of SFO peaks to decrease and the intensity of (Fe,Co) peaks to increase.

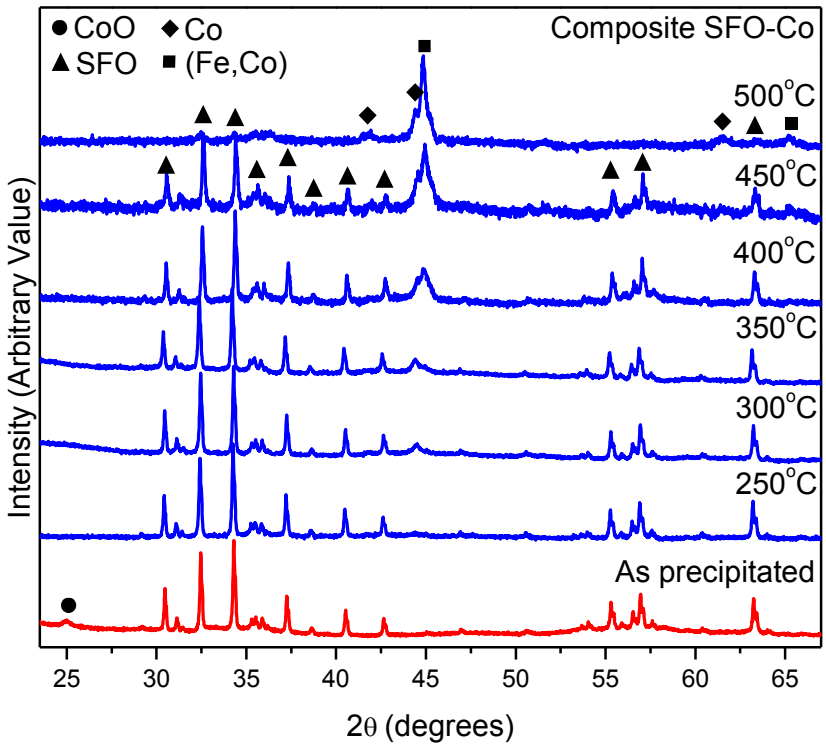

Figure 3.2.2-6 X-ray diffraction patterns for the SFO/Co based composite after precipitation procedure as well as at reduction temperatures 250-500 °C.

XRD peak intensity ratio vs. reduction temperature of the SFO/Fe based composite is shown in **Figure 3.2.2-7**. The XRD peak intensity ratios of CoO_2 and SFO account for 100% of the peak intensities before reduction. The XRD peak intensity ratio of CoO_2 deceases as the composite is reduced at 250 °C and disappears completely as the reduction temperature is increased to 300 °C. SFO peak intensity ratio decreases as the reduction

temperature increases from 250 ºC to 500 ºC. Peak intensity ratio of Co becomes non-zero at the reduction temperature of 250 ºC and increases as the reduction temperature is increased to 500 ºC. (Fe,Co) peak intensity ratio first appears at 300 ºC and grows, surpassing SFO's peak intensity ratio at the reduction temperature of 500 ºC.

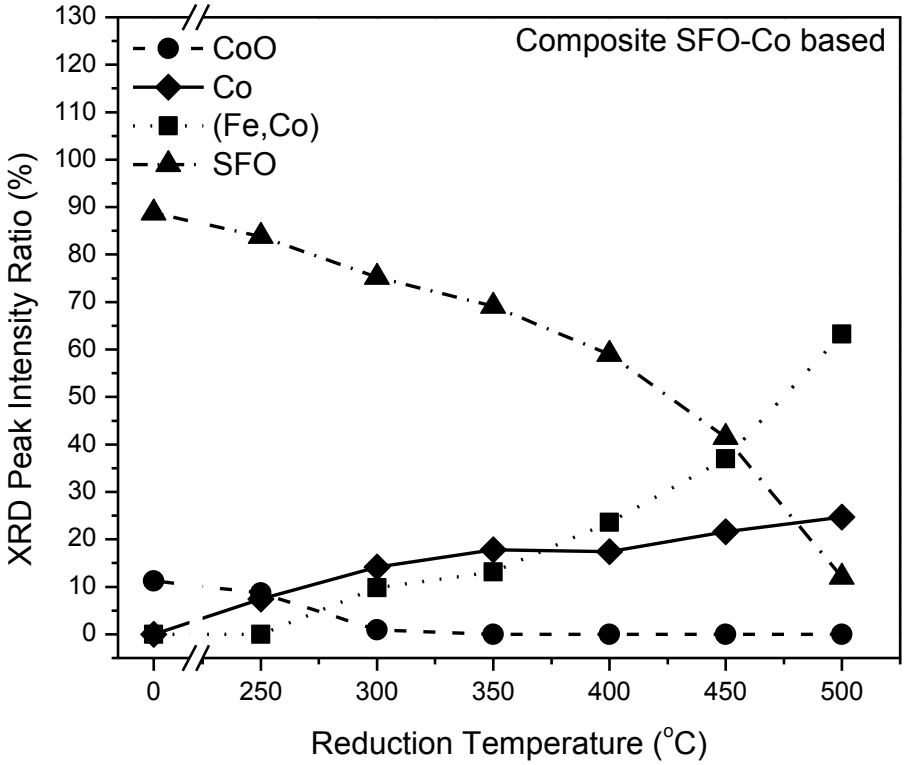

Figure 3.2.2-7 XRD peak intensities ratios of SFO/Co based composite at varying reduction temperatures. The peak intensity ratio is the ratio of the most intense peak of a particular phase to the sum of the intensities of the most intense peaks of all identifiable phases. The most intense peaks for CoO, Co, (Fe,Co) and SFO are from the (004), (111), (110) and (107) planes, respectively.

Properties of the SFO/Co based system compared to the SFO/Fe based system are shown in **Figure 3.2.2-8**. They hysteresis curve shows the SFO/Co based composite

reduced at 350 ^{o}C, composed of SFO/Co,(Fe,Co) and SFO/Fe based composite, composed of SFO/Fe_3O_4, also reduced at 350^{o}C. Magnetization of the SFO/Co,(Fe,Co) composite is higher than that of the SFO/Fe_3O_4 composite at 16,000 Oe, and 0 Oe. It takes a higher negative *H* to reduce the magnetization of the saturated SFO/Co,(Fe,Co) composite to 0 emu/g in comparison to the SFO/Fe_3O_4 composite. The magnetization of the SFO/Co,(Fe,Co) composite is higher than that of the SFO/Fe_3O_4 composite at every point in the second quadrant.

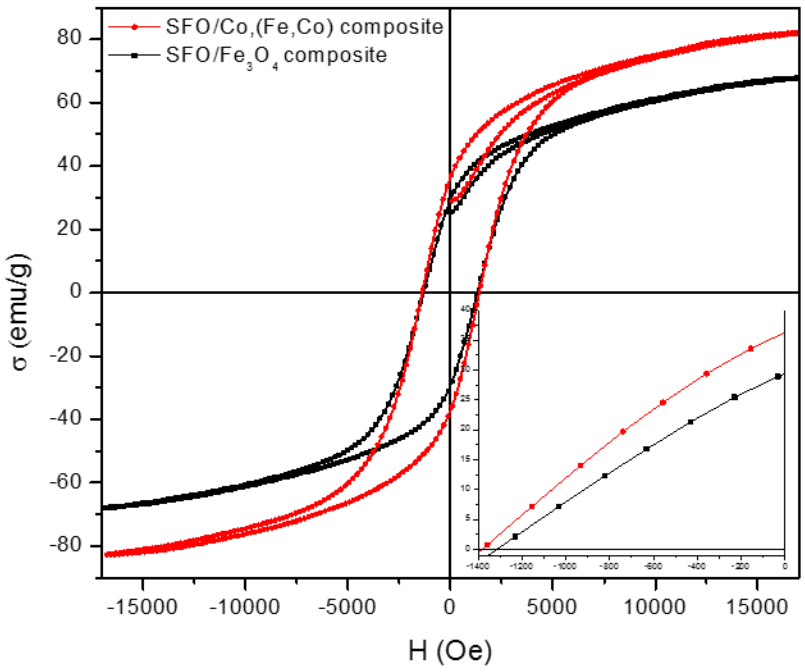

Figure 3.2.2-8 Comparison of hysteresis loop of SFO/Fe based and SFO/Co based composites.

Further differences between SFO, SFO/Fe based and SFO/Co based composites can be seen in the FORC diagrams of **Figure 3.2.2-9**. While all diagrams show single "hot spot", there are clear differences between them. There is a higher spread in H_u for the SFO/Fe based composite **(b)** in comparison to SFO **(a)**. There is an even larger H_u distribution for the SFO/Co composite **(c)**. The magnitude of ρ is highest in the SFO/Co based composite, followed by the SFO/Fe based composite and lastly single phase SFO.

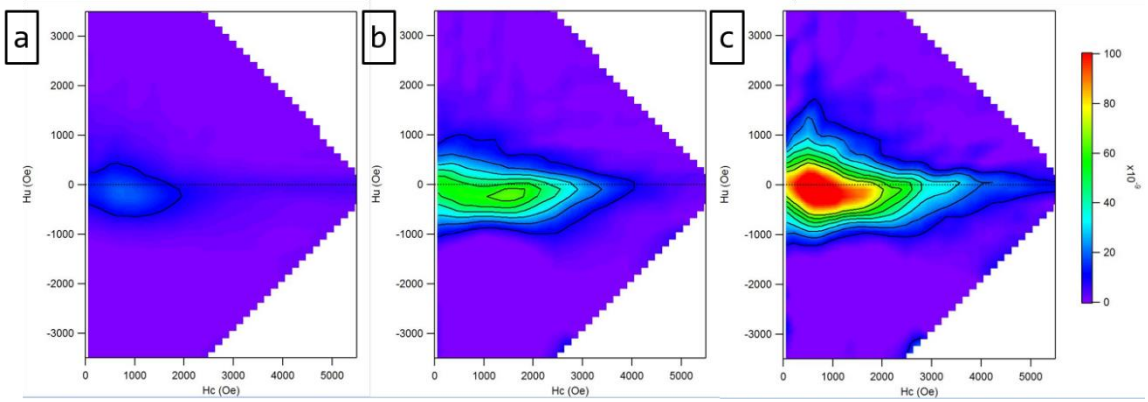

Figure 3.2.2-9 First order reversal curve (FORC) diagrams for (a) single phase SFO, (b) SFO/Fe_3O_4 composite (reduced at 400 °C) and (c) SFO/Co,(Fe,Co) composite (reduced at 350 °C)

Figure 3.2.2-10 shows the effect of precipitation time and reduction temperature on the energy product of the SFO/Co based composite. The energy product of the 0.5 hr powder increases as the reduction temperature is increased from 300 °C to 350 °C and stays fairly constant as the reduction temperature is increased further to 400 °C. The energy product of the 1 hr powder increases as the reduction temperature is increased from 300 °C to 350 °C and decreased as the reduction temperature is increased further to 400 °C. The

energy product of the 2 hr powder stays fairly constant throughout the investigated reduction temperatures. 1 hr powder has the highest achieved BHmax.

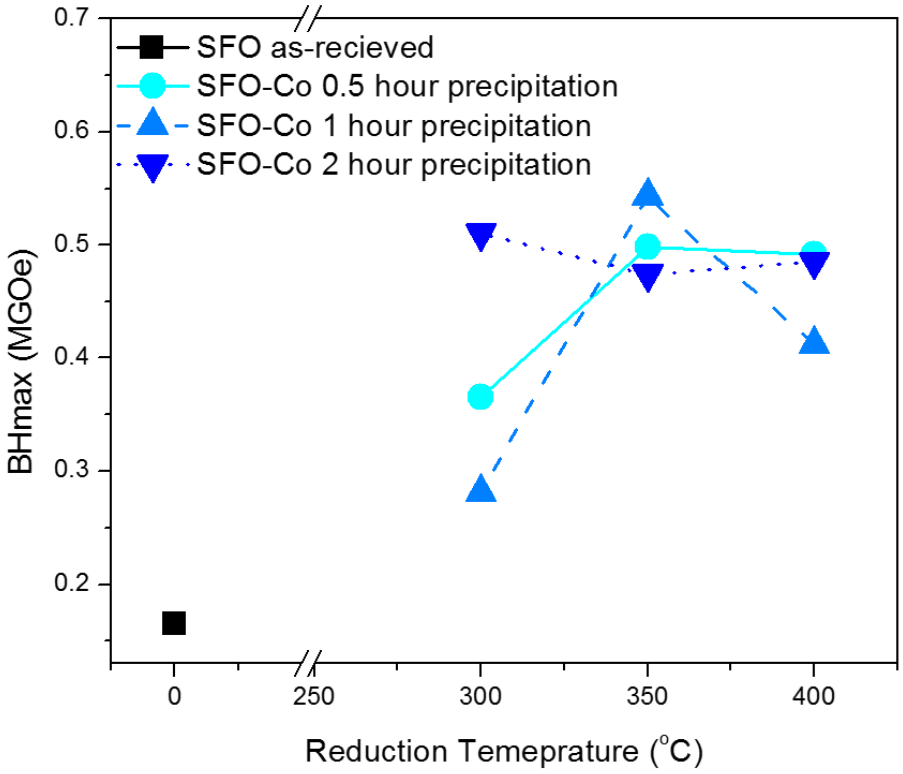

Figure 3.2.2-10 Effect of precipitation time and reduction temperature on the BHmax of the SFO/Co based composite powder.

Figure 3.2.2-11 shows the effect of precipitation time and reduction temperature on M_s of SFO/Co based composite. M_s of the 0.5 hr powder stays constant as the reduction temperature is increased from 300 °C to 350 °C to 400 °C. M_s of the 1 hr powder increases as the reduction temperature is increased from 300 °C to 350 °C and stays fairly constant as the reduction temperature is increased further to 400 °C. M_s of the 2 hr powder stays

constant as the reduction temperature is increased from 300 - 350 ºC followed by a major increase in M_s as the temperature is increased further to 400 ºC. The M_s of the 2 hr power is higher than that of the 1 hr and the 0.5 hr powders at all reduction temperatures. The M_s of the 1hr powder is higher than that of the 0.5 hr powder at the reduction temperatures of 350 ºC and 400 ºC.

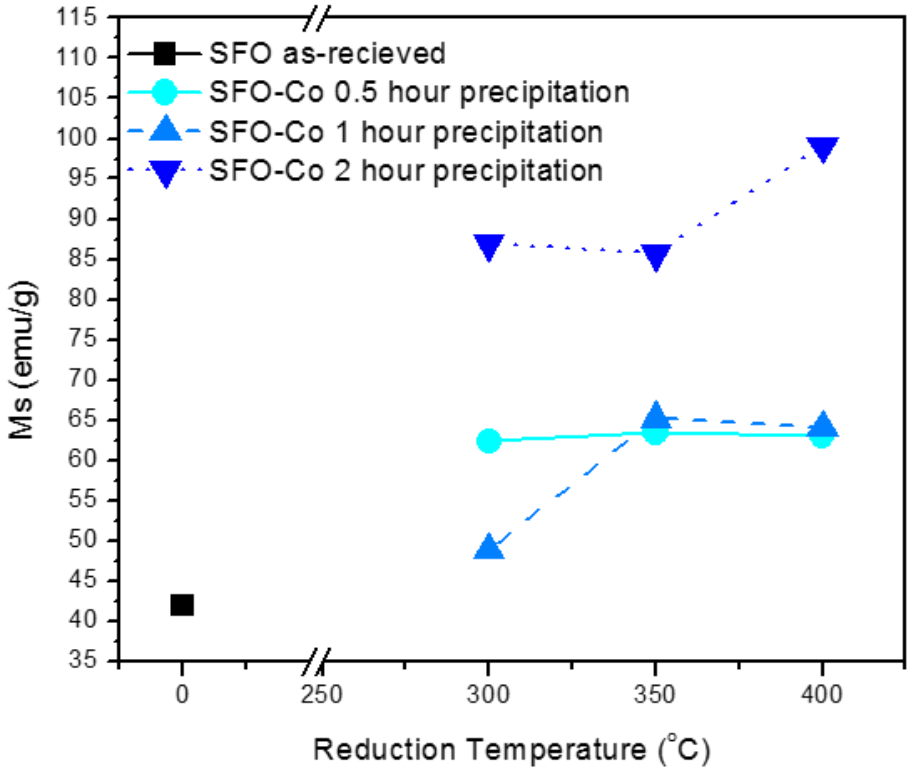

Figure 3.2.2-11 Effect of precipitation time and reduction temperature on the M_s of the SFO/Co based composite powder.

Figure 3.2.2-12 shows the effect of precipitation time and reduction temperature on M_r of SFO/Co based composite. M_r of the 0.5 hr powder increases as the reduction temperature is increased from 300 ºC to 350 ºC and slightly decreases as the reduction

temperature is increased to 400 ^{o}C. M_r of the 1 hr powder increases as the reduction temperature is increased from 300 ^{o}C to 350 ^{o}C and decreases as the reduction temperature is increased further to 400 ^{o}C. M_r of the 2 hr powder decreases slightly as the reduction temperature is increased from 300 – 350 ^{o}C followed by an increase in M_r as the temperature is increased further to 400 ^{o}C. The 2 hr powder displays the highest M_r at the investigated reduction temperatures. The M_r of both the 1hr and the 0.5 hr powders is highest at the reduction temperature of 350 ^{o}C.

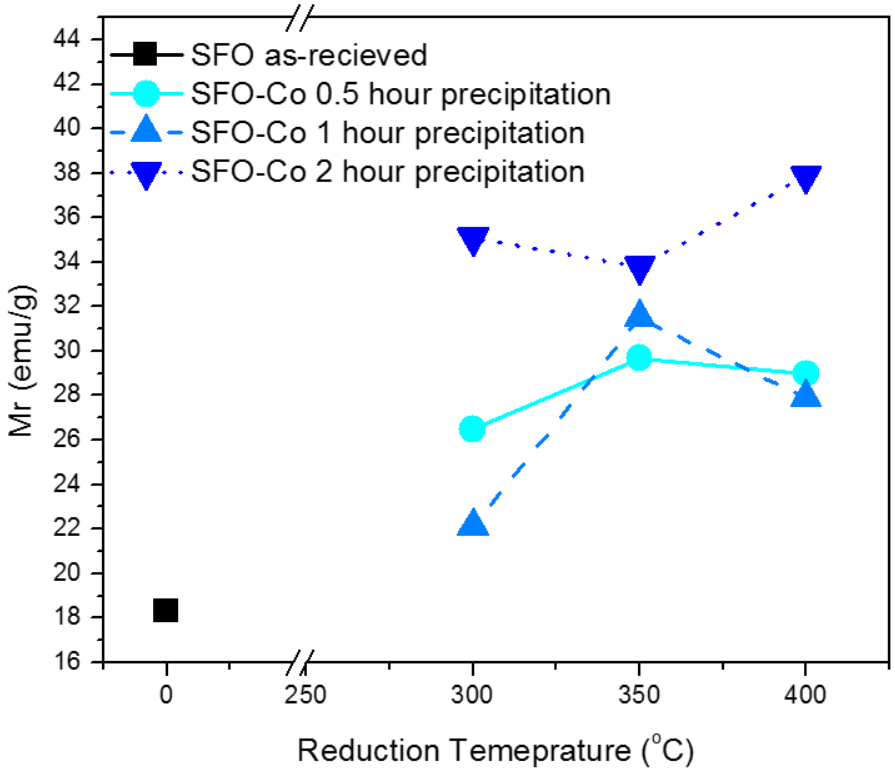

Figure 3.2.2-12 Effect of precipitation time and reduction temperature on the M_r of the SFO/Co based composite powder.

Figure 3.2.2-13 shows the effect of precipitation time and reduction temperature on H_c of SFO/Co based composite. H_c of the 0.5 hr powder increases as the reduction temperature is increased from 300 ^oC to 350 ^oC and stays constant as the reduction temperature is increased to 400 ^oC. H_c of the 1 hr powder increases as the reduction temperature is increased from 300 ^oC to 350 ^oC and decreases as the reduction temperature is increased further to 400 ^oC. H_c of the 2 hr powder stays fairly constant as the reduction temperature is increased from 300 to 350 ^oC to 400 ^oC. The 2 hr powder displays the lowest H_c at the investigated reduction temperatures. M_r of the 1 hr powder is highest of all the time investigated powders, at the temperature of 350 ^oC.

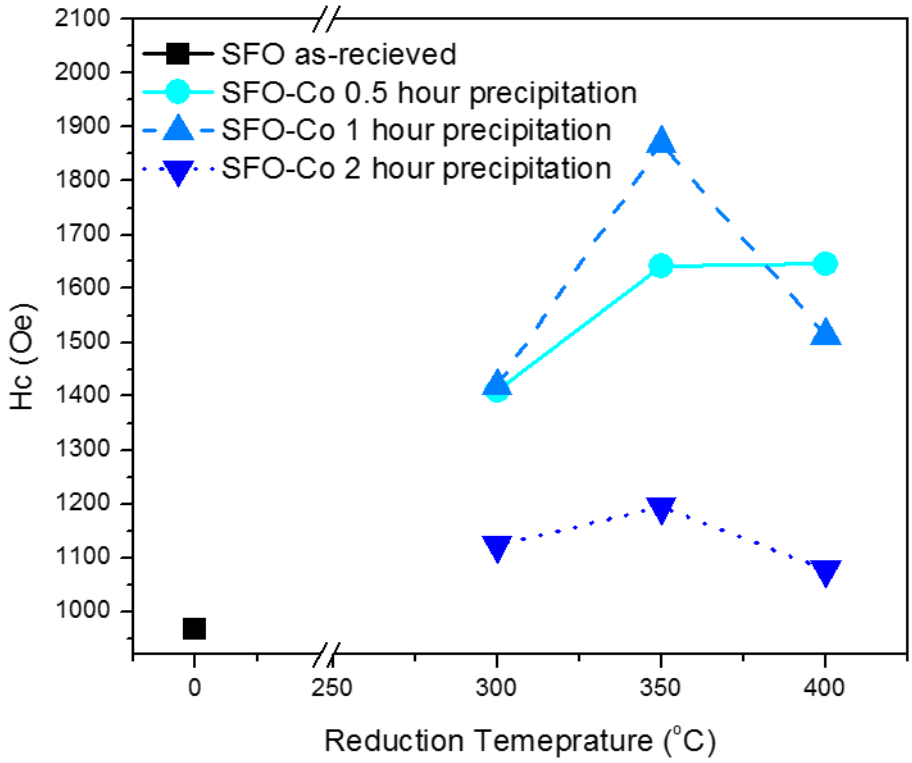

Figure 3.2.2-13 Effect of precipitation time and reduction temperature on the H_c of the SFO/Co based composite powder.

Figure 3.2.2-14 shows the effect of starting SFO:Co precipitation ratio and reduction temperature on energy product of SFO/Co based composite powder. Energy product of the 1:0.98 powder increases as the reduction temperature is increased from 300 ^{o}C to 350 ^{o}C and decreases as the reduction temperature is increased further to 400 ^{o}C. Energy product of the 1:1.98 powder follows a similar patter with an increase as the reduction temperature is increased from 300 ^{o}C to 350 ^{o}C and decreases as the reduction temperature is increased to 400 ^{o}C. Energy product of the 1:3.92 powder decreases slightly as the reduction temperature is increased 300 ^{o}C to 350 ^{o}C to 400 ^{o}C. The highest BH_{max} was achieved using 1:1.96 SFO:Co ratio, reduced at 350 ^{o}C.

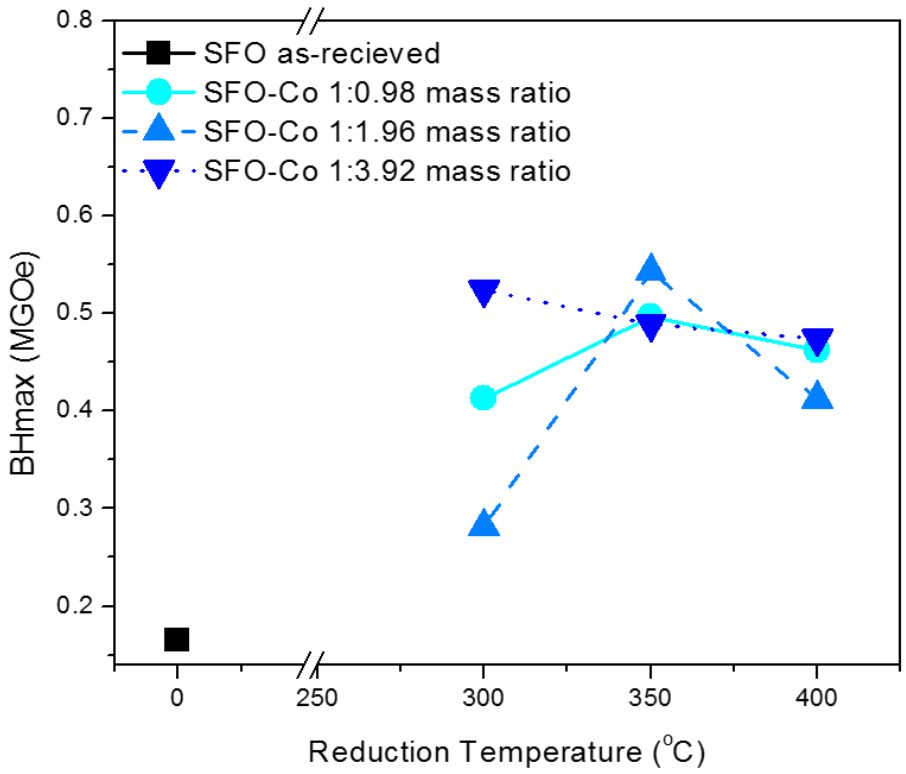

Figure 3.2.2-14 Effect of the starting SFO:Co precipitation ratio and reduction temperature on the BHmax of the SFO/Co based composite powder.

Figure 3.2.2-15 shows the effect of starting SFO:Co precipitation ratio and reduction temperature on M_s of SFO/Co based composite powder. M_s of the 1:0.98 powder increases as the reduction temperature is increased. M_s of the 1:1.98 powder increase as the reduction temperature is increased from 300 °C to 350 °C and decreases slightly as the reduction temperature is increased further to 400 °C. M_s of the 1:3.92 powder decreases slightly as the reduction temperature is increased 300 °C to 350 °C and increases greatly as the reduction temperature is taken to 400 °C. The 1:3.92 powder

displays the highest M_s.

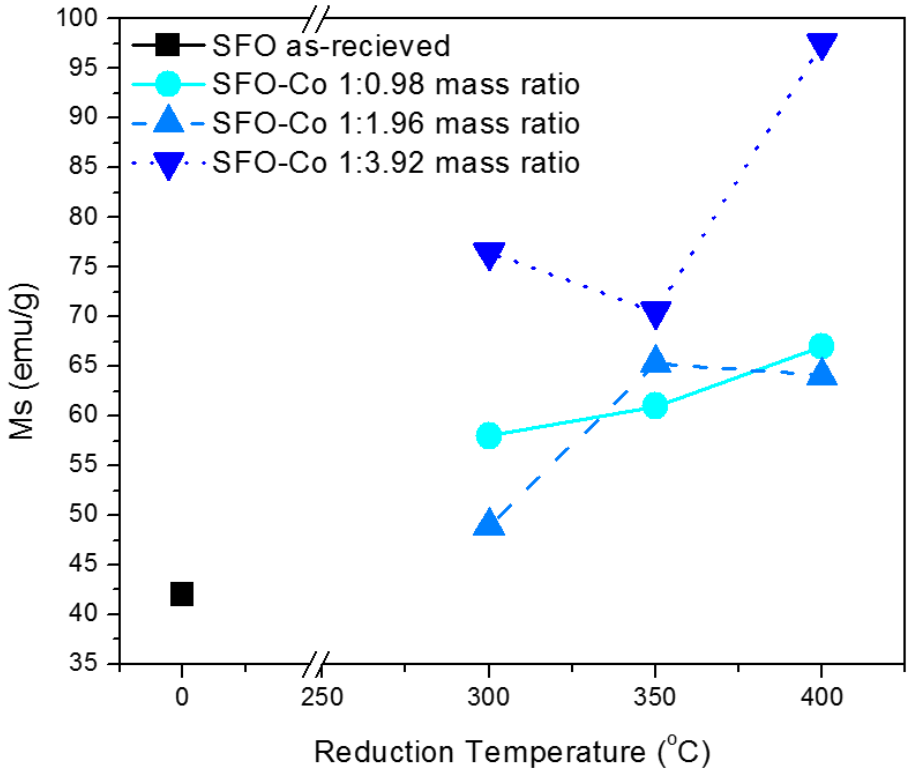

Figure 3.2.2-15 Effect of the starting SFO:Co precipitation ratio and reduction temperature on the M_s of the SFO/Co based composite powder.

Figure 3.2.2-16 shows the effect of starting SFO:Co precipitation ratio and reduction temperature on H_c of SFO/Co based composite powder. H_c of the powders from investigates SFO:Co initial precipitation mass ratios behaves similarly, with an intial incrase as the reduction temperature is increased from 300 °C to 350 °C, followed by a subsequent decrease as the reduction temperature is increased from 350 °C to 400 °C. The 1:0.98 powder shows the highest H_c, while the 1:3.92 powder shows the lowest H_c.

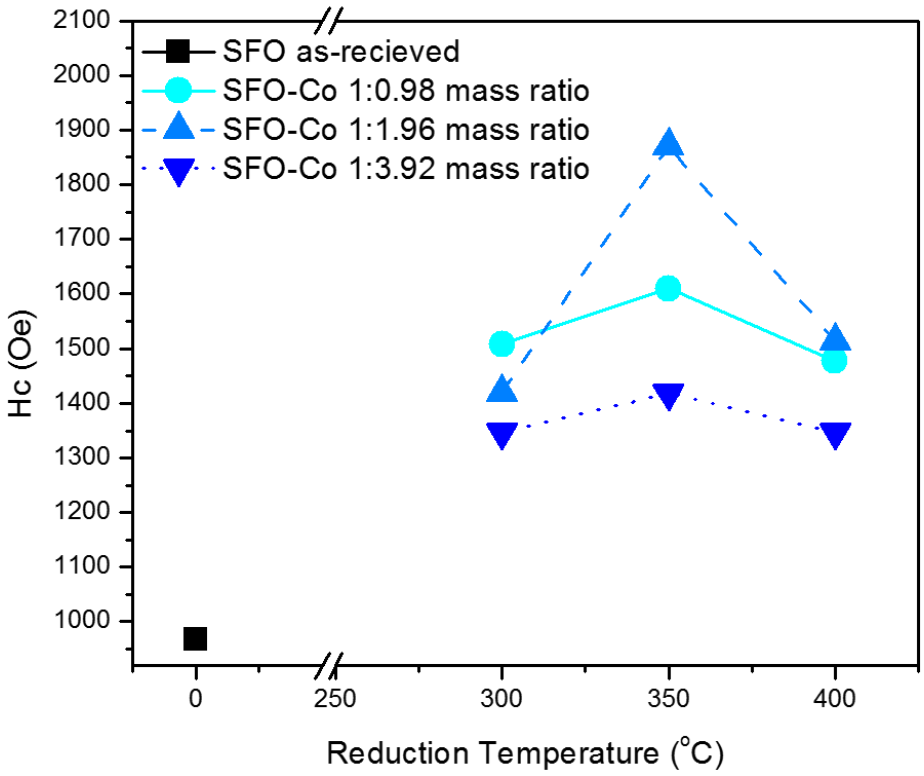

Figure 3.2.2-16 Effect of the starting SFO:Co precipitation ratio and reduction temperature on the H_c of the SFO/Co based composite powder.

Figure 3.2.2-17 shows the effect of starting SFO:Co precipitation ratio and reduction temperature on M_r of SFO/Co based composite powder. M_r of the 1:0.98 powder increases slightly as the reduction temperature is increased from 300 ºC - 400 ºC. M_r of the 1:1.98 powder increase as the reduction temperature is increased from 300 ºC - 350 ºC and decreases as the reduction temperature is increased further to 400 ºC. M_r of the 1:3.92 powder decreases slightly as the reduction temperature is increased 300 ºC - 350 ºC to 400 ºC.

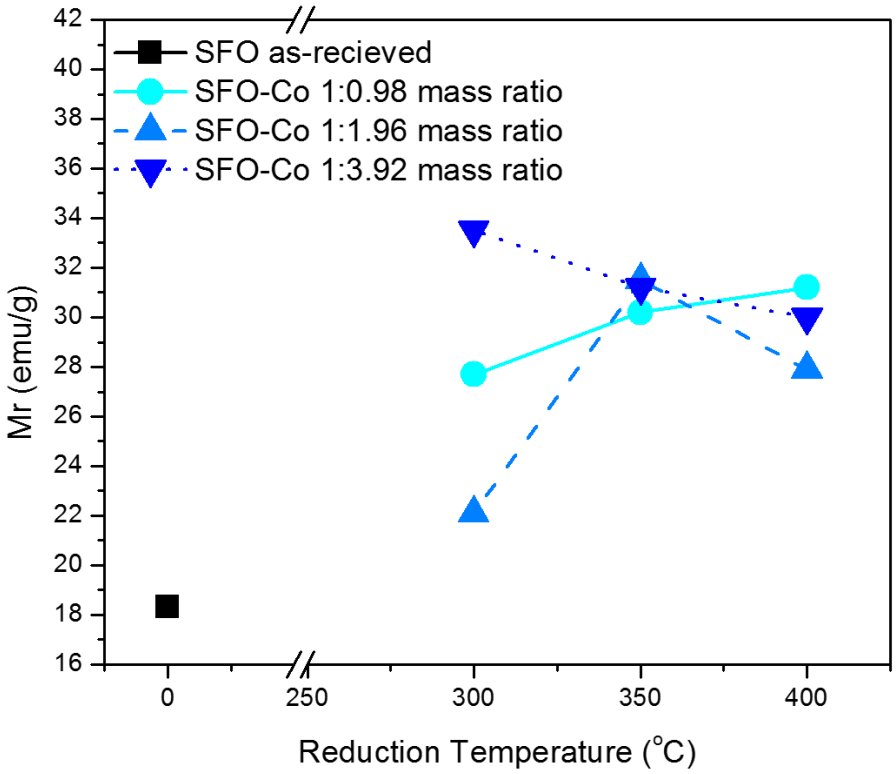

Figure 3.2.2-17 Effect of the starting SFO:Co precipitation ratio and reduction temperature on the M_r of the SFO/Co based composite powder.

Figure 3.2.2-18 shows the effect of starting Co and urea concentration on the energy product of the SFO/Co based composite. Powder synthesized with higher Co and urea concentration has higher energy product. Energy product for 0.1661 M Co^{2+}, 1.6696M urea increases as reduction temperature is increased from 300 ºC to 350 ºC. Energy product for 0.3322 M Co^{2+}, 3.3393 M urea decreases slightly as reduction temperature is increased from 300 ºC to 350 ºC.

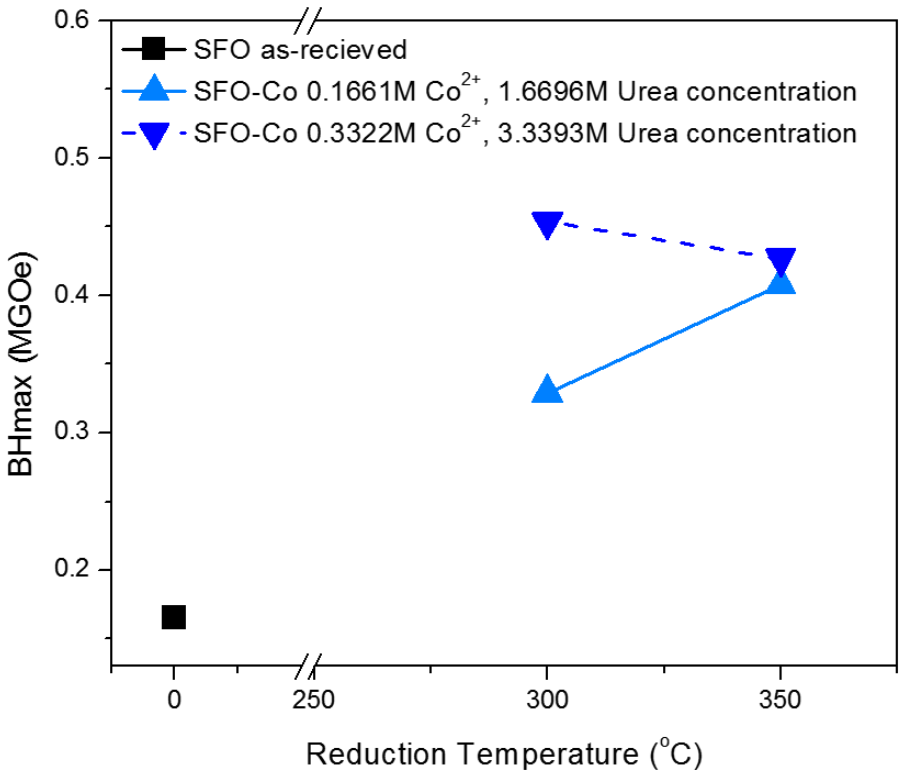

Figure 3.2.2-18 Effect of the starting Co and urea precipitation concentration and reduction temperature on the energy product of the SFO/Co based composite powder.

Figure 3.2.2-19 shows the effect of starting Co and urea concentration on the M_s of the SFO/Co based composite. Powder synthesized with higher Co and urea concentration has higher M_s. M_s for both investigated concentrations increases as reduction temperature is increased from 300 ºC to 350 ºC.

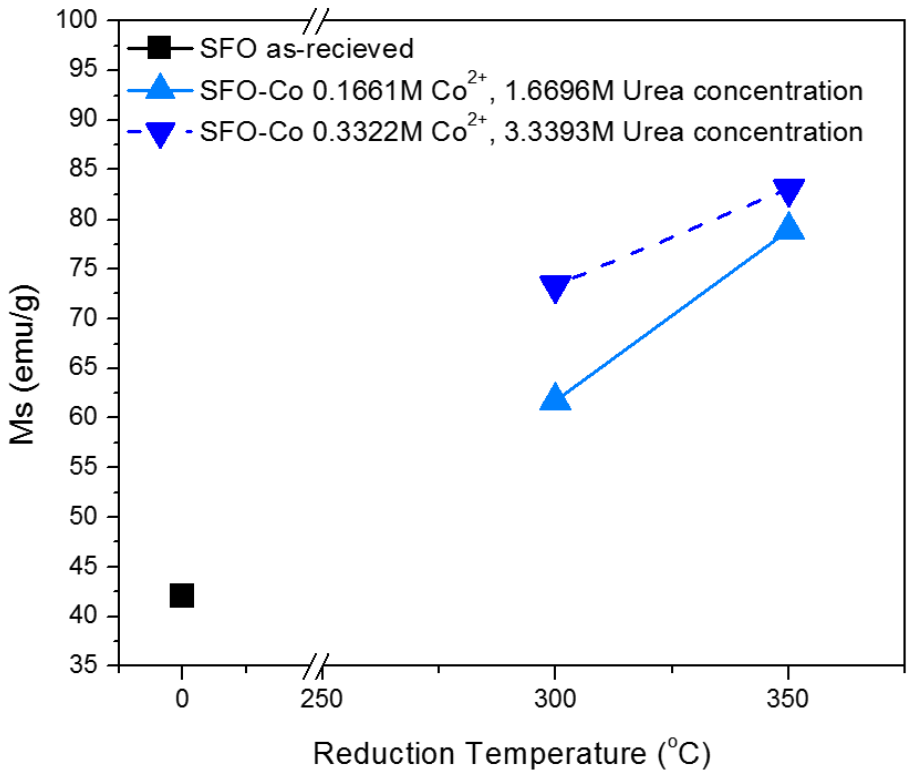

Figure 3.2.2-19 Effect of the starting Co and urea precipitation concentration and reduction temperature on M_s of the SFO/Co based composite powder.

Figure 3.2.2-20 shows the effect of starting Co and urea concentration on the H_c of the SFO/Co based composite. Both Co and urea concentrations show similar H_c at the perspective investigated reduction temperatures. H_c for both investigated concentrations decreases as reduction temperature is increased from 300 ºC to 350 ºC.

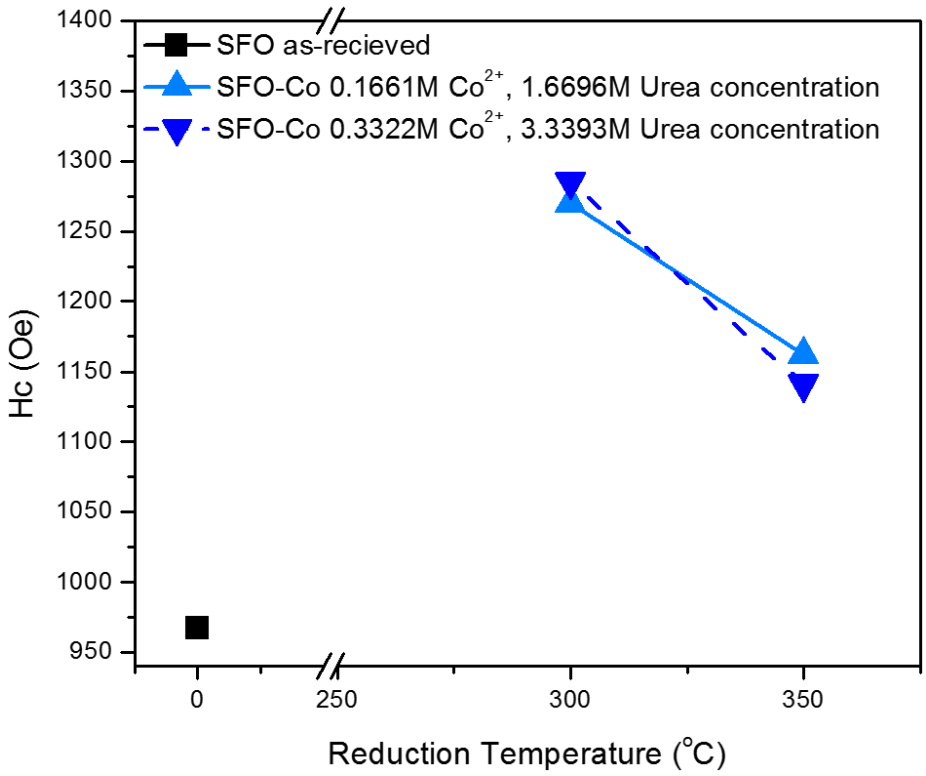

Figure 3.2.2-20 Effect of the starting Co and urea precipitation concentration and reduction temperature on H_c of the SFO/Co based composite powder.

Figure 3.2.2-21 shows the effect of starting Co and urea concentration on the M_r of the SFO/Co based composite. Powder synthesized with higher Co and urea concentration has higher M_r. M_r for both investigated concentrations increases as reduction temperature is increased from 300 ºC to 350 ºC.

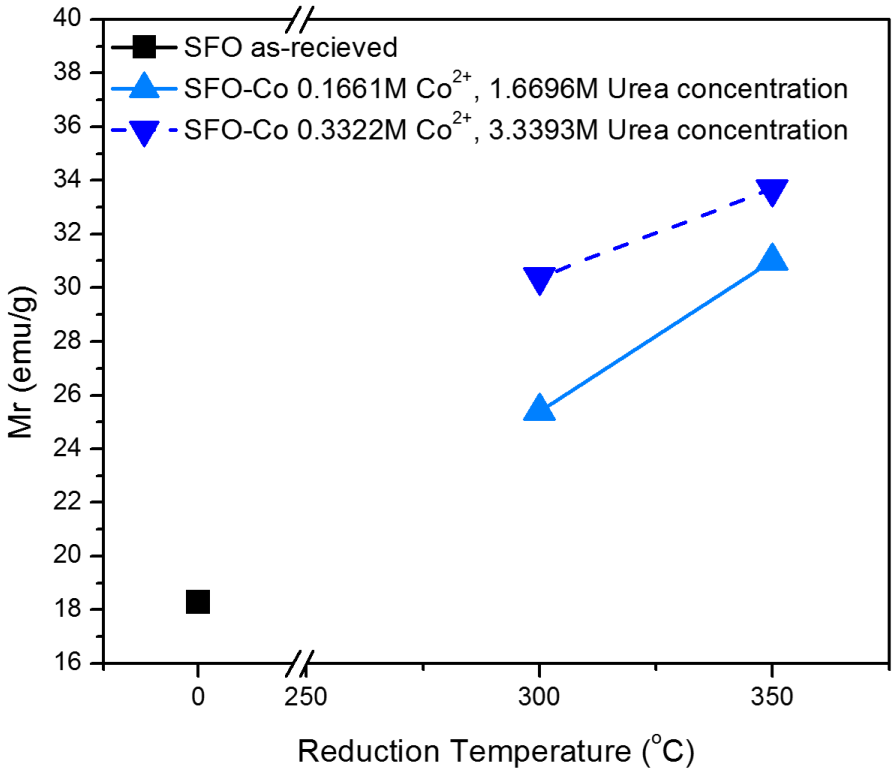

Figure 3.2.2-21 Effect of the starting Co and urea precipitation concentration and reduction temperature on M_r of the SFO/Co based composite powder.

3.2.3 Discussion

3.2.3.1 Co Based Soft Phase

Similar to the Fe based system (**Section 3.3.1**), characterization of the soft Co phase was undertaken first. **Figure 3.2.2-1** displays micrographs of precipitated Co base soft phase precursor and soft phase particles. As-precipitated, flower-like, rod resembling particles, **Figure 3.2.2-1 (a), (b)**, have high aspect ratio, and are vastly different from the Fe base soft phase precursor particles in **Figure 3.1.2-1 (a), (b)**. Like the Fe based material,

the Co based precipitated material is also in the nano-scale. Soft phase precursor particles reduced at 400 ^{o}C, **Figure 3.2.2-1 (c), (d)**, form nano-rods, and exhibit a high degree of agglomeration, but stay in the nano-range, important for taking full advantage of exchange-coupling.

Like the Fe base soft phase precursor, the as precipitated Co based soft phase precursor particles exhibit low degree of crystallinity, having the high XRD background intensity at low angles and wide XRD peaks, seen in **Figure 3.2.2-2 (As-precipitated)**. Besides the amorphous material, the as precipitated Co precursor powder consists of $Co(OH)_2$. As the powder is reduced at 250 ^{o}C, the amorphous and $Co(OH)_2$ materials disappear and broad Co peaks appear (**Figure 3.2.2-2 (250 ^{o}C)**). Increasing reduction temperature causes the reduction of Co^{2+} of $Co(OH)_2$ into metal Co. Metal is formed at much lower reduction temperatures using the Co based soft phase, in comparison to the Fe based soft phase. This holds promise of a wider processing window to achieve an oxide/metal nano-composite for the SFO/Co system compared to SFO/Fe system.

Figure 3.2.2-3 shows the evolution of peak intensities of the Co based soft phase. At reduction temperature of 250 ^{o}C and higher, Co metal is formed. This result is in agreement with the measured M_s at various reduction temperatures (**Figure 3.2.2-4**). The M_s of the soft phase material reduced above 300 ^{o}C is >160 emu/g, reaching the theoretical M_s for Co [55]. In comparison, Fe based soft phase had M_s of only 93 emu/g after reduction at 300 ^{o}C.

3.2.3.2 SFO/Co Based Composite

The soft phase Co was deposited heterogeneously onto SFO. Smooth, featureless surface of SFO's faceted flakes (**Figure 3.2.2-5 (a), (b) and (c)**) became covered in nano-scale rod-like features after precipitation procedure (**Figure 3.2.2-5 (d), (e) and (f)**). Similar to the SFO/Fe based system, after reduction at 400 ^{o}C, the SFO appears undamaged (**Figure 3.2.2-5 (g), (h)**). However, higher magnification, (**Figure 3.2.2-5 (i)**), displays necking and grain growth behavior of the deposited nano-rods.

The yield of the precipitation varied according to the initial SFO:Co mass precipitation ratio. Assuming perfect coverage and that all soft phase transformed to Co, thicknesses from 4 nm (for 1:0.98 SFO:Co ratio) to 20 nm (for 1:3.92 SFO:Co ratio) of Co would envelope SFO (see **Sample Soft Phase Thickness Calculation** in **Appendix**). As discussed in **Section 2.3.1**, the ideal soft phase thickness is ~10.5 nm. Ideally, under assumption of perfect coverage and no reaction, initial mass precipitation ratio of SFO:Co should be 1:2.23 which is very close to the investigated ratio of 1:1.98. The calculated thicknesses in tens of nanometers if perfect coverage is assumes are consistent with visible observations of the SFO/Co based composite micrographs.

The as-precipitated SFO/Co based composite displays XRD patterns of SFO and a small peak of CoO_2, suggesting insignificant damage to SFO due to the precipitation process (**Figure 3.1.2-6 As-precipitated**). As the composite is reduced 300 ^{o}C, CoO_2 disappears, while Co and (Fe,Co), a solid solution of Fe and Co is created.

The evolution of the phases, through peak intensities is more easily appreciated in **Figure 3.2.2-7**. SFO peak intensity ratio decreases while peak intensity ratios of Co and

(Fe,Co) increase with increasing reduction temperature. More Co precursor is reduced with higher reduction temperature, attributing to the increase in Co content. Increase in (Fe,Co) peak suggests reaction in which the precipitated Co based material acts as a reducing agent of SFO (SFO does not reduce at these reduction temperatures without a catalyst). The Fe for the (Fe,Co) solid solution is supplied by the SFO, consistent with the decomposition of SFO as seen by lower SFO XRD peak intensity ratio at elevated reduction temperatures. As seen in **Figure 3.2.3-1**, the phase diagram of Fe - Co system, a solid solution of the BCC structure (Fe side), as well of the FCC structure (Co side) is present for a wide range of Fe/Co compositions. As the reduction temperature increases, the peak intensity ratio of (Fe,Co) (in BCC crystal structure) surpasses that of Co/(Fe,Co) (in FCC crystal structure). This suggests the composition moves closer to the more Fe rich BCC solid solution in the two phase solid solution region of the phase diagram. Likely, the interface between the soft Co/(Fe,Co) phase and hard SFO phase is large in surface area to allow the transport of Fe atoms. Interfaces with large surface area are ideal for exchange-coupling. At reduction temperatures above 450^{o}C, BCC (Fe,Co) become the primary phase (assumed form XRD peak intensity ratios). Likely, the ratio of hard phase to soft phase is too low to lead to improved properties at these temperatures. In this case, there is likely too much soft phase for efficient coupling with the hard phase. On the other hand, at reduction temperatures of 300 ^{o}C to 400 ^{o}C, SFO is the only detectable oxide phase (no reaction between SFO and Co to an oxide). At those reduction temperatures SFO also has higher XRD peak intensity ratio than the metal phase(s), giving high hope for optimal microstructure and hard/soft ratio.

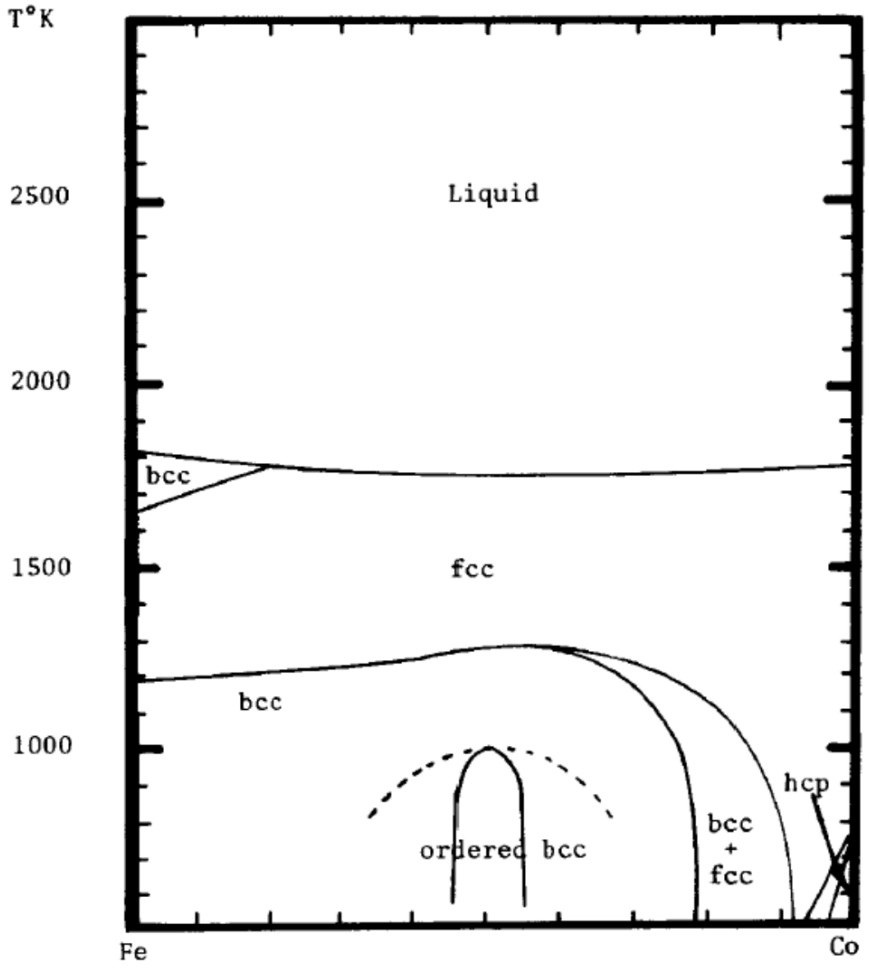

Figure 3.2.3-1 Co Fe phase diagram. From REF [74]

As discussed earlier (**Section 3.1.3**) SFO/Fe based composite powder had better magnetic properties than single phase SFO by exhibiting a higher energy product. Interestingly, SFO/Co based composite has even better properties than the SFO/Fe based composite, judging by the hysteresis loop of **Figure 3.2.2-8**. With higher magnetization at every *H* in the second quadrant, the energy product of the SFO/Co based system is clearly higher than that of SFO/ Fe_3O_4based system. The higher M_s of Co in comparison to Fe_3O_4 (soft phase of SFO/Fe based system), is evident as the SFO/Co composite displays a higher

M_s in comparison to the SFO/ Fe_3O_4 based composite. The higher H_c in the SFO/Co based composite compared to SFO/ Fe_3O_4 based composite is attributed to better coupling and/or less degree of reaction between the hard and soft phases. Like the SFO/ Fe_3O_4 based composite, the SFO/Co based composite displays a smooth second quadrant hysteresis curve (no kink) indicating exchange-coupling.

Comparing FORC diagrams of SFO, SFO/Fe_3O_4 and SFO/Co,(Fe,Co) composites provides evidence of greater exchange-coupling in the SFO/Co based system (**Figure 3.2.2-9**). Features of the FORC diagram have already been discussed in **Section 3.1.3.2** and **Section 2.2.2.4**. The SFO/Co based composite has a larger spread of H_u data and higher intensity "hotspot" than the exchange-coupled SFO/Fe based composite. Like single phase SFO and SFO/Fe based composite, single "hotspot" behavior is observed in SFO/Co based composite, suggesting single phase exchange type composite behavior.

While the improvements over the oxide/oxide SFO/Fe_3O_4 system make the oxide/metal SFO/Co,(Fe,Co) system a great success, further optimization was investigated. Optimal synthesis conditions were explored by varying the amount of deposited soft phase. Modifying the soft phase was done by changing the length of time the precipitation procedure was allowed to run, and by varying the initial mass precipitation ratio of SFO:Co. Longer precipitation time, as well as higher starting Co content were hypothesized to increase the amount of precipitated soft phase.

The effect of precipitation time was investigated first. The figure of merit, energy product was maximized through a 1hr precipitation procedure with a reduction temperature of 350^{o}C (**Figure 3.2.2-10**). 1hr precipitation time henceforth was chosen as the ideal

precipitation time for the study. Notably, while increasing the reduction temperature from 300°C to 350°C gave mixed results with improvements for the 0.5 and 1hr samples, increasing the reduction temperature further to 400°C had an overall negative effect on the energy product. Using reduction temperature of 400°C was therefor abandoned later in the project.

Investigating *Ms*, *Hc* and *Mr* under various precipitation time conditions give insight to property-microstructure relationship of the SFO/Co based composite. **Figure 3.2.2-11** demonstrates that the 2hr precipitated composite, reduced at 400°C has the highest M_s. Higher precipitation time is hypothesized to precipitate more soft phase precursor, while higher reduction temperature transforms all the precursor (and possibly some hard phase) into soft phase, and increases the amount of soft phase in the composite. Highest M_s (compared to other powders) of the 2hr precipitated, 400°C reduced material is in agreement with the hypothesized ideas. Further evidence is provided through the fact that on average, M_s increases with precipitation time as well as with reduction temperature, consistent with M_s being representative of the amount of soft phase in the composite.

Figure 3.2.2-12, the effect of precipitation time and reduction temperature on the M_r of the SFO/Co based composite powder, has very similar trends to **Figure 3.2.2-10**, the effect of precipitation time and reduction temperature on the energy product of the SFO/Co based composite powder. It is not surprising that trends in Mr will follow trends in energy product. The exchange-coupling was discovered through observing improvements in *Mr* and allocating the reasoning for the improvements to phase interaction[25]. Every data point from the tested composites is higher than that of single phase SFO, in agreement with

Coehoorn's observations. The highest Mr is observed in 2 hr precipitation powder, suggesting the highest amount of exchange-coupled soft phase. This is attributed to the higher amount of soft phase of the 2hr precipitation. Lowest *Mr*, at reduction temperatures of 350°C and 400°C is that of 0.5 hour powder, in agreement with it having the least amount of exchange-coupled material, due to low amount of soft phase deposited within the 0.5 hour precipitation.

Large amount of decoupled soft phase should heavily influence H_c. Decoupled soft phase's moments will flip in the direction of the applied field easily, working to demagnetize the material, and also diluting and decreasing its H_c. Experimental results follow theory with the 2hr powder, having the lowest H_c values (**Figure 3.2.2-13**). Although having a lot of soft phase deposited on SFO allowed the 2hr powder to have the highest M_s and M_r, it has also robbed it of high H_c, suggesting lots of decoupled soft phase material. The highest H_c is found in 1hr precipitation composite powder. It is likely that the amount of soft phase is just right in this composite; and that the soft phase is well intermixed, and mostly coupled.

The effect of controlling the amount of soft phase through initial SFO:Co mass ratio was investigated as well. The highest energy product was observed in 1:1.96 ratio powder (**Figure 3.2.2-14**). Notably, the ratio required for the ideal exchange length of 10.5 nm is 1:2.23, and is very close to 1:1.96. Looking at M_s, H_c and M_r gives further evidence in agreement with the hypothesis of higher SFO:Co starting ratio depositing more soft phase in the composite. The highest M_s values are found for the highest SFO:Co ratio of 1:3.92 (**Figure 3.2.2-15**). The highest M_s corresponds to the reduction temperature of 400°C,

consistent with XRD peak intensities suggesting increase in soft phase volume fraction at elevated reduction temperatures (**Figure 3.2.2-7**).

Lowest H_c is once again found in the composite hypothesized to have the highest amount of soft phase. 1:3.92 composite is likely to have the highest amount of decoupled soft phase, due to its large soft phase volume fraction. The highest H_c coming from 1:1.96 powder is attributed to high amount of coupled soft phase in comparison to the other concentrations.

Similar results to investigating precipitation time effect were found in this SFO:Co ratio study. M_r and energy product trends are very similar. In **Figure 3.2.2-17**, 1:3.92 powder displays the highest M_r at low reduction temperature, likely attributed to having the highest amount of coupled soft phase, but loses Mr at elevated temperatures, suggesting a too low of a hard/soft phase ratio. 1:0.98 powder displays the lowest Mr at low reduction temperature (due to too high of a hard/soft ratio), but improves to displaying the highest M_r at 400^{o}C likely due to the powder approaching a more optimal hard/soft ratio. 1:1.96 ratio powder has mixed results, but has the highest M_r occurs at middle reduction temperatures, where its optimal hard/soft ratio likes resides.

It is likely that changing the concentration, not just amount of initial Co and urea will effect precipitation mechanics. Figure **3.2.2-18** shows that high precipitation reactant concentration composite powder has much improved energy product, especially at reduction temperature of 300 ^{o}C. Looking at M_s, H_c and M_r is likely to give reasoning behind improved properties of high concentration powder. Fist, M_s of the high precipitation concentration powder is higher, suggesting that more soft phase is deposited compared to

low precipitation concentration powder. H_c of the two powders are similar. Since the high concentration powder is likely to have more soft phase, due to its' higher M_s, similar H_c values to the low precipitation concentration powder suggests that the soft phase is better intermixed under high concentration precipitation conditions. This is in agreement with M_r, which is significantly higher for the high precipitation concentration powder suggesting more exchange-coupled soft phase in the high concentration precipitation powder.

4 Exchange-Coupled Nano-Composite Bulk Magnets

4.1.1 Procedure

The precipitated and reduced powder composites based on the SFO/Co system were densified. For comparison, a hand mixed composite was also synthesized. For the hand mixed composite, from homogeneously precipitated $Co(OH)_2$ was reduced at 400 ^oC, making phase pure Co. SFO and Co powder was hand mixed by mortar and pestle tumbled together in an attempt to achieve homogenous mixing. The hand mixed composite was mixed with an SFO:Co mass ratio of 1:0.427 in an attempt to match the total Co amount of the hand-mixed composite powder and the core-shell composite powder based on the precipitation synthesis of 1hr, 1:1.96 initial SFO:Co mass precipitation ratio.

Bulk samples of SFO/Co based composite were synthesized using CAPAD. Section 2.5.1 has more insight on CAPAD processing. 3/8 inch mini system was used to process at relatively high pressures of 505MPa. A typical experiment included a load ramp at constant voltage of 1.5V though which the pressure was ramped form 0 to 505MPa. Temperature

typically reached 200 ºC at the end of the pressure ramp. The temperature was then ramped using constant voltage ramp intervals of 0.25V every 20 seconds or every 5 seconds for high heating rate experiments. No hold time was used and the system voltage was lowered to 0V as soon as target temperature was reached (typically 300-500 ºC). Mechanical load was held while the die cooled to 200 ºC to increase the cooling rate. Density of bulk samples was measured through geometric means. Mass was measured and regular cylindrical geometry of the sample was in volume calculation. Density was calculated by dividing measured mass by calculated volume.

The same instruments and procedures as those described in Section 3.1.1 were used for phase, microstructure and magnetic characterization.

4.1.2 Results

To validate the necessity of nano-scale intermixing of two phases, that was achieved by precipitation of one phase on another, a hand mixed composite, based on SFO/Co system was densified. Figure **Figure 4.1.2-1** shows the hysteresis loop of the hand-mixed composite in comparison to the as received SFO powder, both densified at same processing conditions of 500 ºC, 505 MPa with no hold at temperature. The hand-mixed composite bulk sample has higher magnetization at 16,000 Oe, compared to as received densified SFO. However, in the second quadrant, the magnetization of the SFO sample is higher than that of the hand-mixed composite.

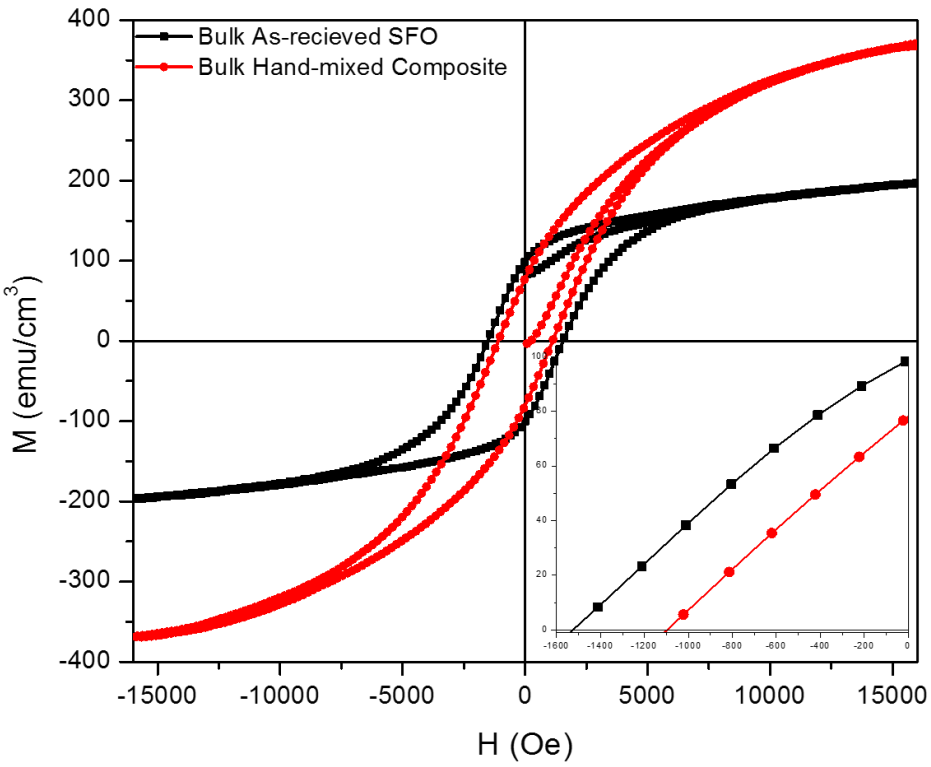

Figure 4.1.2-1 Hysteresis loop of as received SFO and hand-mixed composite, both densified using same processing conditions of 400°C, 505MPa and no hold at temperature.

Composition of bulk densified core-shell composite samples based on SFO/Co was investigated at temperatures of 350 °C, 400 °C to 500 °C. **Figure 4.1.2-2** shows XRD waterfall plots of reduced SFO/Co based powder (reduced at 350°C) as well as densified (at various temperatures) SFO/Co based bulk composite samples. The reduced composite powder displays peaks belonging to Co, (Fe,Co) and SFO. At the densification temperature of 300 °C the XRD peaks belonging to the soft phase (Co and Fe,Co) increase and various peaks belonging to SFO change in intensity. Increasing densification temperature to 500

^{o}C causes the peaks of SFO to decrease greatly and peaks of the $CoFe_2O_4$ phase to appear. At 500^{o}C, the peak belonging to Co is the 100% peak.

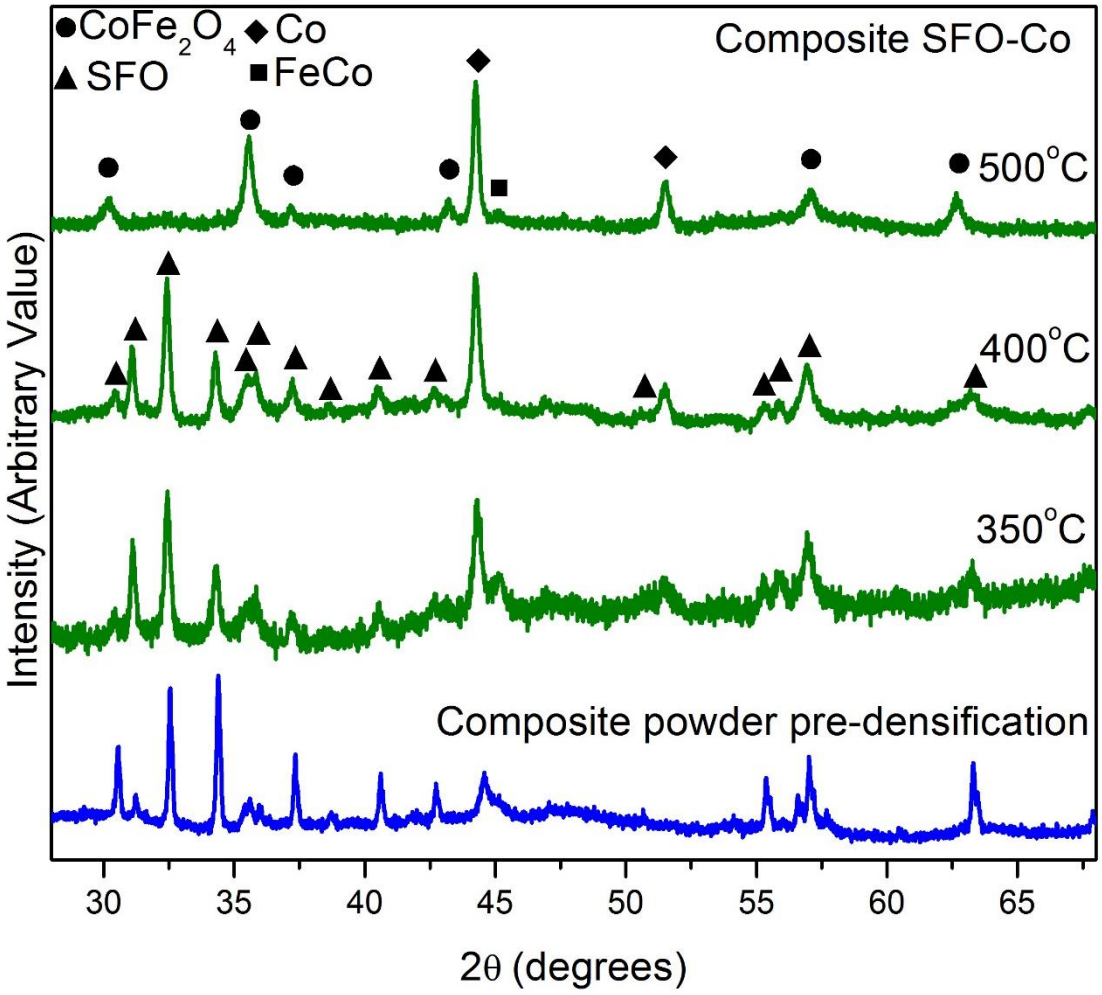

Figure 4.1.2-2 XRD plots of bulk SFO/Co based composites densified at 350^{o}C, 400^{o}C and 500^{o}C as well as SFO/Co based composite powder (1hr, 1:1.96 powder reduced at 350^{o}C).

XRD peak intensity ratio vs. densification temperature (0 ^{o}C being the composite powder reduced at 350 ^{o}C) of the SFO/Co based densified composite is shown in **Figure 4.1.2-3**. The XRD peak intensity ratios of Co, (Fe,Co) and SFO account for 100% of the

peak intensities before densification. The XRD peak intensity ratio of SFO deceases as the composite densified at 350 ^{o}C. Peak intensity ratio of Co increases as the powder is densified and as densification temperature is increases from 350 ^{o}C to 500 ^{o}C, surpassing SFO's peak intensity ratio at densification temperature of 400 ^{o}C. (Fe,Co) peak intensity ratio first increases as the powder is densified at 350 ^{o}C and decreases as the densification temperature is increased.

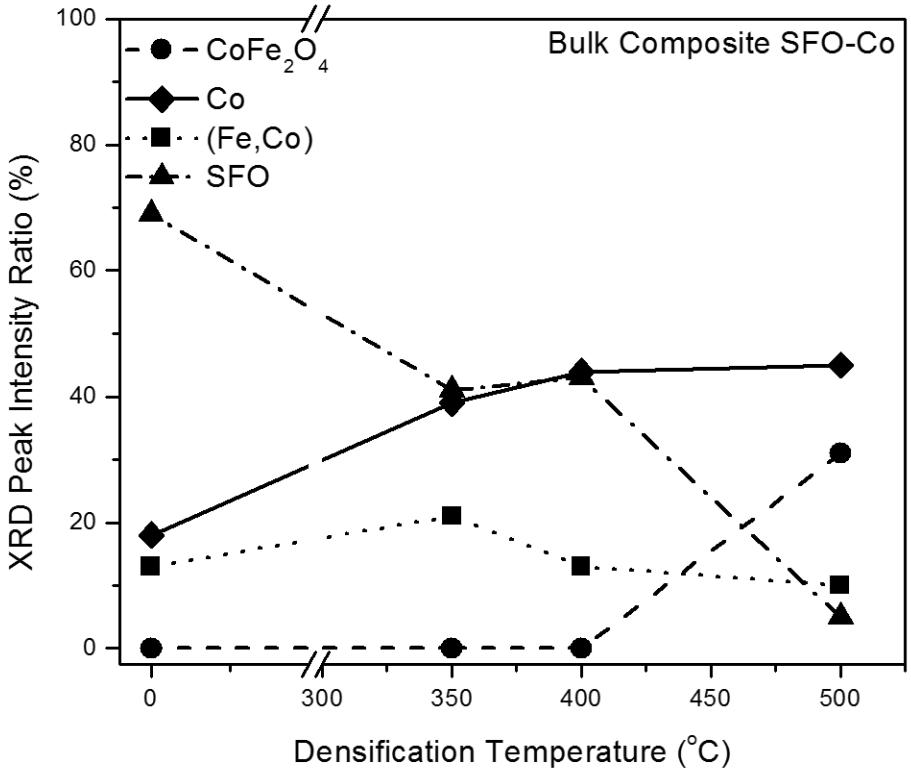

Figure 4.1.2-3 XRD peak intensities ratios of SFO/Co based densified composite at varying densification temperatures (0^{o}C is the composite powder 1hr, 1:1.96, reduced at 350^{o}C). The peak intensity ratio is the ratio of the most intense peak of a particular phase to the sum of the intensities of the most intense peaks of all identifiable phases. The most intense peaks for $CoFe_2O_4$, Co, (Fe,Co) and SFO are from the (311), (111) , (110) and (107) planes, respectively.

The density of the bulk SFO/Co based composite increases with densification temperature, as shown in **Figure 4.1.2-4**.

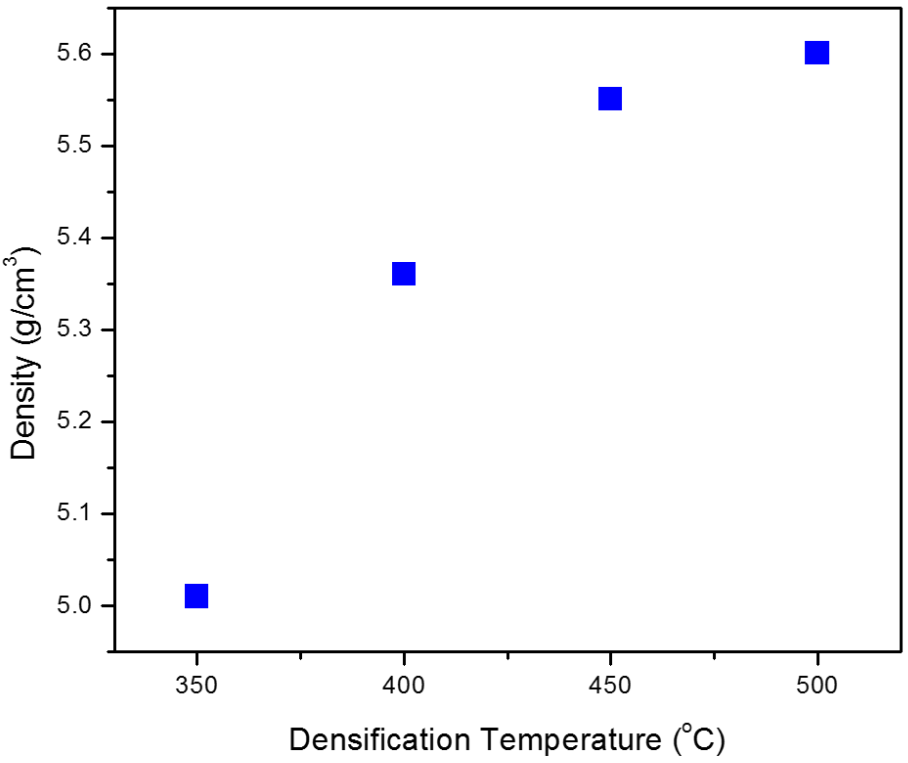

Figure 4.1.2-4 Effect of densification temperature, from 350 °C to 500 °C, on the density of bulk SFO/Co based composite.

Sample micrograph of the SFO/Co system based on the 1hr, 1:0.979 SFO:Co starting mass precipitation ratio is shown in **Figure 4.1.2-5**. The micrograph is also accompanied by EDS spectra, collected at spots pointed to by the arrows. There are several features in the micrograph. There is a more dense region in the middle of the micrograph, compared to the surrounding (especially left and top right) region. SE micrograph shows

clear topological differences between the highly porous region and the flatter region. Looking at the flatter region in the BSE micrograph, two regions of highly varying contrast are visible. The brighter region, exhibits EDS peaks belonging primarily to Co, while the darker region exhibits peaks belonging primarily to O, Fe, Sr as well as a low Co peak.

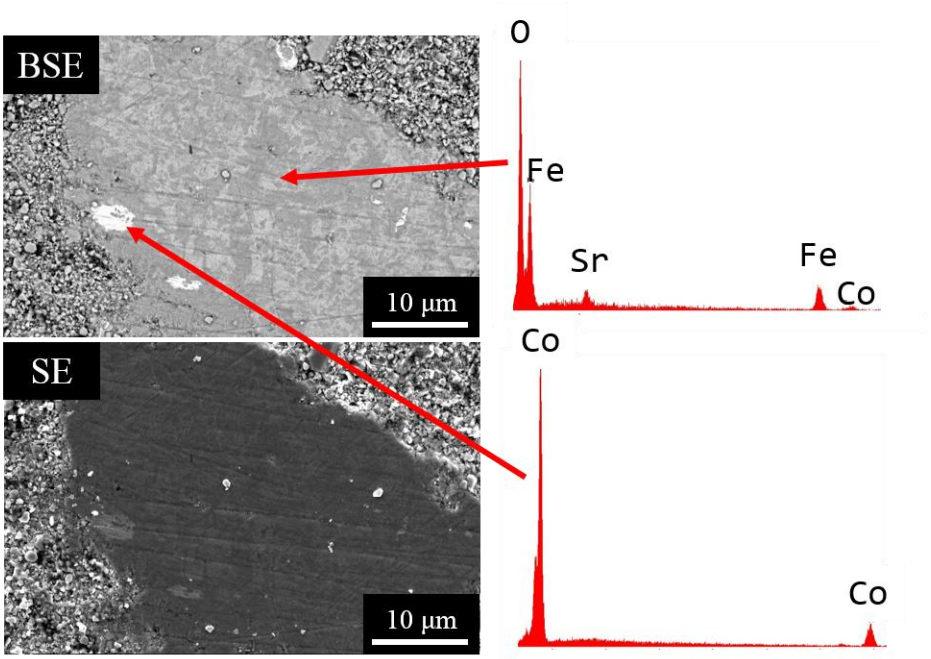

Figure 4.1.2-5 SEM micrographs and EDS spectra of densified bulk SFO/Co composite. Densification condition of 400°C 505MPa and no hold time at temperature, and powder synthesis of 1hr and 1:0.98 SFO:Co starting mass ratio is used.

The effect of varying the starting SFO:Co mass precipitation ratio on the microstructure is show in **Figure 4.1.2-6**. 1:3.92 ratio sample **(a)**, has a very high amount of lighter contrast regions, when examining the BSE 100 µm scale bar micrograph. There is not a lot of segregated Co regions. The 500 nm scale bad micrographs for the 1:3.92 ratio sample, show excellent example of densified core shell microstructure. 1:1.96 ratio sample **(b)**, has less overall amount of lighter contrast in the BSE 100µm scale bar micrograph,

however there are a lot of areas showing high amount of light contrast area segregation. Looking at the 500nm scale bar micrographs reveals very well intermixed slivers of light contrast in between darker contrast regions. 1:0.98 ratio sample **(c)**, shows very little amount of light contrast areas in the lower magnification BSE micrograph. The light contrast areas that are present are very heavily segregated. The 500 nm micrographs display high degree of porosity and show no light contrast areas (difficult to examine due to low density).

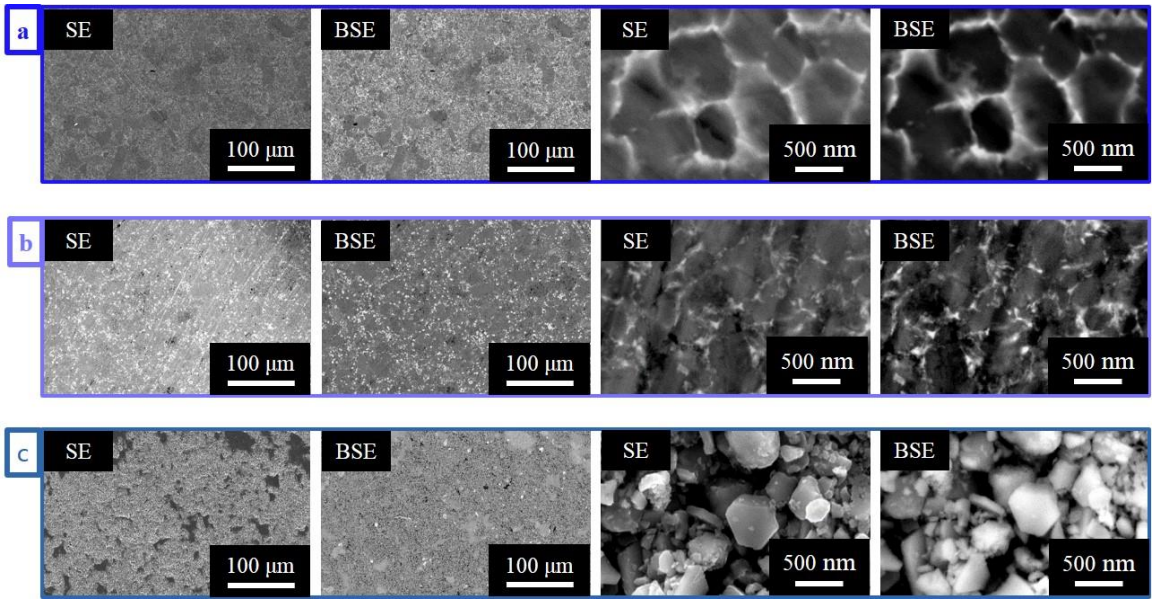

Figure 4.1.2-6 SEM micrographs of bulk SFO/Co based composite densified at 400°C, 505MPa and no hold time at temperature. Bulk samples were made of powder have a starting precipitation mass ratio of SFO:Co of (a) 1:3.92, (b) 1:1.96, and (c) 1:0.98.

Magnetic properties, and also density of varying SFO:Co starting precipitation mass ratios is shown in **Figure 4.1.2-7**. Energy product decreases with increasing ratio. M_r

peaks for the 1:1.96 ratio composite. H_c decreases with increasing ratio. M_s increases with increasing ratio. Density increases with increasing ratio.

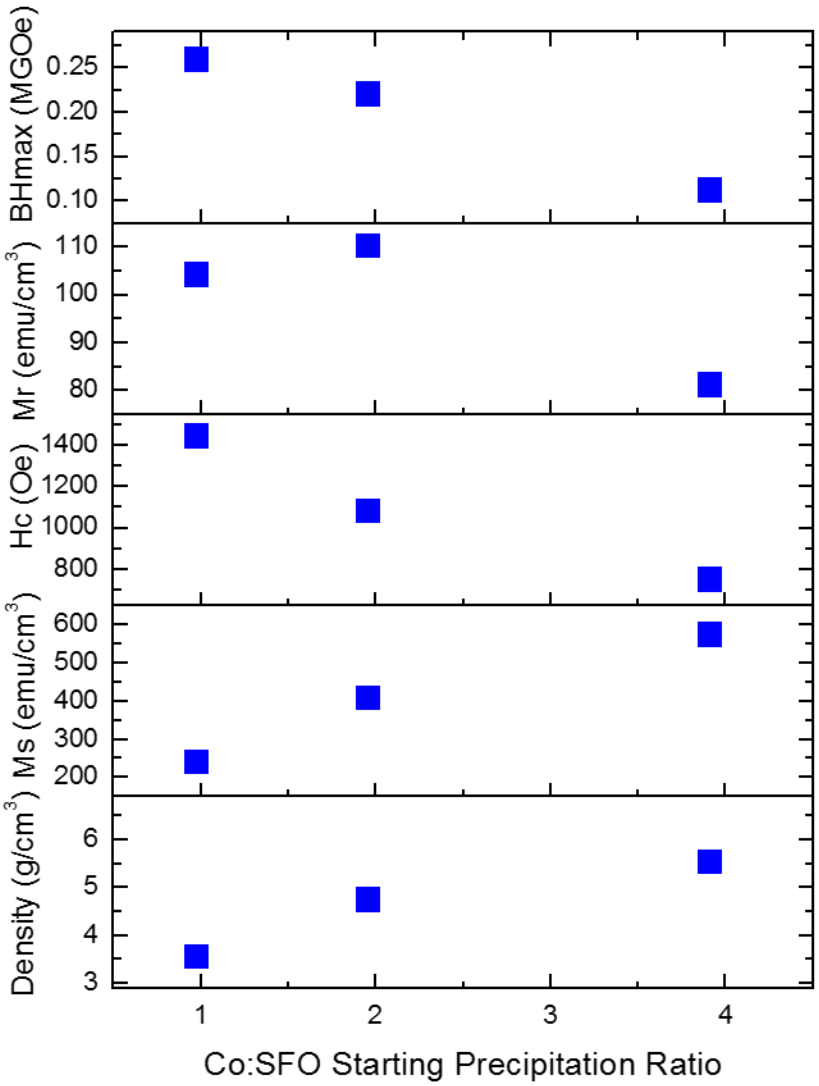

Figure 4.1.2-7 Magnetic properties and density of the SFO/Co based densified composite with varying SFO:Co starting precipitation mass ratio(initial powder reduced at 350°C, 1hr precipitation, densified at 350°C was used).

The effect of reduction temperature of the composite powder on microstructure of densified sample is shown in **Figure 4.1.2-8**. The microstructure of bulk sample made of powder reduced at **(a)** 300 ºC and **(b)** 350 ºC appear similar.

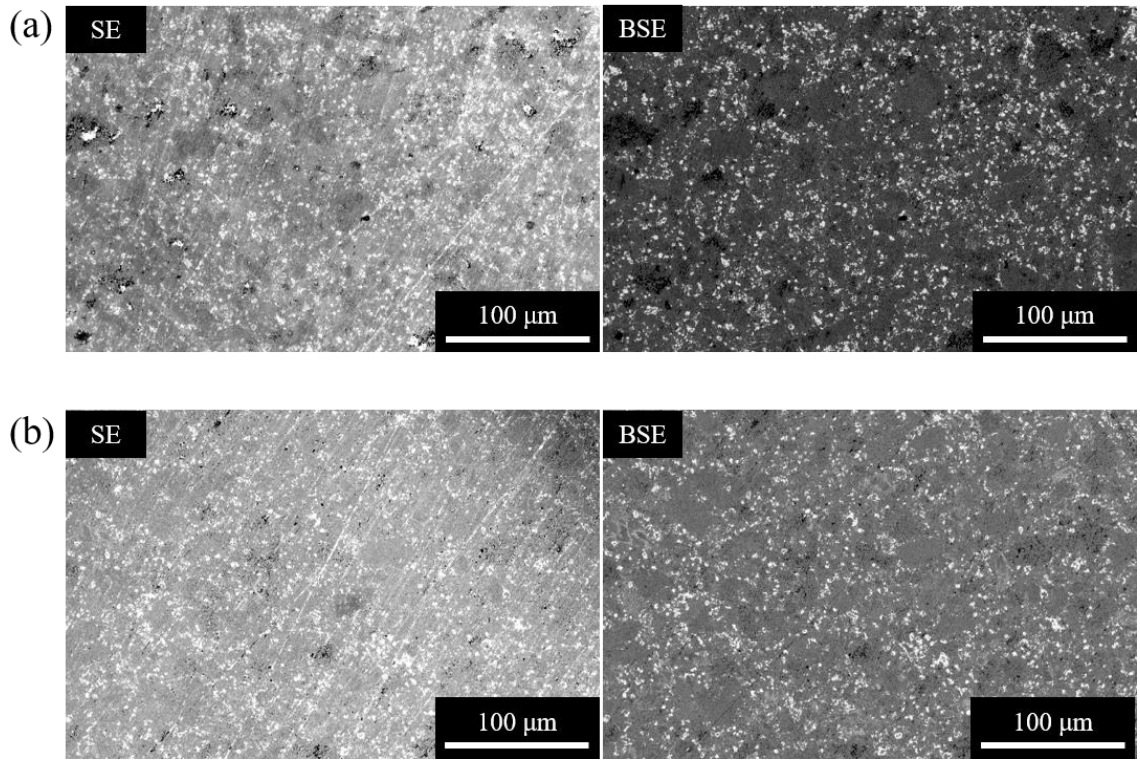

Figure 4.1.2-8 SEM micrographs of bulk SFO/Co based composite samples densified at 400ºC, 505MPa and no hold time at temperature, synthesized from powders reduced at (a) 300ºC and (b) 350ºC.

Magnetic properties, and also density of densified SFO/Co based composites of varying powder reduction temperature is shown in **Figure 4.1.2-9**. Energy product decreases as the reduction temperature is increased from 300 ºC to 350 ºC. M_r and H_c decrease with increasing reduction temperature. M_s and density increase with increasing reduction temperature.

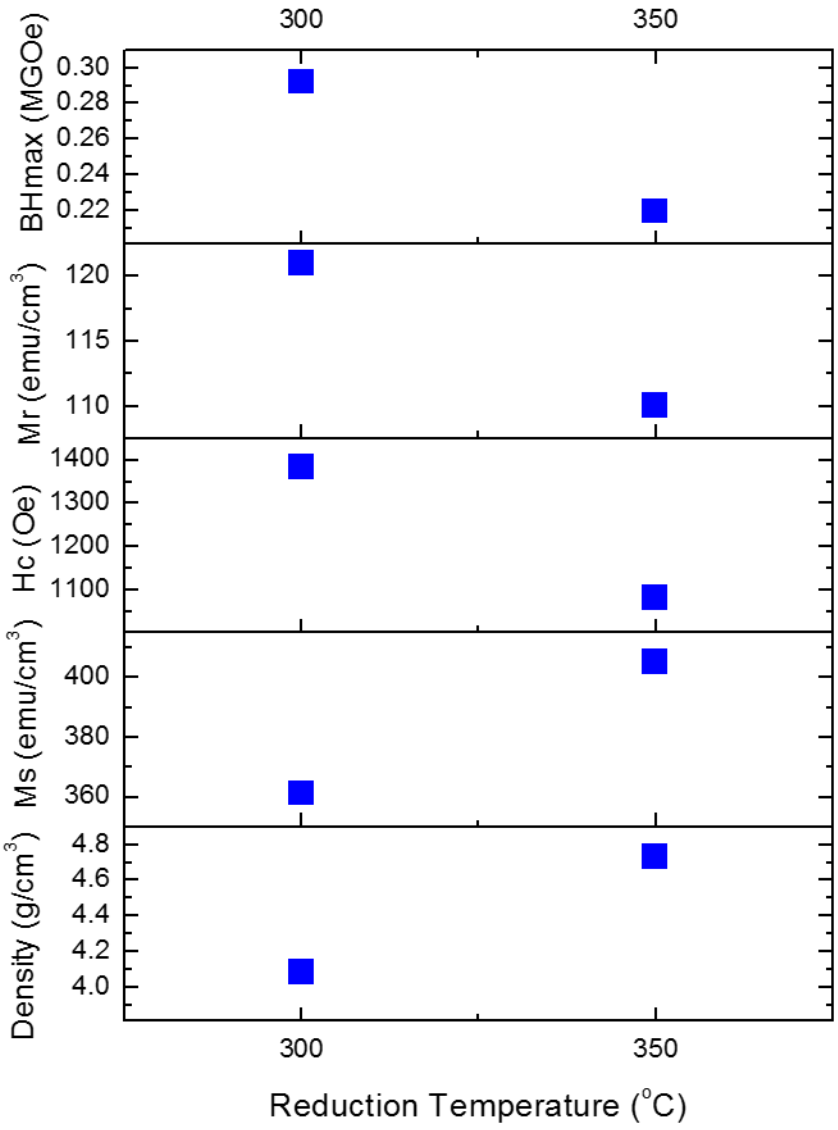

Figure 4.1.2-9 Magnetic properties and density of the SFO/Co based densified composite with varying powder reduction temperature (initial powder of SFO:Co starting precipitation ratio of 1:1.96, 1hr precipitation, densified at 350°C was used).

The effect of densification temperature on magnetic properties, and also density of densified SFO/Co based composites is shown in **Figure 4.1.2-10**. Energy product and M_r peak at 350 °C as the densification temperature is increased from 300 °C to 350 °C to

400ºC. H_c decrease with increasing densification temperature. M_s and density increase with increasing densification temperature.

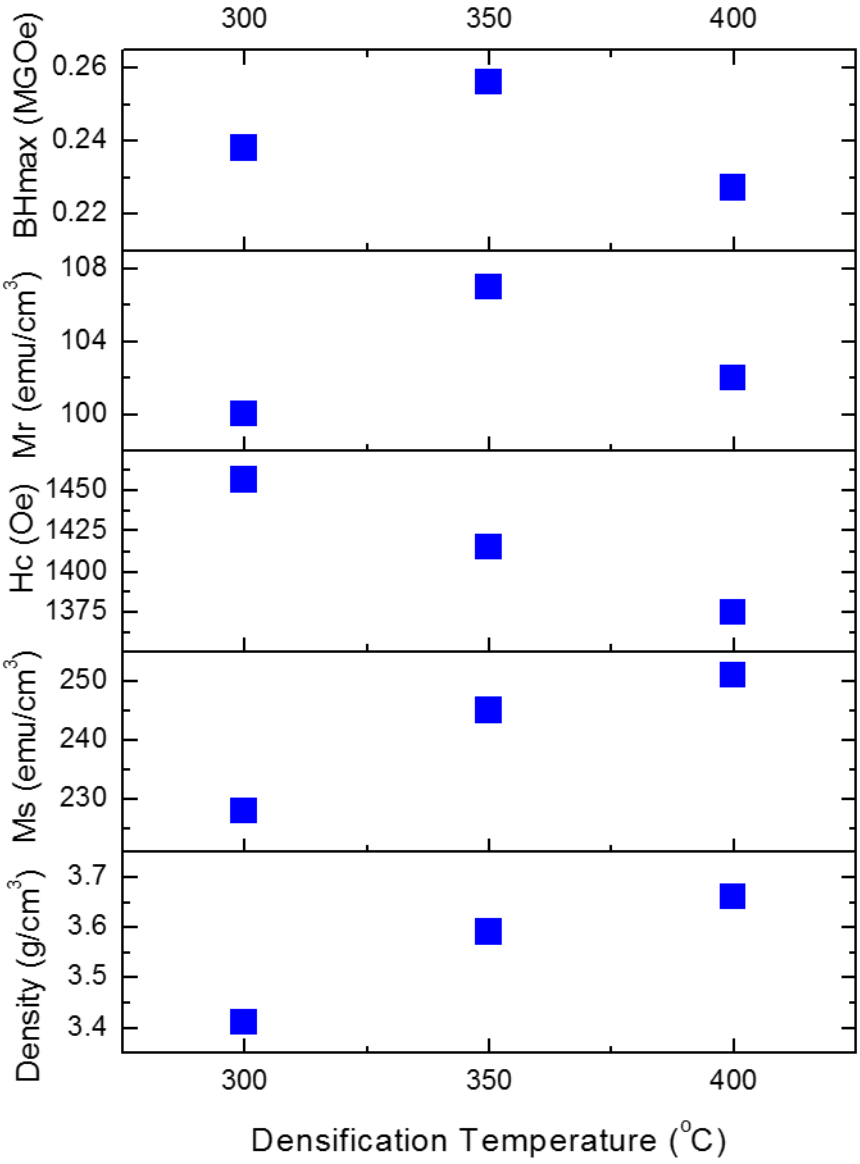

Figure 4.1.2-10 Magnetic properties and density of the SFO/Co based densified composite with varying densification temperature (initial powder with SFO:Co starting precipitation ratio of 1:1.96, 1hr precipitation, reduced at 350ºC was used).

Effect of heating rate was investigated. **Figure 4.1.2-11** shows the effect of heating rate on magnetic properties, and also density of densified SFO/Co based composites. Energy product, M_r, H_c, M_s and density all increase with increasing heating rate.

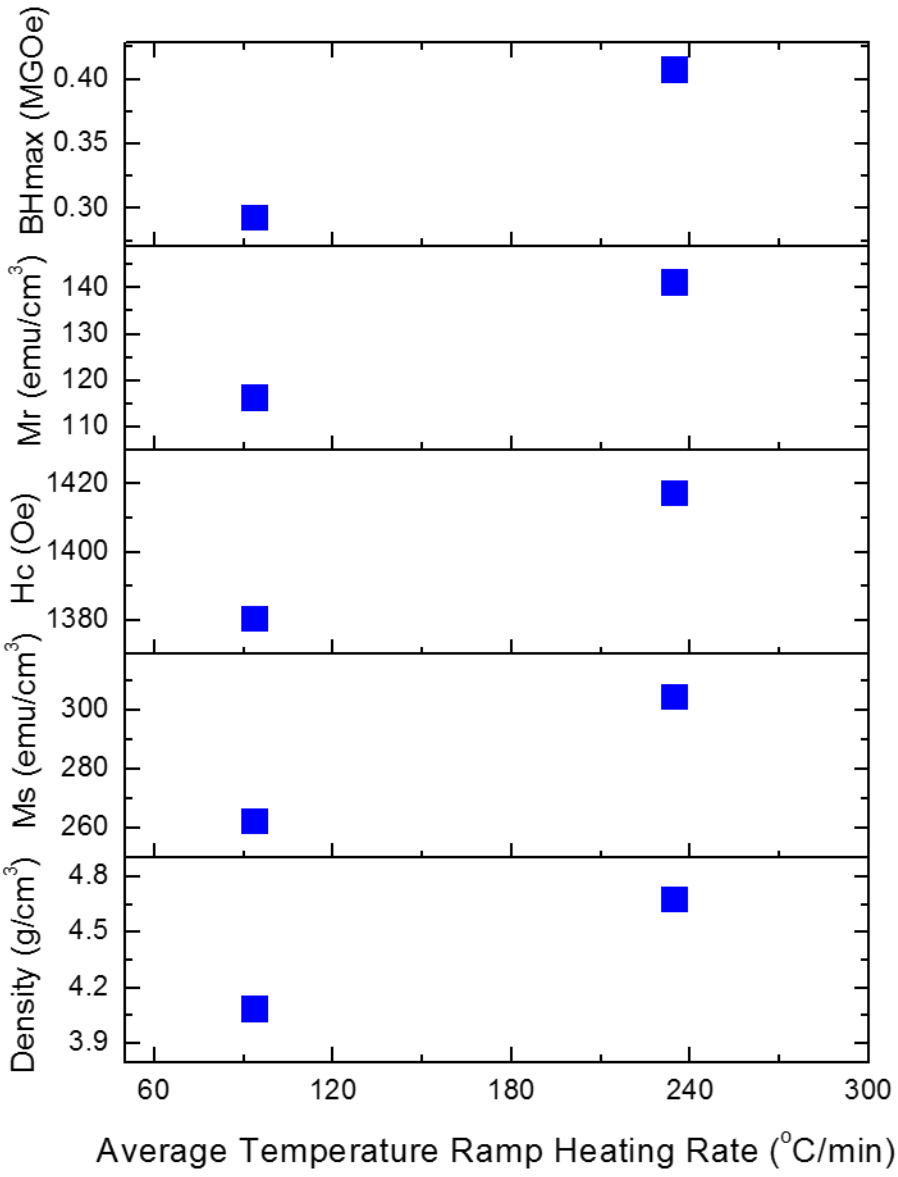

Figure 4.1.2-11 Magnetic properties and density of the SFO/Co based densified composite with varying heating rate densified at 400°C (initial powder with SFO:Co starting precipitation ratio of 1:1.96, 1hr precipitation, reduced at 300°C was used).

A comparison of microstructures between hand mixed and core-shell bulk composites is show in **Figure 4.1.2-12**. The core-shell composite microstructure **(a)**, has a

lesser degree of bright contrast area segregations, and much intermixing of dark and light contrast areas. The hand-mixed densified composite (b) has a very high degree of segregation of bright contrast areas and very poor intermixing between the bright and dark contrast areas.

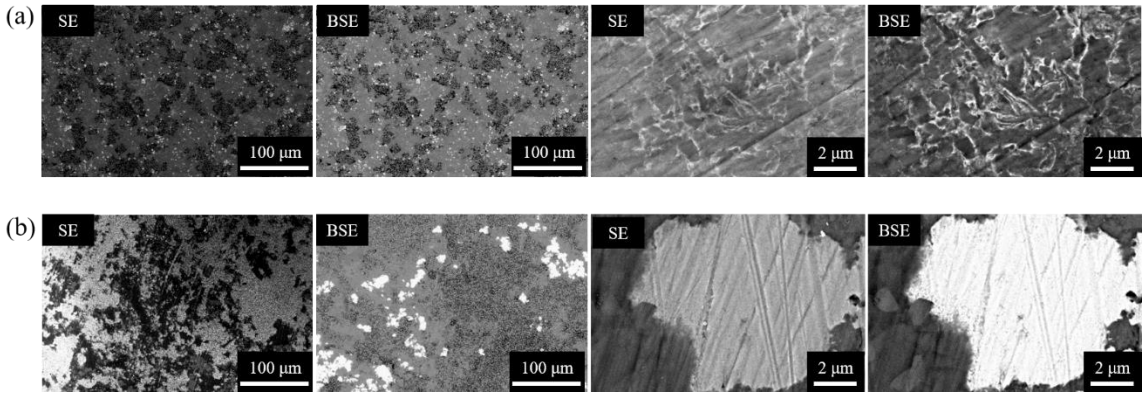

Figure 4.1.2-12 SEM micrographs of bulk SFO/Co based composite samples densified at 400°C, 505MPa and no hold (a) using precipitation synthesized core-shell powder (synthesized using 1hr, 1:1.96 powder reduced at 300°C) and (b) using hand-mixed powder

The hysteresis loops of SFO/Co based bulk composites made from hand-mixed and core-shell powders is shown in **Figure 4.1.2-13**. Although the magnetization of the hand-mixed composite is higher at 16000Oe, the magnetization of the core-shell powder is much higher at every *H* in the second quadrant.

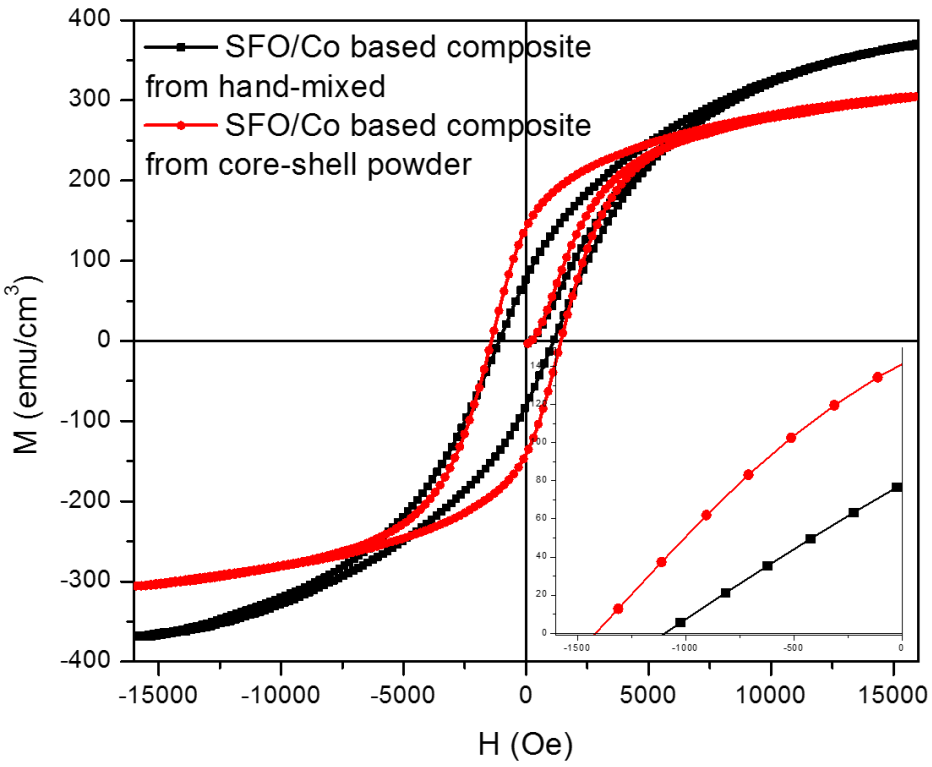

Figure 4.1.2-13 Hysteresis loop of core-shell (synthesized using 1hr, 1:1.96 powder reduced at 300°C) and hand-mixed composite, both densified using same processing conditions of 400°C, 505MPa and no hold at temperature.

The hysteresis loops of SFO/Co based core-shell bulk composites and bulk SFO is shown in **Figure 4.1.2-14**. The magnetization of the composite is higher at 16000 Oe and at most *H* values in the second quadrant. It take a higher field however, to demagnetize bulk SFO, compared to bulk composite.

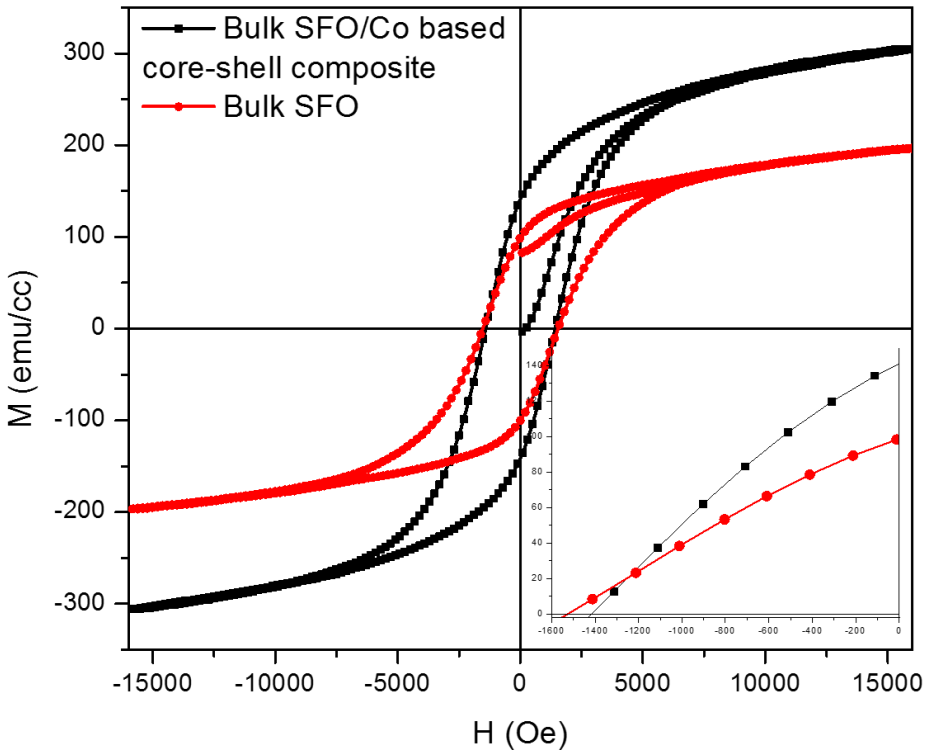

Figure 4.1.2-14 Hysteresis loop of SFO/Co based core-shell composite (synthesized using 1hr, 1:1.96 powder reduced at 300 °C) and bulk SFO, both densified using same processing conditions of 400 °C, 505 MPa and no hold at temperature.

Recoil loop measurements for the core-shell SFO/Co based bulk composite and bulk SFO are shown in **Figure 4.1.2-15**. Small loop openness is observed for both materials.

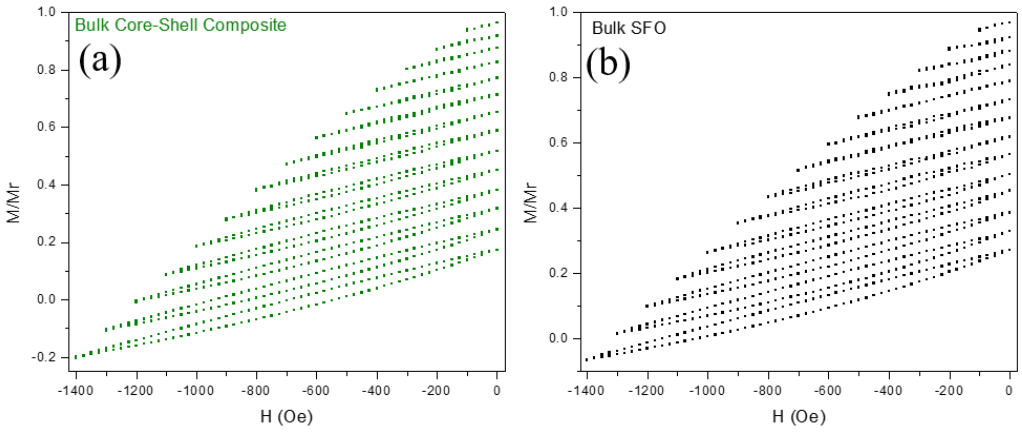

Figure 4.1.2-15 Recoil curve measurements of (a) bulk core-shell SFO/Co based composite (synthesized using 1hr, 1:1.96 powder reduced at 300 °C) and (b) bulk SFO both densified at 400 °C, 505 MPa and no hold time at temperature.

Remanence recoil ratio for the core-shell SFO/Co based bulk composite and bulk SFO are shown is seen in **Figure 4.1.2-16**. Both materials behave very similarly at low reversal fields. The composite's recoil remanence ratio become lower at higher fields.

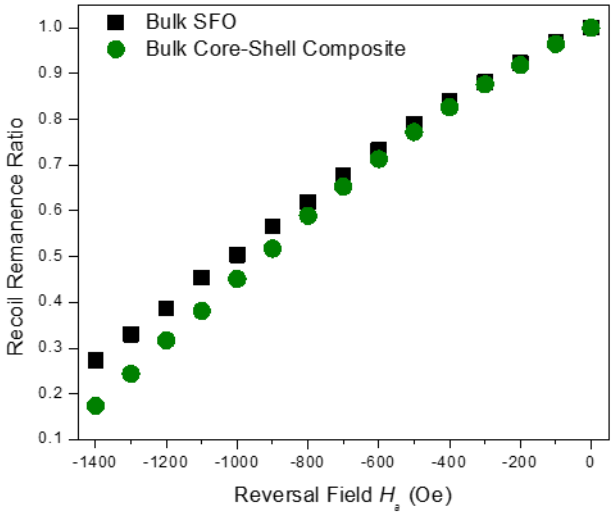

Figure 4.1.2-16 Recoil remanence ratio as a function of reversal field H_a (composite synthesized from 1hr, 1:1.96 powder reduced at 300 °C).

Normalized recoil loop area for the core-shell SFO/Co based bulk composite and bulk SFO are shown is seen in **Figure 4.1.2-17**. Both materials behave very similarly at low reversal fields. The composite's normalized recoil loop area become higher at higher reversals fields.

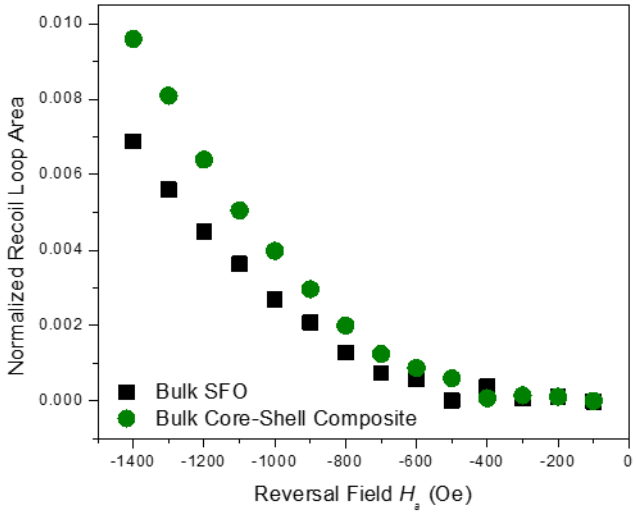

Figure 4.1.2-17 Normalized recoil loop are as a function of reversal field H_a (composite synthesized from 1hr, 1:1.96 powder reduced at 300 °C).

The δM analysis is seen for the core-shell SFO/Co based bulk composite in **Figure 4.1.2-18**. At very low fields the value of δM is positive, dropping rapidly with increasing field values.

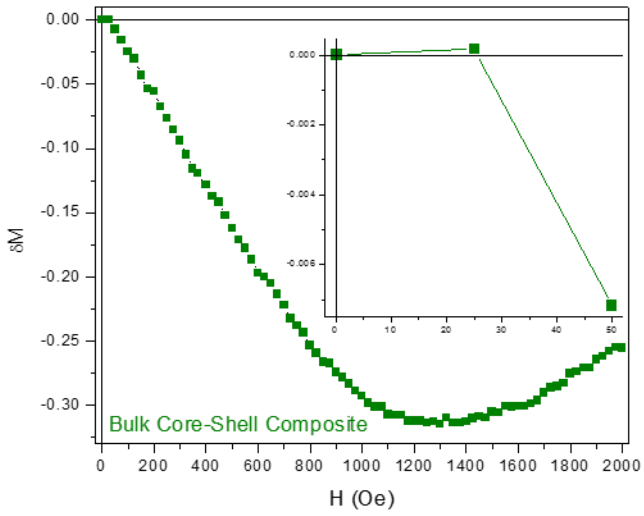

Figure 4.1.2-18 δM analysis of the bulk core-shell SFO/Co based composite densified at 400 °C, 505 MPa and no hold time at temperature (synthesized from 1hr, 1:1.96 powder reduced at 300 °C)

Various FORC diagrams are presented in Figure **4.1.2-19**. The FORC diagram of bulk SFO **(a)** shows single "hot-spot" behavior. The FORC diagram for bulk SFO/Co based composite made with powder with precipitation SFO:Co mass ratio of 1:3.92 **(b)**, shows several "hot-stops". The FORC diagram for bulk SFO/Co based composite made with powder with precipitation SFO:Co mass ratio of 1:1.96 **(b)**, shows single "hot-stop" and is higher in intensity than that of bulk non-composite SFO.

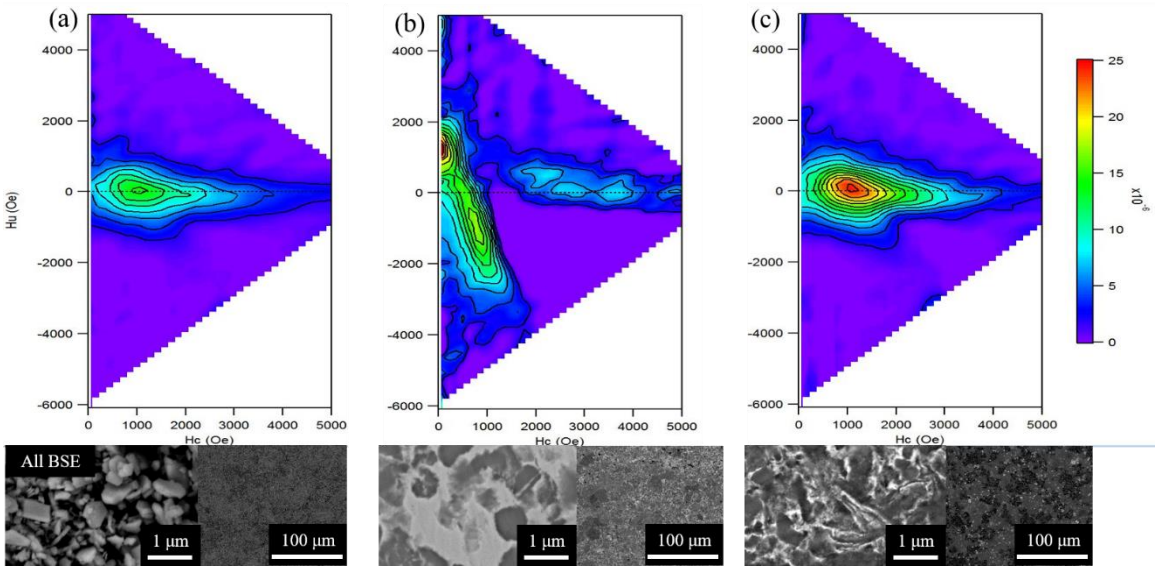

Figure 4.1.2-19 FORC diagrams of bulk samples densified at the same densification conditions of 400°C, 505MPa and no hold time at temperature of (a) SFO, (b) SFO/Co based composite made with powder with initial precipitation SFO:Co mass ratio of 1:3.92 and (c) SFO/Co based composite made with powder with initial precipitation SFO:Co mass ratio of 1:1.96 (composites synthesized from 1hr powder reduced at 300 °C).

4.1.3 Discussion

Discussion of the bulk composite starts with a simple question of why go through the trouble of precipitating the soft phase. Hysteresis curves of hand mixed SFO/Co composite and bulk as received SFO are compared in **Figure 4.1.2-1**. Both materials were densified at the same conditions that they would be most comparable. M_s of the composite is much higher than that of the SFO, suggesting a large amount of soft phase. If this composite was exchange-coupled, the high magnetization should carry over into an improvement in M_r. This is not the case. The M_r of the composite is lower than that of the single phase SFO, suggesting decoupled behavior. H_c of the composite is also lower, as expected with a higher volume fraction of soft phase. Hand mixing did not improve

magnetic properties (with the exception of M_s) of the composite compared to single phase SFO. Precipitation route must hence be implemented, to achieve the engineering feat of nano-scale mixing between the hard and soft phases, in hopes of bulk exchange-coupled nano-composite.

Porosity dilutes the performance of the PM. As expected, **Figure 4.1.2-4** shows that density increases with densification temperature. XRD data in **Figure 4.1.2-2** and XRD peak intensity ratios in **Figure 4.1.2-3** show phase evolution of the composite under elevated densification temperatures. Densifying the oxide/metal composite powder at relatively low densification temperature of 350 ^{o}C causes a decrease of SFO and an increase in Co and (Fe,Co) metal soft phases (soft phase solid solution is discussed in **Section 3.2.3**). It is apparent that densification further promotes the decomposition reaction of SFO, with Co as catalyst. This is likely due to increased surface interface between SFO and Co under densification. Relatively high pressure during processing causes particle rearrangement, and soft Co metal likely "flows" between SFO particles, increasing interaction area between the two phases. At densification temperature of 500 ^{o}C, the SFO is almost completely diminished, and $CoFe_2O_4$ phase appears. It is clear that in order to keep the desired SFO hard phase with proper hard/soft ratio, densification temperature must be kept low. However, in order to synthesize a composite with relatively high density, high densification temperature is preferred. These competing effects between density and reaction narrow the processing window, making engineering bulk oxide-metal exchange-coupled nano-composite an engineering feat.

Microstructure of the bulk composite, densified from precipitated SFO/Co based composite powder is highly affected by factors such as SFO:Co initial mass precipitation ratio. **Figure 4.1.2-5** shows poor soft phase distribution, but serves the purpose of clearly identifying BSE contrast belonging to Co and SFO. EDS spot check of the bright region reveals mostly Co signature, while EDS spot check of darker area reveals EDS signature of mostly Sr, Fe and O belonging to SFO. Changing the SFO:Co initial mass precipitation ratio appears to change more than just the amount of precipitated soft phase, as seen in **Figure 4.1.2-6**. SFO:Co ratio of 1:3.92 **(a)**, creates microstructure of well dispersed soft phase, without much agglomeration. Unfortunately, the amount of Co (light contrast) in the microstructure is too high for effective exchange-coupling. SFO:Co ratio of 1:1.98, **(b)** lowers the overall amount of visible Co, at the expense of introduction of some segregated soft phase regions, visible under low magnification. High magnification of this microstructure, however, reveals finely intermixed slivers of Co based material in between SFO grains. In an attempt to lower the amount of soft phase even further, 1:0.98 SFO:Co ratio is used **(c)**. This produces areas of high Co segregation, visible under low magnification. High magnification displays very high degree of porosity, suggesting lack of Co to "flow" in between SFO grains; Co improves density of high SFO:Co ratio samples. Lack of fine Co in the microstructure of 1:0.98 SFO:Co ratio sample suggests 1:0.98 ratio improper for exchange-coupled nano-composite.

Magnetic properties and density as function of Co:SFO ratio, in **Figure 4.1.2-7**, are consistent with microstructural observations. High degree of visible porosity in 1:0.98 SFO:Co ratio sample corresponds to the lowest measures density of the ratios studied.

Though the 1:3.92 SFO:Co ratio produces the most dense sample, with the largest M_s, lack of H_c and M_r puts this sample in last place in terms of energy product, suggesting high degree of decoupled soft phase. Although the energy product of 1:0.98 SFO:Co ratio powder was highest, microstructure was lacking well interphased SFO/Co,(Fe,Co) boundaries. Based on having the highest *Mr*, and good nano-mixed microstructure, 1:1.96 ratio was chosen for further investigation.

While the microstructure of bulk SFO/Co based composite made of powder reduced at different temperatures looks similar (**Figure 4.1.2-8**), magnetic properties are vastly different (**Figure 4.1.2-9**). Although denser, and having higher *Ms*, the bulk composite made of powder reduced at 350 ^{o}C showed significantly lower energy product. *Mr* and *Hc* of the 350 ^{o}C reduced sample were also lower. It is likely that reaction at elevated reduction temperature caused a lower than optimal hard/soft ratio.

Densification temperature is shown to have strong influence on magnetic properties in **Figure 4.1.2-10**. While having highest density and *Ms*, bulk composite densified at 400 ^{o}C has the lowest energy product. This result suggests reaction to a hard/soft ratio too rich with soft phase. While having middle of the pack density, M_s and H_c, bulk composite densified at 350 ^{o}C has the highest M_r and energy product, suggesting that it has the optimal hard/soft ratio for close to ideal exchange-coupling. SFO/Co based composite powder synthesized using 1hr, 1:1.96 ratio, reduced at 300 ^{o}C and densified at 350 ^{o}C yield the highest yet energy product; these optimized processing parameters were used for future studies. In order to further control unfavorable reaction, the time spent at elevated CAPAD temperatures was limited by a high temperature heating rate (while processing at 400^{o}C).

Figure 4.1.2-11 shows improvement in all magnetic properties, along with density because of high heating rate. Likely, the more ideal hard/soft ratio of lower densification temperatures along with higher density of higher densification temperatures was achieved through high heating rate. The bulk composite synthesized under these processing conditions is referred to as optimized composite.

Comparing microstructure of hand-mixed composite with optimized composite made of precipitated core-shell powder gives clues to the lack of high performance properties of the hand mixed composite. **Figure 4.1.2-12 (b)** shows that the microstructure of the hand mixed composite has very highly segregated regions of Co based soft phase, compared to the optimized precipitated core-shell composite **(a)**. Magnetic properties of the two composites are displayed in **Figure 4.1.2-13**. While the hand mixed composite has a higher M_s, the exchange-coupling in the optimized core-shell precipitated composite has much higher M_r, H_c and energy product due to exchange-coupling. The optimized core-shell composite has even higher magnetization in most of the second quadrant than bulk single phase SFO (**Figure 4.1.2-14**). This project has been successful in synthesizing an exchange-coupled composite with improved magnetic properties compared to single phase hard phase, without the use of RE or precious elements.

Recoil remanence ratio in **Figure 4.1.2-16** show that the optimized composite is as resilient to demagnetization as the single phase bulk SFO at low reversal fields, and slightly less resilient to demagnetization at higher recoil fields. Similarly, Recoil loops of the SFO/Co composite are as closed as those of bulk SFO at low H_a, seen through normalized

recoil loop area in **Figure 4.1.2-17**. This finding suggests high degree of exchange-coupling at low to moderate H_a values which breaks down at increased -H_a values.

The positive δM value in **Figure 4.1.2-18** shows further evidence of exchange-coupling interaction at low H_a values, in agreement with the recoil measurements. . Lastly, **Figure 4.1.2-19** shows FORC diagram for bulk SFO, composite with too low of a hard/soft phase fraction (non-optimized), and composite with optimized hard/soft fraction. Multiple "hotspots" compared to single "hotspot" is observed in non-optimized hard/soft ratio composite, compared to bulk SFO and exchange-coupled optimized single phase composite. Through optimization of powder synthesis, and fine control of microstructure and composition through a well-established processing window, a 70% improvement in energy product of bulk, RE free, exchange-coupled nano-composite is observed, compared to single phase bulk SFO hard phase.

5 Conclusion and Future Directions

5.1 Summary and Conclusion

Performance of PMs is tied to the efficiency of renewable energy and other green technologies. Improving the properties of PMs will have a large spread, long term effect in benefit to humanity. State of the art RE based PMs are environmentally damaging and costly to mine, separate and process from ore to metal. Using nano-scale materials engineering, improvements in magnetic properties of magnets could be achieved. Applying these techniques to PMs made from earth abundant materials could lower the reliance on environmentally damaging RE based magnets.

Effective exchange-coupling requires high amount of interphase area between two different magnetic phases. Metals, such as Fe and Co, with their high volume magnetization and oxide, such as $SrFe_{12}O_{19}$, with high coercivity are well suited for an exchange-coupled nano-composite PM. However, it is incredibly difficult to achieve nano-scale mixing and clean interphases between oxide and metal due to their affinity to react with each other.

In this work, a simple and scalable approach was developed for synthesizing exchange-coupled powder. A two-step procedure was involved. During the first step, soft phase precursor was precipitated on the surface of hard phase. During the second step the precipitated soft phase precursor was reduced to soft phase in a reducing environment. Very fine control and effect of synthesis conditions including reactant ratios, precipitation time and reduction time and temperature was demonstrated and understood. A narrow

processing window for optimal hard/soft ratio was painstakingly developed. Through the synthesis route established in this work, composite powder with improved energy product, compared to either of the two constituent phases was synthesized.

Many applications of PMs including PM based generators and motors rely on the use of magnets in bulk 3D form, i.e. powders and thin films cannot be used. It is highly unlikely to achieve the necessary microstructures (clean unreacted interfaces and nano-length scales) with traditional sintering techniques. t. Since effective exchange-coupling relies on inter-grain interactions at the nano-scale, non-traditional processing technique was implemented. CAPAD allowed for processing of exchange-coupled powder into bulk exchange-coupled samples. Notably, nano-scale mixing of hard and soft phases was retained as powders transformed into bulk samples. Through fine control of pressure, temperature, hold time and heating rate, optimized processing window was developed for synthesizing oxide/metal bulk nano-composite materials. Incredibly, a 70.3% improvement in energy product of bulk composite compared to bulk hard phase was observed. To my knowledge, nobody else has been able to attain improvements higher than 70% in RE and precious metal free exchange-coupled PMs. Processing technique developed in this dissertation paves the way forward for use of earth abundant materials in high performance PM applications.

5.2 Future Considerations

While a 70% improvement in energy product is a significant achievement, samples synthesized do not outperform commercially made ferrite magnets. The hard phase used in

here was chosen for a proof-of-concept study, and does not have the highest coercivity available in RE free PMs. Future direction for this project could involve the use of synthesis and processing procedure developed here using a hard phase with higher coercivity.

Optimization of single phase PMs typically requires grain alignment. Aligned, anisotropic, PMs have improved properties in specific directions. Applying alignment to exchange-coupled nano-composites would improve properties further, and the performance of the PMs in unidirectional applications would increase. Some alignment studies using CAPAD have already been done[21]. Flake like particles tend to orient themselves with the flake out-of-plane direction, parallel to the load direction in CAPAD. Preferential grain growth at elevated temperatures is also likely responsible for alignment during processing.

The easy magnetization direction for a single SFO flake is out-of-plane of the flake, assuming faceted hexagonal flakes are of single crystallographic orientation with C-axis out-of-plane of the flake. **Figure 5.2-1** shows preliminary data for alignment of bulk SFO. Magnetic properties in the second quadrant vary with measurement direction. The best properties are for field applied out-of-the plane of the sample, parallel to the load direction, suggesting easy direction alignment out-of-plane of the sample. This is in agreement with the hypothesis of flakes orienting with flake out-of-plane direction becoming parallel to the load direction in the CAPAD. XRD further confirms these findings. As the powder is densified, peaks belonging to (00X) planes grow while those belonging to (XX0) planes shrink, also suggesting flakes orienting with flake out-of-plane direction aligning parallel to the load direction in the CAPAD. Further investigation of the effect of processing

condition on degree of alignment could prove very beneficial for additional improvement in magnetic properties of exchange-coupled PMs synthesized through CAPAD processing.

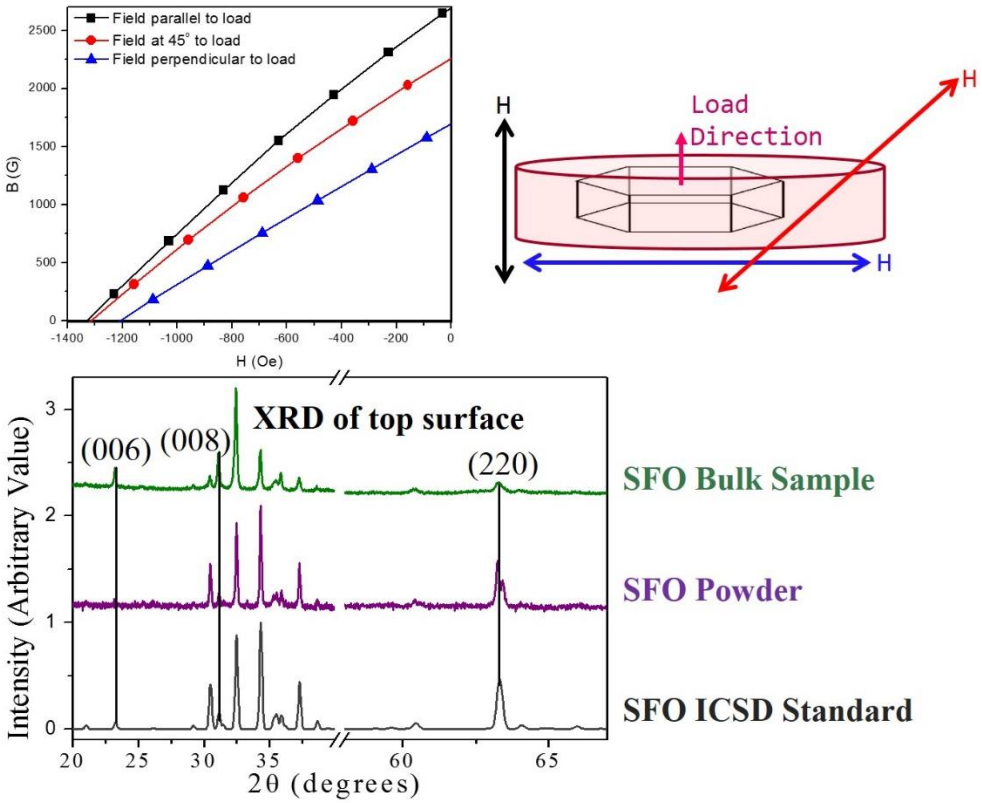

Figure 5.2- 1 Texturing in CAPAD processed bulk SFO, shown through magnetic and XRD data

Appendix

Sample Soft Phase Thickness Calculation

Microstructure was assumed to be composed of identical regular prismatic hexagonal SFO flakes with the distance between two parallel edges of the hexagonal face of the prism to be l_{SFO}. After some trigonometric analysis, l_{SFO} was expressed using the diameter of the regular hexagon, d_{SFO} and side length a_{SFO} of the hexagon was expressed as:

$$l_{SFO} = \frac{d_{SFO}\sqrt{3}}{2} \quad (1)$$

$$a_{SFO} = \frac{l_{SFO}}{\sqrt{3}} \quad (1)$$

The face area of a hexagon, A_{SFO}, was written as:

$$A_{SFO} = \frac{3\sqrt{3}}{2}\, a_{SFO}^2 \quad (2)$$

Assuming h_{SFO} to be the height of the hexagonal prism, the volume of a single hexagonal SFO flake, V_{SFO}, was written as:

$$V_{SFO} = \frac{3\sqrt{3}}{2}\, a_{SFO}^2 h_{SFO} \quad (3)$$

Combining (1) and (3) gave:

$$V_{SFO} = \frac{3\sqrt{3}}{2}\, (\frac{l_{SFO}}{\sqrt{3}})^2 h_{SFO} \quad (3b)$$

The Fe_3O_4 particles are assumed to have uniform coating around the the prismatic hexagonal SFO flakes. The thickness of the coating is t. The length $l_{composite}$ for the SFO/Fe3O4 nanocomposites was the distance between two parallel edges of the hexagonal face. The side length of the composite particle was expressed as $a_{composite}$. The height of the

composite prismatic hexagonal particles was $h_{composite}$. $l_{composite}$, $a_{composite}$ and $h_{composite}$ were expressed as:

$$l_{composite} = l_{SFO} + 2t \quad (4)$$

$$a_{composite} = \frac{l_{composite}}{\sqrt{3}} = \frac{l_{SFO}+2t}{\sqrt{3}} \quad (5)$$

$$h_{composite} = h_{SFO} + 2t \quad (6)$$

The volume of a single composite flake, $V_{composite}$, was expressed as:

$$V_{composite} = \frac{3\sqrt{3}}{2} a_{composite}^2 h_{composite} \quad (7)$$

(5) and (6) were then substituted into (7), giving:

$$V_{composite} = \frac{3\sqrt{3}}{2} (\frac{l_{SFO}+2t}{\sqrt{3}})^2 (h_{SFO} + 2t) \quad (8)$$

Volume of the soft phase layer of one composite flake, $V_{soft\ phase}$, was calculated to be:

$$V_{soft\ phase} = V_{composite} - V_{SFO} \quad (9)$$

Combining (3), (8) and (9) gave:

$$V_{soft\ phase} = (\frac{3\sqrt{3}}{2} \left(\frac{l_{SFO}+2t}{\sqrt{3}}\right)^2 (h_{SFO} + 2t)) - (\frac{3\sqrt{3}}{2} (\frac{l_{SFO}}{\sqrt{3}})^2 h_{SFO}) \quad (10)$$

The total volume of soft phase, $V_{soft\ phase\ total}$, is given by multiplying V_{soft} phase by the number of SFO particles, n_{SFO}, in the precipitation process:

$$V_{soft\ phase\ total} = V_{soft\ phase}\ n_{SFO} \quad (11)$$

Combining (10) and (11) gave:

$$V_{soft\ phase\ total} = \left[(\frac{3\sqrt{3}}{2} \left(\frac{l_{SFO}+2t}{\sqrt{3}}\right)^2 (h_{SFO} + 2t)) - (\frac{3\sqrt{3}}{2} (\frac{l_{SFO}}{\sqrt{3}})^2 h_{SFO})\right] n_{SFO}$$

(12)

d_{SFO} and h_{SFO} was taken to be 1.12 μm and 0.16 μm, respectively. These values were measured from particle size analysis of the as received SFO powder. These values gave a V_{SFO} value of 1.30×10^{-19} m^3.

n_{SFO} was calculated the following way. The mass of starting SFO powder mSFO was divided by the density of bulk SFO to give the total volume of starting SFO particles, $V_{SFO\ total}$, of 3.18×10^{-7} m^3. n_{SFO} was calculated to be 2.45×10^{12} particles by:

$$n_{SFO} = \frac{V_{SFO\ total}}{V_{SFO}} \quad (13)$$

$V_{soft\ phase\ total}$ was calculated in the following way. The yield of precipitation was obtained by the gravimetric analysis based method. The collected solution post precipitation (separated from the composite particles) was dried and calcined at 800 ºC for 6 h in air atmosphere. The residue remaining after calcination was α-Fe_2O_3 single phase which was confirmed by X-ray diffraction analysis. The amount of α-Fe_2O_3 was used to calculate yield of the precipitation process. The volume ratio of hard/soft phase (Fe_3O_4/ SFO) was 45/55 giving $V_{soft\ phase\ total}$ of 2.60×10^{-7} m^3. Equation 12 was solved for t using numerical methods. The precipitated Fe_3O_4 thickness was estimated to be *43nm*.

Sample MATLAB Code for Recoil Area Calculation

```
clear all
A = xlsread('magnetizationCurve.xlsx');
X1 = A(:,1);
Y1 = A(:,2);

B = xlsread('demagnetizationCurve.xlsx');
X2 = B(:,1);
Y2 = B(:,2);

R1 = trapz(X1,Y1);
R2 = trapz(X2,Y2);

R = -1*R1 - R2
```

Sample MATLAB Code for the Manipulation of FORC Data For FORCInel

```
clear all
A = xlsread('FORCdatanormalizedbyVolume.xlsx');
X = A(:,1);
Y = A(:,2);
X1 = zeros(1);
Y1 = zeros(1);

n = length(X)-1;
j=1;
for i=1:n;
    if X(i)<=X(i+1);
        X1(j)=X(i);
        Y1(j)=Y(i);


    else
    X1(j)=[0];
    Y1(j)=[0];

        if X1(j)~=0
            continue
        end

    end
    j=j+1;
    i=i+1;
end

A1=[X1;Y1]';

plot(X1,Y1,'.')
xlswrite(' FORCdatanormalizedbyVolumeMODIFIED.xlsx',A1)
```

Work Cited

[1] ReportBuyer, "Permanent Magnets - Types , applications , new developments , industry structure and global markets," London, pp. 1–20, 03-Sep-2014.

[2] R. W. Lee, "Hot-pressed neodymium-iron-boron magnets," *Appl. Phys. Lett.*, vol. 46, no. 8, p. 790, 1985.

[3] M. Sagawa, S. Fujimura, H. Yamamoto, Y. Matsuura, and K. Hiraga, "Permanent magnet materials based on the rare earth-iron-boron tetragonal compounds," *IEEE Trans. Magn.*, vol. 20, no. 5, pp. 1584–1589, Sep. 1984.

[4] C. Bontron, "Rare-earth mining in China comes at a heavy cost for local villages," *Guard.*, vol. 7 August, pp. 5–7, 2012.

[5] C. Milmo, "Concern as China clamps down on rare earth exports," *Independent*, p. http://www.independent.co.uk/news/world/asia/conce, 01-Jan-2010.

[6] N. Jones, "THE PULL OF STRONGER MAGNETS," *Nature*, vol. 472, pp. 22–23, 2011.

[7] C.-W. YAP, "China Ends Rare-Earth Minerals Export Quotas," pp. 5–8, 05-Jan-2015.

[8] B. Bauer, D., Diamond, D., Li, J., Sandalow, D., Telleen, P., Wanner, "Critical Materials Strategy," *US Dep. Energy*, no. December, pp. 1–166, 2010.

[9] M. Humphries, "Rare Earth Elements : The Global Supply Chain," *CRS Rep. Congr.*, 2013.

[10] E. F. Kneller and R. Hawig, "The Exchange-Spring Magnet: A New Material Principle for Permanent Magnets," *IEEE Trans. Magn.*, vol. 27, no. 4, pp. 3588–3600, 1991.

[11] R. Skomski and J. M. D. Coey, "Giant energy product in nanostructured two-phase magnets," *Phys. Rev. B*, vol. 48, no. 21, pp. 15812–15816, 1993.

[12] L. Zhang and Z. Li, "Synthesis and characterization of SrFe 12 O 19 / CoFe 2 O 4 nanocomposites with core-shell structure," vol. 469, pp. 422–426, 2009.

[13] V. Nandwana, G. S. Chaubey, K. Yano, C. Rong, and J. P. Liu, "Bimagnetic nanoparticles with enhanced exchange coupling and energy products," *J. Appl. Phys.*, vol. 105, no. 1, p. 014303, 2009.

[14] X. Liu, S. He, J.-M. Qiu, and J.-P. Wang, "Nanocomposite exchange-spring magnet

synthesized by gas phase method: From isotropic to anisotropic," *Appl. Phys. Lett.*, vol. 98, no. 22, p. 222507, 2011.

[15] C.-B. Rong, V. Nandwana, N. Poudyal, J. P. Liu, M. E. Kozlov, R. H. Baughman, Y. Ding, and Z. L. Wang, "Bulk FePt-based nanocomposite magnets with enhanced exchange coupling," *J. Appl. Phys.*, vol. 102, no. 2, p. 023908, 2007.

[16] K. J. Strnat, "Modern permanent magnets for applications in electro-technology," *Proc. IEEE*, vol. 78, no. 6, pp. 923–946, Jun. 1990.

[17] N. Poudyal and J. Ping Liu, "Advances in nanostructured permanent magnets research," *J. Phys. D. Appl. Phys.*, vol. 46, no. 4, pp. 043001–043023, Jan. 2013.

[18] O. Gutfleisch, "Controlling the properties of high energy density permanent magnetic materials by different processing routes," *J. Phys. D. Appl. Phys.*, vol. 33, no. 17, pp. R157–R172, 2000.

[19] A. Cochardt, "Recent ferrite magnet developments," *J. Appl. Phys.*, vol. 37, no. 3, pp. 1112–1115, 1966.

[20] J. J. Becker, "Rare-earth-compound permanent magnets," *J. Appl. Phys.*, vol. 41, no. 3, pp. 1055–1064, 1970.

[21] J. Morales, "Tailoring Magnetic Properties in Bulk Nanostructured Solids," University of California, Riverside, 2011.

[22] J. I. Hoppe, "Effective magnetic moment," *J. Chem. Educ.*, vol. 49, no. 7, p. 505, 1972.

[23] G. Bertotti, *Hysteresis in Magnetism*. Elsevier, 1998.

[24] U. Anselmi-Tamburini, J. E. Garay, Z. a. Munir, a. Tacca, F. Maglia, G. Chiodelli, and G. Spinolo, "Spark plasma sintering and characterization of bulk nanostructured fully stabilized zirconia: Part II. Characterization studies," *J. Mater. Res.*, vol. 19, no. 11, pp. 3263–3269, 2004.

[25] R. Coehoorn, D. B. D. E. Mooij, and C. D. E. Waard, "Meltspun permanent magneti materials containing Fe3B as the main phase," *J. Magn. Magn. Mater.*, vol. 80, pp. 101–104, 1989.

[26] R. F. Sabiryanov and S. S. Jaswal, "Magnetic properties of hard/soft composites: SmCo5/Co1-xFex," *Phys. Rev. B*, vol. 58, no. 18, pp. 71–74, 1998.

[27] W. Gong, G. C. Hadjipanayis, and R. F. Krause, "Mechanically alloyed nanocomposite magnets," *J. Appl. Phys.*, vol. 75, no. 10, pp. 6649–6651, 1994.

[28] P. G. McCormick, R. Street, J. Ding, and W. F. Miao, “Mechanically alloyed nanocomposite magnets (invieted),” *J. Appl. Phys.*, vol. 83, 1998.

[29] J. Zhang, S. Zhang, H. Zhang, B. Shen, and B. Li, “Structure and magnetic properties of Sm[sub x]Co[sub 5]/α-Fe (x=0.65–1.3) prepared by mechanical milling and subsequent annealing,” *J. Appl. Phys.*, vol. 89, no. 5, p. 2857, 2001.

[30] Z. W. Liu, D. C. Zeng, R. V. Ramanujan, X. C. Zhong, and H. A. Davies, “Exchange interaction in rapidly solidified nanocrystalline RE–(Fe/Co)–B hard magnetic alloys,” *J. Appl. Phys.*, vol. 105, no. 7, p. 07A736, 2009.

[31] J. P. Liu, C. P. Luo, Y. Liu, and D. J. Sellmyer, “High energy products in rapidly annealed nanoscale Fe/Pt multilayers,” *Appl. Phys. Lett.*, vol. 72, no. 4, pp. 483–485, 1998.

[32] J. P. Liu, Y. Liu, R. Skomski, and D. J. Sellmyer, “Magnetic hardening in SmCo[sub x]–Co multilayers and nanocomposites,” *J. Appl. Phys.*, vol. 85, no. 8, p. 4812, 1999.

[33] E. E. Fullerton, J. S. Jiang, C. H. Sowers, J. E. Pearson, and S. D. Bader, “Structure and magnetic properties of exchange-spring Sm-Co/Co superlattices,” *Appl. Phys. Lett.*, vol. 72, no. 3, pp. 380–382, 1998.

[34] F. J. Cadieu, J. S. Jiang, E. E. Fullerton, M. Grimsditch, C. H. Sowers, and S. D. Bader, “Exchanges-spring behavior in epitaxial hard/soft magenetic bilayer films,” *J. Appl. Phys.*, vol. 83, no. 18, pp. 6238–6240, 1998.

[35] Y. Hou, S. Sun, C. Rong, and J. P. Liu, “SmCo[sub 5]/Fe nanocomposites synthesized from reductive annealing of oxide nanoparticles,” *Appl. Phys. Lett.*, vol. 91, no. 15, p. 153117, 2007.

[36] G. S. Chaubey, N. Poudyal, Y. Liu, C. Rong, and J. P. Liu, “Synthesis of Sm–Co and Sm–Co/Fe nanocrystals by reductive annealing of nanoparticles,” *J. Alloys Compd.*, vol. 509, no. 5, pp. 2132–2136, Feb. 2011.

[37] S. Sun, “Exchange-coupled nanocomposite magnets by nanoparticle self-assembly,” *Nature*, vol. 420, no. November, pp. 395–398, 2002.

[38] A. D. Volodchenkov, Y. Kodera, and J. E. Garay, “Synthesis of strontium ferrite/iron oxide exchange coupled nano-powders with improved energy product for rare earth free permanent magnet applications,” *J. Phys. Chem. C*, p. submitted, 2016.

[39] C.-B. Rong, V. Nandwana, N. Poudyal, J. P. Liu, T. Saito, Y. Wu, and M. J. Kramer, “Bulk FePt/Fe[sub 3]Pt nanocomposite magnets prepared by spark plasma sintering,” *J. Appl. Phys.*, vol. 101, no. 9, p. 09K515, 2007.

[40] K. H. Chen, Z. Q. Jin, J. Li, G. Kennedy, Z. L. Wang, N. N. Thadhani, H. Zeng, S.-F. Cheng, and J. P. Liu, "Bulk nanocomposite magnets produced by dynamic shock compaction," *J. Appl. Phys.*, vol. 96, no. 2, p. 1276, 2004.

[41] Y. Hou, S. Sun, C. Rong, and J. P. Liu, "SmCo[sub 5]/Fe nanocomposites synthesized from reductive annealing of oxide nanoparticles," *Appl. Phys. Lett.*, vol. 91, no. 15, p. 153117, 2007.

[42] X. Liu, S. He, J.-M. Qiu, and J.-P. Wang, "Nanocomposite exchange-spring magnet synthesized by gas phase method: From isotropic to anisotropic," *Appl. Phys. Lett.*, vol. 98, no. 22, p. 222507, 2011.

[43] D. Roy and P. S. Anil Kumar, "Exchange spring behaviour in SrFe12O19-CoFe2O4 nanocomposites," *AIP Adv.*, vol. 5, no. 7, p. 077137, Jul. 2015.

[44] V. Patel, M. El-Hilo, K. O'Grady, and R. W. Chantrell, "Nucleation fields in an exchange spring hard magnet," *J. Phys. D. Appl. Phys.*, pp. 1453–1458, 1993.

[45] E. P. Wohlfarth, "Relations between Different Modes of Acquisition of the Remanent Magnetization of Ferromagnetic Particles," *J. Appl. Phys.*, vol. 29, no. 3, p. 595, 1958.

[46] Y. Choi, J. S. Jiang, J. E. Pearson, S. D. Bader, and J. P. Liu, "Element-specific recoil loops in Sm–Co/Fe exchange-spring magnets," *J. Appl. Phys.*, vol. 103, no. 7, p. 07E132, 2008.

[47] D. Goll, M. Seeger, and H. Kronmu, "Magnetic and microstructural properties of nanocrystalline exchange coupled PrFeB permanent magnets," vol. 185, 1998.

[48] C. L. Harland, L. H. Lewis, Z. Chen, and B.-M. Ma, "Exchange coupling and recoil loop area in Nd2Fe14B nanocrystalline alloys," *J. Magn. Magn. Mater.*, vol. 271, no. 1, pp. 53–62, Apr. 2004.

[49] J. P. Liu, E. Fullerton, and D. J. Sellmyer, *Nanoscale Magnetic Materials and Applications*. Boston, MA: Springer US, 2009.

[50] C. R. Pike, A. P. Roberts, and K. L. Verosub, "Characterizing interactions in fine magnetic particle systems using first order reversal curves," *J. Appl. Phys.*, vol. 85, no. 9, p. 6660, 1999.

[51] C. R. Pike, "First-order reversal-curve diagrams and reversible magnetization," *Phys. Rev. B*, vol. 68, no. 10, p. 104424, Sep. 2003.

[52] R. J. Harrison and J. M. Feinberg, "FORCinel: An improved algorithm for calculating first-order reversal curve distributions using locally weighted regression

smoothing," *Geochemistry, Geophys. Geosystems*, vol. 9, no. 5, p. n/a–n/a, May 2008.

[53] I. D. Mayergoyz, *Mathematical Models of Hysteresis and Their Applications*, Second. Elsevier, 2003.

[54] R. C. Pullar, "Hexagonal ferrites: A review of the synthesis, properties and applications of hexaferrite ceramics," *Prog. Mater. Sci.*, vol. 57, no. 7, pp. 1191–1334, Sep. 2012.

[55] E. E. Fullerton, J. . Jiang, and S. . Bader, "Hard/soft magnetic heterostructures: model exchange-spring magnets," *J. Magn. Magn. Mater.*, vol. 200, no. 1–3, pp. 392–404, Oct. 1999.

[56] G. B. Haxel, J. B. Hedrick, G. J. Orris, S. Sound, M. Of, and O. U. R. Mineral, "Rare Earth Elements — Critical Resources for High Technology," *United States Geol. Surv. Fact Sheet*, vol. 087, p. 4, 2002.

[57] R. Nawathey-Dikshit, S. R. Shinde, S. B. Ogale, S. D. Kulkarni, S. R. Sainkar, and S. K. Date, "Synthesis of single domain strontium ferrite powder by pulsed laser ablation," *Appl. Phys. Lett.*, vol. 68, no. 24, pp. 3491–3493, 1996.

[58] S. R. Shinde, S. E. Lofland, C. S. Ganpule, S. B. Ogale, S. M. Bhagat, T. Venkatesan, and R. Ramesh, "Realization of epitaxial barium ferrite films of high crystalline quality with small resonance losses," *J. Appl. Phys.*, vol. 85, no. 10, p. 7459, 1999.

[59] C. J. S. Manuel Ocana, Maria P. Morales, "The Growth Mechanism of aFe2O3 Ellipsoidal Particles in Solution," *J. Colloid Interface Sci.*, vol. 171, pp. 85–91, 1995.

[60] B. Djuričić, S. Pickering, D. McGarry, P. Glaude, P. Tambuyser, and K. Schuster, "The properties of zirconia powders produced by homogeneous precipitation," *Ceram. Int.*, vol. 21, no. 3, pp. 195–206, Jan. 1995.

[61] H. Unuma, S. Kato, T. Ota, and M. Takahashi, "Homogeneous precipitation of alumina precursors via enzymatic decomposition of urea," *Adv. Powder Technol.*, vol. 9, no. 2, pp. 181–190, Jan. 1998.

[62] E. Matijevic, "Preparation and properties of uniform size colloids," *Chem. Mater.*, vol. 5, no. 4, pp. 412–426, 1993.

[63] P. Kulamani and J. Das, "Studies on Ferric Oxide Hydroxides," vol. 593, pp. 586–593, 1995.

[64] M. Ocaña, M. Morales, and C. Serna, “Homogeneous Precipitation of Uniform alpha-Fe2O3 Particles from Iron Salts Solutions in the Presence of Urea.,” *J. Colloid Interface Sci.*, vol. 212, no. 2, pp. 317–323, 1999.

[65] A. Volodchenkov, “Synthesis and Characterization of Metal - Oxide Composite Materials for Permanent Magnetic Applications,” Univeristy of California, Riverside, 2012.

[66] Y.-M. Chiang, D. P. Birnie, and W. D. Kingery, *Physical Ceramics*. Wiley, 1997.

[67] R. M. Cornell, R. Giovanoli, and W. Schneider, “Review of the hydrolysis of iron(III) and the crystallization of amorphous iron(III) hydroxide hydrate,” *J. Chem. Technol. Biotechnol.*, vol. 46, pp. 115–134, 1989.

[68] W. K. Jozwiak, E. Kaczmarek, T. P. Maniecki, W. Ignaczak, and W. Maniukiewicz, “Reduction behavior of iron oxides in hydrogen and carbon monoxide atmospheres,” *Appl. Catal. A Gen.*, vol. 326, no. 1, pp. 17–27, 2007.

[69] C. l. H.Lin, Y.Chen, “The mechanism of reduction of iron oxide by hydrogen,” *Thermochim. Acta*, vol. 400, pp. 61–67, 2003.

[70] L. K. Lagorce and M. G. Allen, “Magnetic and mechanical properties of micromachined strontium ferrite/polyimide composites,” *J. Microelectromechanical Syst.*, vol. 6, no. 4, pp. 307–312, 1997.

[71] Y. Choi, J. S. Jiang, J. E. Pearson, S. D. Bader, and J. P. Liu, “Origin of recoil hysteresis loops in Sm–Co/Fe exchange-spring magnets,” *Appl. Phys. Lett.*, vol. 91, no. 2, p. 022502, 2007.

[72] C. Rong, Y. Liu, and J. P. Liu, “Do thermal fluctuations influence the recoil loops of nanocomposite magnets?,” *Appl. Phys. Lett.*, vol. 93, no. 4, p. 042508, 2008.

[73] C. Rong and J. P. Liu, “Grain boundary contribution to recoil loop openness of exchange-coupled nanocrystalline magnets,” *Appl. Phys. Lett.*, vol. 94, no. 17, p. 172510, 2009.

[74] L. Kaufman, H. Nesor, and E. Street, “Coupled Phase Diagrams and Thermochemical Data for Transition Metal Binary Systems,” *Calphad Comput. Coupling Phase Diagrams Thermochem.*, vol. 2, pp. 55–80, 1978.